

Improving satellite remote sensing methodologies for analyzing landscape dynamics in arid environments with focus on Egypt

Delgado Blasco, José Manuel

DOI

[10.4233/uuid:f3e42dee-c691-4dc8-879d-6b0f828c9d8f](https://doi.org/10.4233/uuid:f3e42dee-c691-4dc8-879d-6b0f828c9d8f)

Publication date

2023

Document Version

Final published version

Citation (APA)

Delgado Blasco, J. M. (2023). *Improving satellite remote sensing methodologies for analyzing landscape dynamics in arid environments with focus on Egypt*. [Dissertation (TU Delft), Delft University of Technology, Katholieke Universiteit Leuven]. <https://doi.org/10.4233/uuid:f3e42dee-c691-4dc8-879d-6b0f828c9d8f>

Important note

To cite this publication, please use the final published version (if applicable).
Please check the document version above.

Copyright

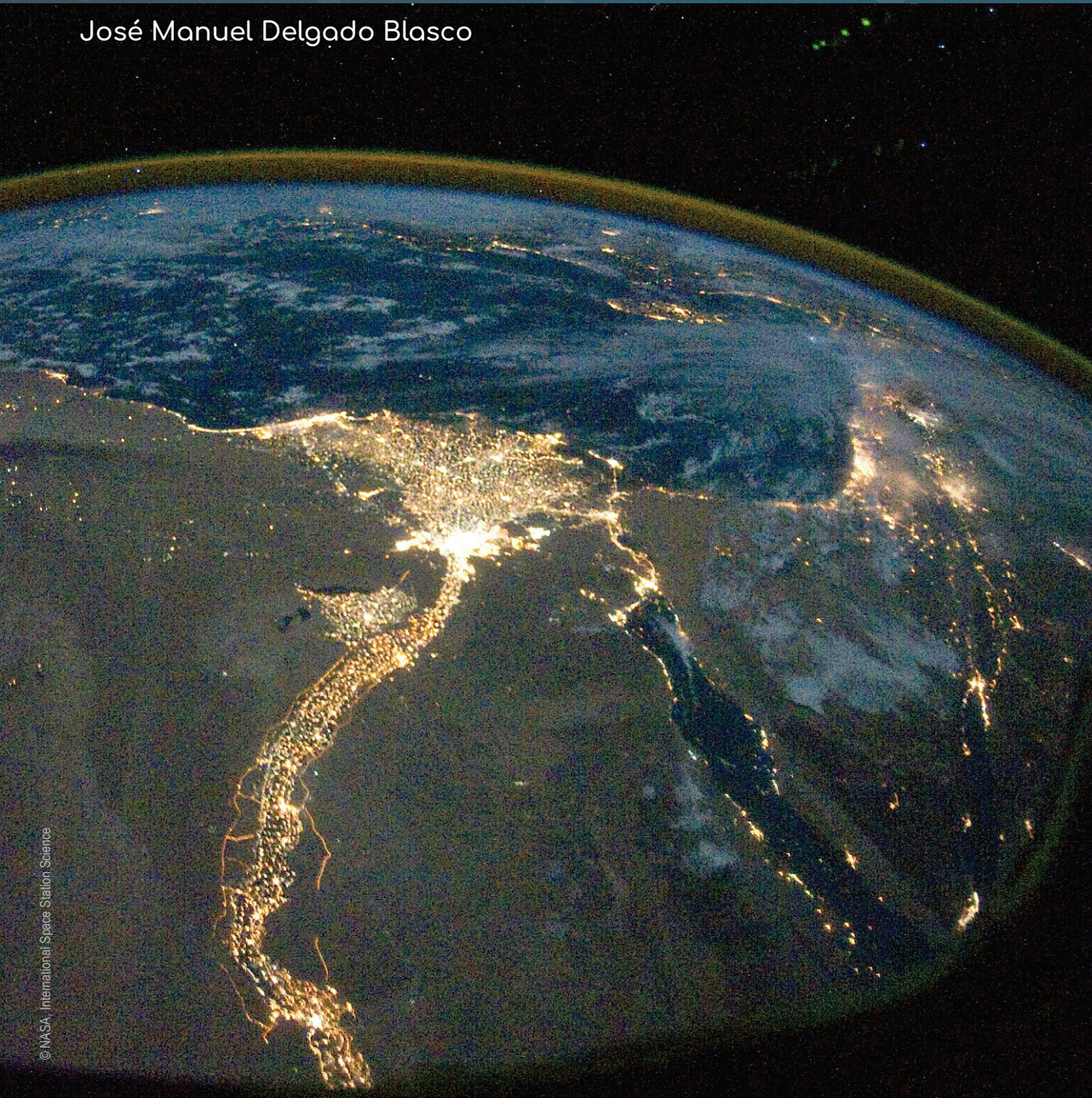
Other than for strictly personal use, it is not permitted to download, forward or distribute the text or part of it, without the consent of the author(s) and/or copyright holder(s), unless the work is under an open content license such as Creative Commons.

Takedown policy

Please contact us and provide details if you believe this document breaches copyrights.
We will remove access to the work immediately and investigate your claim.

Improving satellite remote sensing methodologies for analyzing landscape dynamics in arid environments with focus on Egypt

José Manuel Delgado Blasco



Improving satellite remote sensing methodologies for analyzing landscape dynamics in arid environments with focus on Egypt

José Manuel **Delgado Blasco**

Supervisors:

Prof. dr. ir. R.F. Hanssen

Prof. dr. G. Verstraeten

Dissertation presented in partial fulfillment of the requirements for the degree of Doctor of Science: Geography from KU Leuven and the degree of Philosophical Doctor from TU Delft.



Improving satellite remote sensing methodologies for analyzing landscape dynamics in arid environments with focus on Egypt

PROEFSCHRIFT

ter verkrijging van de graad van doctor
aan de Technische Universiteit Delft,
op gezag van de Rector Magnificus
Prof.dr.ir. T.H.J.J. van der Hagen,
voorzitter van het College voor Promoties,
in het openbaar te verdedigen op
Dinsdag 4th April 2023 om 12:30 uur

door

José Manuel DELGADO BLASCO

Master in Telecommunication Engineering,
Polytechnic University of Valencia, Spain
geboren te Valencia, Spanje.

Dit proefschrift is goedgekeurd door de promotoren:

Prof. dr. ir. R.F. Hanssen

Prof. dr. G. Verstraeten

Samenstelling promotiecommissie:

Rector Magnificus,
Prof. dr. ir. R.F. Hanssen
Prof. dr. G. Verstraeten

voorzitter
Technische Universiteit Delft, promotor
KU Leuven, promotor

Onafhankelijke leden:

Prof. dr. K.M. de Beurs,
Prof. dr. ir. S. Steele-Dunne,
Prof. dr. R. Goossens,
Prof. dr. A. van Rompaey,

Universiteit Wageningen
Technische Universiteit Delft
Universiteit Gent
KU Leuven

Delgado Blasco, José Manuel

Improving satellite remote sensing methodologies for analyzing landscape dynamics in arid environments with focus on Egypt

Delft University of Technology and KU Leuven



Keywords: Earth Observation, SAR, Radar, Urbanization, Land Use Change, Dunes dynamics, Data Fusion, Machine Learning

Printed by: Optima Grafische Communicatie

Cover design: Remedia Italia Srl

ISBN 978-94-6361-830-4

Copyright © 2023 by J.M. Delgado Blasco.

All rights reserved. No part of the material protected by this copyright notice may be reproduced or utilized in any form or by any means, electronic or mechanical, including photocopying, recording or by any information storage and retrieval system, without the prior permission of the author.

An electronic version of this dissertation is available at
<http://repository.tudelft.nl/>.

*Life is a continuous learning experience,
keep on living!*

José Manuel Delgado Blasco

Preface

The Egyptian landscape has been rapidly changing since the last decades. Most of these changes are a consequence of the Aswan High Dam construction, which stopped the Nile's yearly floods and brought electricity to Egyptian homes. Until that moment, urban settlements could only exist in elevated areas within the floodplain, as the other areas were subject to yearly floods. After completion of the Aswan High Dam, the urban settlements started to grow, most rapidly in larger cities, with Greater Cairo as an extreme case, with an exponentially increasing population since the early twentieth century.

The research reported in this thesis is focused on the analysis of the landscape dynamics of Egypt, with special attention to (i) urban expansion in urban and rural areas, and (ii) dune dynamics. The latter can become a hazard to agricultural fields and villages located in the western edge of the Nile floodplain.

During this PhD study, I experienced a revolution in the Earth Observation domain, starting from the open data policies, the Copernicus Sentinels, and a data processing paradigm shift, evolving from the traditional tools and methods to the current exploitation platforms. These enabled working with satellite data without the need of downloading them, increasing the processing possibilities.

In this multidisciplinary research, I had the chance to learn under the supervision of Ramon Hanssen and Gert Verstraeten, from two of the world leading faculties and research groups in their relative disciplines, i.e., (In)SAR theory and applications, geography and geomorphology of Egypt, dune formation, dune dynamics and Egyptian archaeology.

I explored the synergy of fusing Synthetic Aperture Radar (SAR) data with multi-spectral optical data, and the design of Artificial Neural Networks (ANN) to develop machine learning methods that improve state-of-the-art methods, especially for Land Use Land Cover (LULC). In collaboration with Dr. Fabio Cian I explored the usage of large time series statistics and Big data platforms to improve LULC classification models. Together with Dr. Marco Chini, I developed the first fully automatic method to compute dune dynamics using SAR data.

In collaboration with Prof. Dr. Antonio M. Ruiz-Armenteros I analysed the structural stability of Aswan High Dam using interferometry with the available SAR sensors.

I hope that this thesis will prove useful for new generations of scientists, and sparkle the same excitement as I experienced writing it.

*José Manuel Delgado Blasco
Delft, April 2023*

Contents

Preface	VII
Summary	XI
Samenvatting	XIII
Resumen	XV
Nomenclature	XVII
1 Introduction	1
1.1 Motivation	1
1.2 Background and Problem statement	2
1.3 Research objectives	4
1.4 Thesis roadmap	5
2 Greater Cairo urban growth analysis (1998 – 2015)	7
2.1 Introduction	7
2.1.1 Previous works on land cover classification over Greater Cairo: limitations	8
2.2 Study area and remote sensing datasets.	12
2.3 Methodology	13
2.3.1 Data preparation.	13
2.3.2 Land use classification.	15
2.3.3 Validation approach	18
2.3.4 Temporal evolution analysis	18
2.4 Results	19
2.4.1 Land use classification.	19
2.4.2 Temporal evaluation of the classified land use/cover maps	22
2.4.3 Built-up sprawl in Hadayek Al Ahram (Pyramids Gardens)	24
2.5 Discussion	27
2.6 Conclusion	29
3 Land cover dynamics in the Nile Valley and Middle Egypt	31
3.1 Introduction	31
3.2 The Study Area	33
3.3 Materials and Methods	35
3.3.1 Step 1: Data Preparation and Indicators Extraction	36
3.3.2 Step 2: Land Cover Mapping	38
3.3.3 Step 3: Multi-Temporal Evolution Analysis	40

3.4	Result	42
3.5	Discussion	48
3.5.1	Quality of the Data Fusion Approach Compared to Single Platform Approaches	48
3.5.2	Urban and Agricultural Land Dynamics	49
3.6	Conclusions.	52
4	Automatic dune dynamics analysis using multi-temporal SAR data	55
4.1	Introduction	55
4.2	Study area.	58
4.3	Materials and Methods	59
4.3.1	Materials.	59
4.3.2	Methodology.	59
4.4	Results	65
4.4.1	West Sahara - Mauritania	65
4.4.2	South-Rayan Dune Field in Egypt	69
4.5	Discussion	73
4.5.1	Overall comments from the proper exploitation of the proposed approach.	75
4.5.2	Implications in other domains	76
4.6	Conclusions.	76
5	Conclusions and Recommendations	77
5.1	Conclusions.	77
5.2	Contributions.	79
5.3	Recommendations	80
	Bibliography	83
	Acknowledgements	97
	About the author	99
	List of related publications	101
	Other publications	103

Summary

Monitoring rapidly changing landscapes, especially those which cannot be easily accessed due to climate conditions, access or insecurity has been always a very challenging task. It is particularly timely to be able to accurately monitor such changing landscapes given the current socio-economical changes and population growth of many developing countries, as land is a limited resource and it is crucial that it is used in a planned and sustainable manner. Egypt is the perfect example of a country where the population increase linked to urban growth goes at the expense of agricultural land. Landscape dynamics in Egypt are changing very rapidly. In particular the continuous growth of urban areas, sand storms regularly covering roads and buildings, and dunes approaching villages and crop fields in the western edge of the Nile floodplain call for a continuous monitoring strategy. Satellite remote sensing is optimally suited to provide the required spatio-temporal coverage. Yet, currently used satellite remote sensing technologies have shortcomings that need to be addressed. Optical remote sensing techniques fail to detect the construction of buildings when the same materials (mud blocks) are used as their natural surroundings.

Dunes need also to be regularly monitored, specially the ones that are considered hazards as they migrate towards inhabited areas or crop fields, but this has been traditionally done or at very small scale and using time consuming and expensive procedures. In this research, we investigated the combination of optical and microwave (SAR) satellite data to overcome the aforementioned limitations and we propose the usage of SAR data to analyse dune migration phenomena.

In this study we develop appropriate methods and provide accurate maps to facilitate landscape dynamics analysis for Egypt, focusing on urban sprawl and dune dynamics. We improved the detection of urban areas and developed an automatic method for the monitoring the dynamics of individual dunes. Our method for urban change detection overcomes the limitations of previous urban maps derived from optical sensors and improved state-of-the-art global urban layers. Additionally, our method for individual dune dynamics improves the traditional field survey methods, overcoming limitations of the optical sensor methods and is, to our knowledge, the first automatic method using SAR backscatter to monitor individual dune dynamics at dune-field scale.

We employed satellite data fusion methods, artificial neural networks, and big data analysis to develop land cover classification methods applicable not only in Egypt but also in similar environments. Additionally, the developed method for dune dynamics analysis with SAR is also exportable to other dune-fields and dune types, enabling a more frequent individual dune dynamics monitoring at dune-field scale, which was not possible until now.

The proposed methods for land use classification can be applied to other locations with similar conditions, and countries rapidly changing landscapes with arid environment. These methods can help in urban planning activities or in monitoring systems, as

they can detect areas where built-up activities are in early stages, or areas with undefined anthropogenic disturbances.

The proposed method for dune mapping and dune migration analysis could be employed for i) permanent monitoring of dune fields, ii) planning building activities inside a sandy desert, iii) protecting and planning any possible relocation activities of already-built infrastructure on Earth or any other planet with sandy desert and dune formations, among others.

Samenvatting

Het monitoren van snel veranderend landgebruik is een uitdagende taak, in het bijzonder op locaties die moeilijk toegankelijk zijn, bijvoorbeeld door klimaat- of veiligheidsomstandigheden. Met name voor ontwikkelingslanden, vaak gekenmerkt door grote bevolkingsgroei en snelle sociaal-economische veranderingen, is het tijdig volgen van veranderend landgebruik van groot belang. Bruikbaar land is daar schaars, en moet bovendien planmatig en duurzaam worden gebruikt. Egypte is een voorbeeld van een land waar bevolkingstoename leidt tot stedelijke groei ten koste van landbouwgrond. De dynamiek van het landgebruik in Egypte is groot. Hierdoor is een permanente en systematische monitoringsstrategie vereist, zowel met het oog op de voortdurende groei van stedelijke gebieden, maar ook met betrekking tot de effecten van zandstormen die regelmatig wegen blokkeren en gebouwen bedekken, en de systematische beweging van zandduinen die dorpen en akkers aan de westelijke rand van de uiterwaard van de Nijl bedreigen.

Satelliet remote sensing is optimaal geschikt om de vereiste spatio-temporele dekking te verschaffen. Echter, de momenteel gebruikte technologieën vertonen significante tekortkomingen. Zo slaagt optische remote sensing er bijvoorbeeld niet goed in om de constructie van gebouwen te detecteren indien hiervoor dezelfde materialen (kleiblokken) worden gebruikt als hun natuurlijke omgeving. Ook de positie en migratie van zandduinen dient regelmatig te worden gecontroleerd, vooral duinen die als gevaarlijk kunnen worden beschouwd omdat zij zich richting bewoonde gebieden of akkers bewegen. Traditioneel wordt dit alleen lokaal gedaan, gebruikmakend van tijdrovende en dure procedures. In dit onderzoek combineren we optische en microgolf (SAR) satellietgegevens om bovengenoemde beperkingen te overwinnen en analyseren we duinmigratieverschijnselen met SAR-gegevens. De focus ligt hierbij op het ontwikkelen en testen van methoden en het leveren van nauwkeurige kaarten om de analyse van landgebruiksdynamiek van Egypte te vergemakkelijken, met de nadruk op stadsuitbreiding en duindynamiek. De detectie van stedelijke gebieden is hierdoor sterk verbeterd en de dynamiek van individuele duinen wordt automatisch gemonitord. De nieuwe methode voor de detectie van stedelijke veranderingen verbetert eerdere stedelijke kaarten, gebaseerd op uitsluitend van optische sensoren, en dientengevolge de state-of-the-art globale stedelijke kaartlagen. De methode voor het monitoren van de dynamiek van individuele duinen is effectiever dan de traditionele veldkarteringsmethoden, overtreft de optische sensormethoden, en is de eerste automatische methode die gebruik maakt van SAR-backscatter om de dynamiek van individuele duinen op veldschaal te monitoren.

Satelliet data fusie methoden, kunstmatige neurale netwerken, en big data analyses zijn gebruikt om land-cover classificatie methoden te ontwikkelen die niet alleen in Egypte toepasbaar zijn, maar ook in vergelijkbare omgevingen. Zij kunnen helpen bij stadsplanningsactiviteiten of in monitoringsystemen, omdat zij gebieden kunnen detecteren waar de bebouwingsactiviteiten zich in een vroeg stadium bevinden, of

gebieden met ongedefinieerde antropogene verstoringen. Ook de methode voor duindynamiekanalyse met SAR is exporteerbaar naar andere duingebieden en duintypes, waardoor een frequentere individuele duindynamiekmonitoring op duinveldschaal mogelijk wordt. Deze zou kunnen worden gebruikt voor permanente monitoring van duingebieden, planning van bouwactiviteiten in een zandwoestijn, de bescherming en planning van eventuele verplaatsingsactiviteiten van reeds gebouwde infrastructuur, of de analyse van zandwoestijn- en duinformaties op andere planeten.

Resumen

El seguimiento de los paisajes que cambian rápidamente, especialmente aquellos a los que no se puede acceder fácilmente debido a las condiciones climáticas, el acceso o la inseguridad, ha sido siempre una tarea muy difícil. Es especialmente oportuno poder supervisar con precisión esos paisajes cambiantes, dados los actuales cambios socioeconómicos y el crecimiento demográfico de muchos países en desarrollo, ya que la tierra es un recurso limitado y es crucial que se utilice de forma adecuada, planificada y sostenible.

Egipto es el ejemplo perfecto de un país en el que el aumento de la población ligado al crecimiento urbano va en detrimento del suelo agrícola. La dinámica del paisaje en Egipto está cambiando muy rápidamente. En particular, el crecimiento continuo de las zonas urbanas, con tormentas de arena que cubren regularmente las carreteras y los edificios, y las dunas que se acercan a los pueblos y a los campos de cultivo en el borde occidental de la llanura de inundación del Nilo exigen una estrategia de seguimiento continuo. La teledetección por satélite es idónea para proporcionar la cobertura espacio-temporal necesaria. Sin embargo, las tecnologías de teledetección por satélite que se utilizan en la actualidad presentan deficiencias que es preciso subsanar. Las técnicas de teledetección óptica no detectan la construcción de edificios cuando se utilizan los mismos materiales (bloques de barro) que su entorno natural.

También es necesario vigilar periódicamente las dunas, especialmente las que se consideran peligrosas porque migran hacia zonas habitadas o campos de cultivo. Esto se ha hecho tradicionalmente, pero a muy pequeña escala y utilizando procedimientos costosos y que requieren mucho tiempo.

En esta tesis, investigamos la combinación de datos satelitales ópticos y de microondas (SAR) para superar las limitaciones mencionadas y proponemos el uso de datos SAR para analizar los fenómenos de migración de dunas. En este estudio desarrollamos métodos adecuados y proporcionamos mapas precisos para facilitar el análisis de la dinámica del paisaje en Egipto, centrándonos en la expansión urbana y la dinámica de las dunas. Mejoramos la detección de las zonas urbanas y desarrollamos un método automático para el seguimiento de la dinámica de las dunas individuales. Nuestro método para la detección de cambios urbanos supera las limitaciones de los mapas urbanos anteriores derivados de sensores ópticos y mejora las capas urbanas globales de última generación. Además, nuestro método para la dinámica de dunas individuales mejora los métodos tradicionales de estudio de campo, superando las limitaciones de los métodos de sensores ópticos y es, hasta donde sabemos, el primer método automático que utiliza la retrodispersión SAR para monitorizar la dinámica de dunas individuales a escala de campo de dunas.

Empleamos métodos de fusión de datos satelitales, redes neuronales artificiales y análisis de big data para desarrollar métodos de clasificación de la cobertura del suelo aplicables no sólo en Egipto sino también en entornos similares. Además, el método

desarrollado para el análisis de la dinámica de las dunas con SAR también es exportable a otros campos de dunas y tipos de dunas, lo que permite un seguimiento más frecuente de la dinámica de las dunas individuales a escala de campo de dunas, lo que no era posible hasta ahora.

Los métodos propuestos para la clasificación del uso del suelo pueden aplicarse a otros lugares con condiciones similares, y a países con paisajes rápidamente cambiantes con un entorno árido. Estos métodos pueden ayudar a las actividades de planificación urbana o a los sistemas de monitorización, ya que permiten detectar las zonas en las que las actividades de construcción están en sus primeras etapas, o las zonas con perturbaciones antropogénicas no definidas.

El método propuesto para el mapeo de dunas y el análisis de la migración de las dunas podría emplearse para i) el monitoreo permanente de los campos de dunas, ii) la planificación de las actividades de construcción dentro de un desierto arenoso, iii) la protección y la planificación de cualquier posible actividad de reubicación de la infraestructura ya construida en la Tierra o cualquier otro planeta con desierto arenoso y formaciones de dunas, entre otros.

Nomenclature

List of acronyms

ANN	Artificial Neural Network
ASAR	Advanced Synthetic Aperture RADAR
CAMPAS	Central Agency for Public Mobilization and Statistics
CCI	Climate Change Initiative
CGIAR	Consultative Group for International Agricultural Research
COSI-Corr	Co-Registration of Optically Sensed Images and Correlation
CSI	Consortium for Spatial Information
dB	decibel
DEM	Digital Elevation Model
DEOS	Delft Institute for Earth-oriented Space Research / Department of Earth Observation and Space Systems
DGPS	Differential GPS
DL	Deep Learning
DLR	German Space Center
DORIS	Delft object-oriented radar interferometric software
ENVISAT	Environmental Satellite
ERS	European Remote Sensing Satellite
ESA	European Space Agency
ETM	Enhanced Thematic Mapper
GCPs	Ground Control Points
GHSL	Global Human Settlement Layer
GPR	Ground Penetrating RADAR
GPS	Global Positioning System
GRD	Ground Range Detected
GUF	Global Urban Footprint
IMS	Image Mode Single Look Complex
IW	Interferometric Wide Swath
JERS	Japanese Earth Resources Satellite
JRC	Joint Research Center
Landsat	Land Remote-Sensing Satellite
LIST	Luxembourg Institute of Science and Technology
LULC	Land Use Land Cover
MLP	Multi Layer Perceptron
NDVI	Normalised Difference Vegetation Index
NDBI	Normalised Difference Built-up Index
NDWI	Normalised Difference Water Index
NDSWIR12	Normalised Difference Short-Wave Bands 1 & 2 Index

NEST	Next ESA SAR Toolbox
NIR	Near InfraRed
OLITIRS	Operational Land Imager and Thermal Infrared
RADAR	Range and Detection
RF	Random Forest
RGB	Red Green Blue
RTK	Real Time Kinematics
SAR	Synthetic Aperture RADAR
SLC-off	Scan Line Corrector failure
SNAP	SentiNel Application Platform
SRDF	South-Rayane Dune Field
SRTM	Shuttle RADAR Topography Mission
SVM	Support Vector Machine
SWIR	Short-wave Infrared
TM	Thematic Mapper
TOPSAR	Terrain Observation with Progressive Scans SAR
UAD	Undefined Anthropogenic Disturbances
UNESCO	United Nations Educational, Scientific and Cultural Organization
USGS	United States Geological Survey
UTM	Universal Transverse Mercator
WGS84	World Geodetic System 1984
WHCS	World Heritage Cultural Site
WHS	World Heritage Site
WSM	Western Sahara - Mauritania

List of symbols

cm	Centimeter
km	Kilometer
km ²	square Kilometer
m	Meter
mm	Millimeter
yr	Year
(.)*	Complex conjugate operator
A	Complex Phasor
D_a	Coefficient of dispersion
μ	mean of amplitude
γ	Interferometric coherence
σ	SAR Calibrated backscatter

1

Introduction

1.1. Motivation

The world's landscape is transforming rapidly and monitoring these changing landscapes is a very challenging task. Due to the current socio-economical changes and population growth of many developing countries, there is a huge anthropogenic pressure on land cover (Brink et al., 2014; Dong et al., 2019), including on the one hand urban expansion and on the other hand agricultural development. Hence, it is particularly timely to accurately monitor such changing landscapes, as land is a limited resource and it is crucial that it is used in a sustainable manner.

The research here presented is framed within the STEREO-II project called "Anthropogenic and physical landscape dynamics in large fluvial systems" (APLADYN) (BELSPO, 2019), from the Belgian Science Policy Office (BELSPO). In particular, this research contributed to the APLADYN project with the development of monitoring tools and the provision of accurate measurements of the anthropogenic and physical landscape dynamics of large fluvial systems. We had focused our study on Egypt, as it is the perfect example of a country where the population increase linked to urban growth goes at the expense of agricultural land, and its landscape had suffered a huge transformation in the last decades, especially in urban growth, since the completion of the Aswan High Dam.

The controlled and uncontrolled changes that Egypt suffered are also linked to its socio-economical and geo-political factors, which also play an important role in its urban transformation, and had a direct effect on the reduction of available fertile and arable land within the Nile floodplain. This reduction pushed the conversion of some desert areas into new arable land, and after several years, this land becomes abandoned or decommissioned and turned back to desert.

Analyzing landscape dynamics in arid environments using field surveys and medium resolution optical data has been and is still widely used, but the methods employed in such analysis present several limitations. We want to improve these methods by introducing the usage of SAR data in specific domains such as urban expansion analysis and dune dynamics.

1.2. Background and Problem statement

Since the origin of remote sensing, applications had been developed using the first available source of data, i.e. aero-photography Karan (1960); Bowden and Brooner (1970); Vinogradov (1977); Kozlov (1979) which later included also optical or multi-spectral satellite imagery acquired by IRS-1 and Landsat satellites Miller (1978); Punkari (1982); Mainguet (1984); Payette and Filion (1985). Since then and until recent years, and despite the appearance of the first Synthetic Aperture Radar (SAR) satellites in 1991, land mapping applications such as land cover classification have been dominated by the usage of optical imagery despite its known limitations (according to Google Scholar only 10% of the publications used SAR data for land cover classification purposes from 1991 to 1999). These limitations include dependency on sun illumination, cloud cover or difficulties to differentiate objects composed of similar materials. On contrary, SAR imagery is weather independent and can acquire images independently of day/night and weather conditions. However, only a minority started to use SAR data since its origin. Some of the reasons could be due to their data access policies, their complexity to process the data (specific methods, software and knowledge where needed) or their immediate differences to interpret with the optical satellite data, which is more similar to what the human eye is used to see.

When working in arid environments, (e.g Egypt), optical data faces additional difficulties in mapping the urban growth of cities, where periodic sand storms covering roads and building roofs add more difficulty to the land cover mapping tasks of such environments, preventing, for example, an accurate detection of urban features.

After listing above some of the different limitations of the most used techniques, and exactly in these scenarios, it is when SAR data needs to be investigated and when possible, also integrated in approaches that could improve the traditional land cover methods.

While SAR data had already demonstrated a huge potential for sand dune mapping and/or dune characterization (Blumberg, 1998), practical studies still use traditional survey tools (Barnes, 2001; Al-Harthi, 2002; Käyhkö, 2007; Santalla et al., 2009; Kostaschuk and Best, 2005; Baptista, P; Bastos, L; Bernardes, C; Cunha, T; Dias, 2008; Nuyts et al., 2020) or satellite optical data (Mohamed and Verstraeten, 2012; Hermas et al., 2004; Nuyts et al., 2020). Traditional survey tools are time-consuming and provide data over very limited and selected areas while optical or SAR data could potentially provide observations more frequently and in a larger-scale. However, no automatic method was found at the moment of initiating this research.

Countries that could benefit the most from the exploitation and inclusion of SAR data in their daily monitoring activities could be the ones located in arid regions and suffering an acceleration rate of demographic increase and urban pressure. A clear example is Egypt, where Greater Cairo had not stopped growing and where all the above limitations are found in papers studying Cairo and Egypt.

This dissertation aims to improve methodologies, by introducing the usage of SAR data, to overcome limitations of the traditional methods which employed multi-spectral or field survey methods, with special interest on urban, rural, and desert areas of Egypt.

We present an overview of the state-of-the-art methods found in literature, which have evolved since the beginning of this PhD research until its end for each of the main

techniques employed.

Landscape dynamics can be analyzed using multi-temporal land cover maps. In this regard, land cover classification has traditionally been derived from optical data. However, this has shown already its limitations, which are still visible in the Sentinel-2 prototype Land Cover map 20m of Africa released on 2017 (European Space Agency, 2017), but also in previous works of land cover classification with problems distinguishing between different objects composed of the same material can be difficult. Stewart et al. (2004) reported difficulties in spectrally distinguishing urban and desert features from optical sensors in the desert areas of Greater Cairo, due to the heavy layer of sand/dust that coats buildings and the fact that in this area construction materials are sourced from the nearby desert land.

More recently, the urban sprawl of Greater Cairo has been also analyzed using TerraSAR-X data and Landsat data (Taubenböck et al., 2008) from 1972 to 2008, using a statistical feature based approach, extending his initial research with urban data derived from TerraSAR-X data for 2010 (Taubenböck et al., 2012). However, his results classified cemeteries as urban, and these should not be taken into consideration for accounting for the urban population density.

Finally, more recent efforts are dedicated to get global urban and global land cover layers such as the Global Urban Footprint (Esch et al., 2017, 2011) processed by the German Aerospace Center, the Global Human Settlements layers from the Joint Research Center (Florczyk et al., 2018) or the ESA-CCI Land cover maps (European Space Agency, 2017). However, each of them come with its advantages and limitations when using them at regional or small scale, and they are designed with different methods and satellite data.

Since the last decades, the usage of artificial intelligence methods has been exploited for land cover classification, starting with machine learning techniques such as Multi-layer Perceptron (MLP), Support Vector Machines (SVM), Random Forest (RF), etc. and more recently also Deep Learning (DL) techniques are being used, despite needing much higher computing resources and training data than traditional supervised classification methods.

Regarding natural landscape dynamics, the research will focus on dunes dynamics, as it has been traditionally studied and measured using field surveys, with measuring tape roads (Barnes, 2001; Al-Harthi, 2002), optical and electronic levelling (Käyhkö, 2007), DGPS (Santalla et al., 2009; Kostaschuk and Best, 2005; Baptista, P; Bastos, L; Bernardes, C; Cunha, T; Dias, 2008), RTK-GPS (Pardo-Pascual et al., 2005; Mitasova et al., 2005), total station (Arteaga et al., 2008), terrestrial laser scanning (Łabuz, 2016) and ground penetrating radar (Santalla et al., 2009; Buynevich et al., 2011). However, field campaigns are costly and limited (spatial and temporal coverage).

In the last decades, satellite imagery was adopted on such studies, but mainly optical data with semi or automatic techniques such as multitemporal RGB (Mohamed and Verstraeten, 2012) or COSI-Corr (Hermas et al., 2004) respectively. However, medium resolution optical data has difficulties in properly differentiating the full sand dunes' shapes from their sandy surroundings and has its dependency on sun illumination, cloud coverage, and weather conditions. SAR data overcome these limitations and it has been used only in the last few years, but mainly in interplanetary dune exploration,

such as in Mars (Luke and King, 2019) or in equatorial regions of Titan (Radebaugh et al., 2010; Paillou et al., 2014; Le Gall et al., 2012; Lopes et al., 2010; Radebaugh et al., 2008; Paillou et al., 2016). Some works on dunes using SAR data had been found to derive dunes characteristics (Qong, 1996; Blumberg, 2006, 1998), detect dunes' area using correlation (Gouinaud et al., 2013) or interferometric coherence (Havivi et al., 2018; Song et al., 2020). However, no automatic method has been found using SAR data.

1.3. Research objectives

This thesis is aimed to develop methodologies to analyze the multi-temporal evolution of specific landscape features across a range of environments following anthropogenic activities with a focus on Egypt.

This research will focus on three different but interconnected phenomena, from which two of them are related to the global changes which are also encountered in Egypt:

1. Urban transformation of Greater Cairo and selected rural areas which had been increasing dramatically in the last decades following exponential population growth.
2. Natural dynamics caused by dune migration, with special attention to the South-Rayan dune field which interacts with crop fields in the west flank of the Nile floodplain
3. Agricultural explosion in desert areas, especially after the Spring Arab revolution as it can be seen in next sections and chapters.

These phenomena are interconnected, and not only because they occur in the Nile floodplain or in the near surroundings. As stated above, Egypt is characterized by specific geomorphology leaving little space to live and perform agricultural activities (i.e. restricted to the Nile valley from ancient times onwards), whilst it has been confronted with a significant population increase. Urbanization processes have become critical over the last few decades. However, this process of urbanization resulted in a loss of fertile agricultural land and hence, new urban developments as well as agricultural extensions have been initiated in the desert regions.

This research aims also to offer a set of tools for an effective landscape dynamics management policy. This set of tools is especially crucial for Egypt where controversial subjects regarding urban governance and the protection of cultural heritage need to be carefully considered with accurate and updated information.

These objectives are formulated as the following research questions:

- **Can the current methods of urban classification in arid environments be improved by introducing satellite SAR data and machine learning techniques? Are we able to provide accurate urban expansion maps over urban and rural areas in Egypt?**

Current classification maps are mainly produced using satellite optical data, as historically, the research community is more used to this type of data. It was

found in the literature that the usage of such data has some intrinsic limitations when working in arid/semiarid regions, which we want to overcome by introducing Synthetic Aperture Radar data. Until one decade ago, the land use/land cover classification maps were created using the most common supervised and unsupervised classification methods such as Maximum likelihood and K-means. Artificial Neural Networks just started to be employed for this purpose and, it was blooming the usage of SAR data, as it has the very big advantage of being an active sensor able to provide data independently of the weather conditions.

In this research, it will be explored the usage of SAR data to produce Land Use Land Cover (LULC) classification maps alone and in combination with other sensors so that the best LULC maps could be generated for the defined AOIs. The usage of ANN will be also investigated for such LULC production.

- **Can satellite SAR data help to improve the current methods of dune migration analysis? Can be these analysis done automatically? Can this be done at dune field scale?**

Current dune migration analysis are still done via GPS campaigns where the set of studied dunes are very limited, mainly due to the cost and efforts required to carry out field surveys in such extreme and dangerous environments where dunes are located, normally within the desert. Other methods rely on processing workflows that need manual delineation/correction of dune shapes, such as (?), showing the need of having a robust, reliable and automatic method to measure dune dynamics.

The potential usage of SAR data for carrying out such kind of analysis will be evaluated, and we will investigate the possible developments of a fully automatic method which could be not dependent on the area of interest analyzed.

1.4. Thesis roadmap

The current chapter states the motivation and the goals of this study.

Chapter 2 is dedicated to the analysis of the urban expansion and crop fields evolution on Egypt's capital, Cairo and its surroundings, which analysis is carried out using a multi-temporal satellite data fusion approach using SAR and optical data, using machine learning approach using limited data available due to the limits of data access and processing of that period. Finally, the resulting produced maps are compared with current state-of-the-art urban layers produced by institutions such as European Space Agency (ESA), German Aerospace Center (DLR), and Joint Research Center (JRC).

Chapter 3 presents the landscape dynamics of Egypt's rural area of the Middle Egypt province, and it uses new big data technologies offered by Google, the so-called Google Earth Engine for the pre-processing of the satellite data in order to produce annual temporal statistics both on optical data and free available SAR data. Here, we selected Support Vector Machine as the land cover classifier that will finally produce the desired LULC maps over the region. In this chapter, we had also compared our results with the urban layers provided by ESA, DLR and JRC, with outstanding outcomes.

Chapter 4 presents and describes the automatic method developed for monitoring

1

dune dynamics of isolated barchan dunes. This method has been produced in collaboration with Dr. Marco Chini from the Luxembourg Institute of Science and Technology (LIST).

Finally, Chapter 5 summarises the most important findings and conclusions of this research, and provides some suggestions for future work.

2

Greater Cairo urban growth analysis (1998 – 2015)

Due to the rapid land cover changes that occurred in Greater Cairo in the last decades, traditional land cover methods showed limitations in detecting new urban areas in the desert. In this chapter, these limitations were overcome by applying a data fusion approach. In addition, we had defined a new land use class that enables the early identification of future built-up areas. This new methodology could be used for detecting illegal housing and it is exportable to other areas with similar conditions.

2.1. Introduction

The world is becoming progressively urbanized. Especially in developing countries, this trend has been accelerating over the last two decades. Over the next 30 years, the world's population growth is expected to be concentrated in urban areas within the developing world (Vermeiren et al., 2012). The challenges for achieving sustainable urban development will be particularly significant in Africa (Cohen, 2006). This is certainly true for Cairo, the most populous urban agglomeration in Africa in 2010 (The Guardian, 2010) and the second most populated in 2015 after Lagos (Karuga, 2019). The urban sprawl of Cairo during the last decades resulted in the replacement of the fertile floodplain of the River Nile by urban structures. From the time of the 1996 population census onwards, the Egyptian government has tried to avoid new constructions in the Nile floodplain by encouraging people to live outside the so-called 'green land' and settle in the arid areas of the eastern and western desert plateau (Sutton and Fahmi,

This chapter has been published in *Journal of Cultural Heritage* with the title *Detecting modern desert to urban transitions from space in the surroundings of the Giza World Heritage site and Greater Cairo*, (Delgado Blasco, Verstraeten and Hanssen, 2016). To fit the publication into this study minor changes have been made. Data and maps on urban expansion have been updated with new information from 2015 as published in the *Proceedings of ESA Living Planet Symposium 2016* with title *Exploring the Data Fusion of European SAR and Landsat Satellites for Monitoring the Urban Changes in Greater Cairo (Egypt) from 2010 to 2015* (Delgado Blasco, Verstraeten, Hanssen and Ruiz-Armenteros, 2016)

2001). Despite the restrictions introduced in 1996 inner-city slums grew, and informal settlements bloomed on the urban fringe (Harris and Wahba, 2002). What is particularly troublesome is the increasing urban pressure on the Giza pyramids plateau, designated as UNESCO World Heritage Site (WHS) and protected by the 1972 World Heritage Convention (UNESCO, 2008). Debate between scholars, practitioners, and activists over development activities within and around this unique site is leading to growing conflict between conserving the archaeological site on the entire plateau and developing the surrounding areas (Shetawy and El Khateeb, 2009).

In 1996, Cairo's population was approximately 6.78 million citizens, while in 2006 it reached 7.78 million inhabitants, reported in 2012 an approximate population of 8.76 (Source: <http://statoids.com/ueg.html>), and latest CAMPAS publish population information reports more than 9 million people (Fig. 2.1). Considering that Cairo is only one of the three main districts forming the so-called Greater Cairo (Kayouba, Cairo, and Giza districts). Then, the total population of Greater Cairo is about 22 million people in 2015 according to Statoids and CAMPAS (Law, 2016).

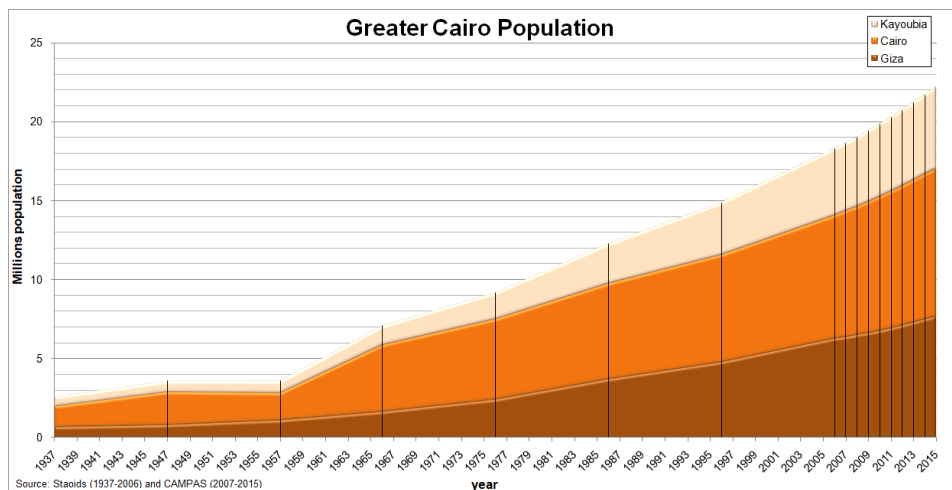


Figure 2.1: Greater Cairo population figures by governorate from 1937 to 2015 (Source: Statoids and CAMPAS).

Detailed mapping and monitoring of the evolution of Cairo's urban structure and morphology is therefore needed for an effective management policy and a comprehensive view on urban governance and the protection of cultural heritage.

2.1.1. Previous works on land cover classification over Greater Cairo: limitations

Several studies have discussed remote sensing techniques to monitor and analyze dynamic expansion and urbanization in Greater Cairo. Most of them have made use of optical sensors (de Noronha Vaz et al., 2011b; Hassan, 2011). However, using just optical data, distinguishing between different objects composed of the same material can be difficult. Stewart et al. (2004) reported difficulties in spectrally distinguishing urban

and desert features from optical sensors in the desert areas of Greater Cairo, due to the heavy layer of sand/dust that coats buildings and the fact that in this area construction materials are sourced from the nearby desert land.

Because of this limitation found in the literature, we had explored the Landsat 5 TM and 7 ETM+ data to derive land use maps for different periods using artificial neural networks with multi-layer perceptron. Parallely, we had explored the land cover classification using ERS SAR and Envisat ASAR IMS data to derive as well land cover maps for the same time period done with Landsat data, in order to compare them and see their differences.

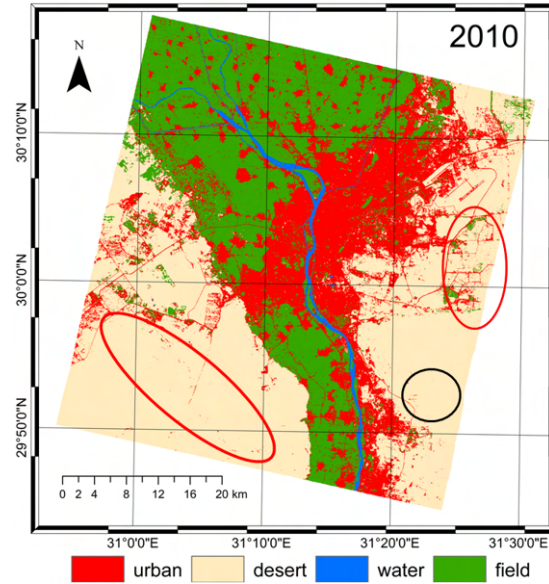


Figure 2.2: 2010 Optical land cover classification derived from Landsat 7 ETM+ imagery acquired on 2010 and detailed on Table 2.2. Ellipses indicate areas with main differences between this classification map (containing desert and urban classes) and the ones on Fig. 2.3 (containing field and urban classes).

In Fig. 2.2 is illustrated the land cover classification obtained using Landsat data and in Fig. 2.3 the one obtained for Envisat ASAR data, both using 2010 data. In color circles highlight the main differences between both classification maps. SAR data derived maps provided vegetation areas inside the desert which optical does not, and optical data derived maps provide less urban data inside such ellipses. In addition inside black circle SAR maps provide higher urban, and that could be due to higher topography in the scene. As it was discussed in Delgado Blasco et al. (2013), analysis using only Synthetic Aperture RADAR data and their derived coherence products might also produce misclassification of areas with high temporal variability.

In Tab. 2.1 are indicated the km^2 occupied by the different classes on the computed Land Cover maps for the different analyzed time periods. Both approaches seem to have different values for all classes, and we consider that the main differences could be caused by the temporal variability of the input data employed for the SAR classifications.

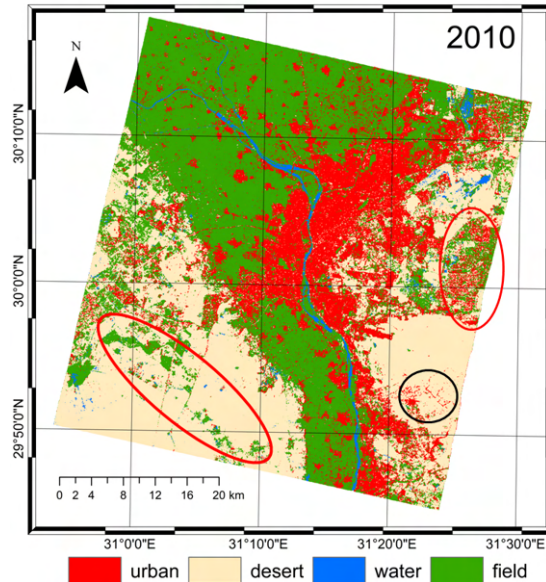


Figure 2.3: 2010 SAR land cover classification map derived from Envisat ASAR imagery acquired in 2010 and detailed on Table 2.2. Ellipses indicate areas with main differences between this classification map (containing vegetation and urban classes) and the ones on Fig. 2.2 (containing desert and urban classes).

Table 2.1: Comparative of area (km²) occupied by classes for the different dates and classification maps. Differences between SAR and Optical increase with time. Main differences in desert class are distributed in water and field classes.

Class	1998		2004		2010		2015	
	SAR	Optical	SAR	Optical	SAR	Optical	SAR	Optical
Urban	497.56	485.26	519.35	573.13	591.59	612.67	611.75	957.19
Desert	840.37	1270.57	917.32	1149.29	908.98	1161.08	746.63	1018.60
Water	48.79	31.98	40.96	37.02	41.11	34.38	177.35	37.06
Fields	1114.96	713.90	1029.37	747.56	965.32	698.87	1048.80	571.65

These indicators contain information of changes, at this is the reason why many areas detected as desert in optical derived maps, in SAR derived maps are consider either vegetation or water.

In addition, visualizing the Normalized Vegetation Index (NDVI) derived from the Landsat image selected for 2010 as shown in Fig 2.4, there are not significant differences between the values inside and outside the red ellipses in Fig. 2.2 and Fig. 2.3. The NDVI inside the red ellipses exhibits values lower than zero (typical values of desert cover) and are far from typical NDVI values of vegetation cover class (with values usually greater than 0.3).

Therefore, our assumption is that in this case, contrary to the natural behaviour of the coherence maps, low coherence does not represent only water or fields (Bruzzone

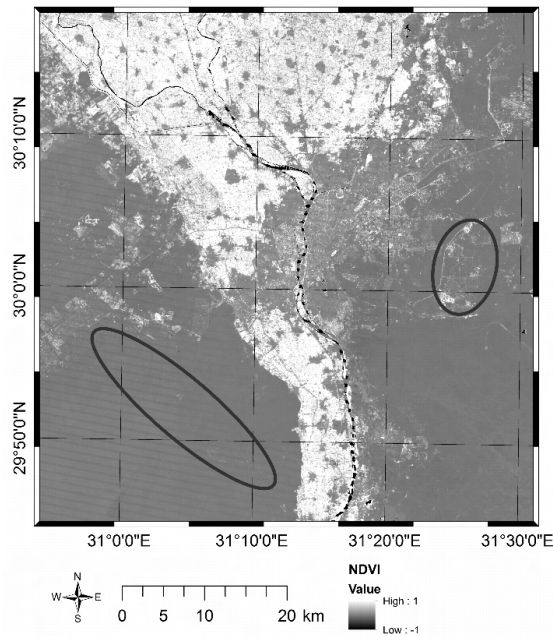


Figure 2.4: Normalised Difference Vegetation Index derived from Landsat 7 ETM+ 2010 data.

et al., 2004) but also areas where other activities are ongoing (Milisavljevic et al., 2010). The same effect is applicable to the SAR amplitude indicators: in our case, high values of the SAR temporal variability are not only linked to water and vegetation. Hence, we define a new land use class for detecting these areas and differentiating them from other classes.

This chapter proposes the analysis of the optical and SAR data fusion for land use classification over Greater Cairo and Giza to overcome the aforementioned limitations. In addition, we also checked if the introduction of a new land use class could better capture the differences between the optical and SAR based techniques (reported in (Delgado Blasco et al., 2013)). This new class may represent areas with human induced changes, that could be permanent or transitory, such as open pits, roads eventually covered by sand and ongoing building activities among others. This new class has been called 'Undefined Anthropogenic Disturbances' (UAD) and is mainly located in desert areas.

In this chapter, the effect of optical and radar satellite data fusion in medium spatial resolution is and applied to analyze the multi-temporal evolution of the urban extension of Greater Cairo for the period from 1998 to 2015.

2.2. Study area and remote sensing datasets

The study area is centred on Greater Cairo and its surroundings, which covers a total area of approximately $50 \times 50 \text{ km}^2$ (Fig. 2.5).

In the last decades, the informal construction (Meikle, 2011) increased dramatically, threatening the Giza's Pyramids World Heritage site. Therefore, we have focused on analyzing the built-up increase in the Pyramids Gardens area, named Hadayek Al Ahram, as well as in the entire Greater Cairo for which their results are analyzed individually.

In addition, due to the Arab Spring occurring in Egypt on January 2011, both periods before and after Arab Spring will be considered for analysis, since different behaviour in urban dynamics could be expected a priori.

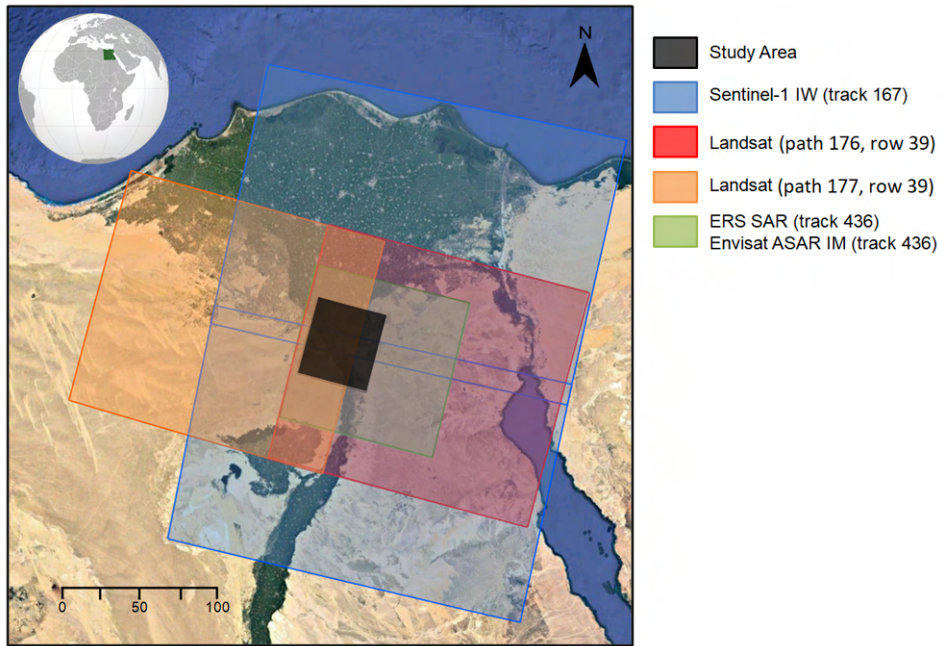


Figure 2.5: Location of the study area in Greater Cairo, Egypt.

We used the freely available archives of Landsat 5 TM, 7 ETM+ and 8 OLITIRS multispectral data, as well as ERS1/2, Envisat and Sentinel-1 SAR data. The selected SAR datasets comprised the full archive of ERS-1/2, Envisat ASAR satellites, both in track 436, and Sentinel-1 on track 167, jointly covering the entire period from 1992 to 2015. The chosen optical satellite imagery was Landsat 5 TM (1998 data), 7 ETM+ (2004 and 2010 datasets) and 8 OLITIRS (2015 data). The specific information is shown in Table 2.2.

Table 2.2: The selected satellite remote sensing imagery.

Acquisition date	Sensor	Path / Track	Spatial resolution (m)	Signal characteristics	N. images
1998-09-11	Landsat 5 TM	176 / 39	30 x 30	Visible, NIR, SWIR-1/2, Thermal	1
2004-04-12 / 2004-07-17	Landsat 7 ETM+	176,177 / 39	30 x 30	Visible, NIR, SWIR-1/2, Thermal	4
2010-05-15 / 2010-06-07	Landsat 7 ETM+	176,177 / 39	30 x 30	Visible, NIR, SWIR-1/2, Thermal	4
2015-07-24	Landsat 8 OLI/TIRS	176 / 39	30 x 30	Visible, NIR, SWIR-1/2, Thermal	1
1992-06-01 / 2001-01-04	ERS-1/2 SAR	436	4 x 20	Microwave (C band)	6
2003-11-20 / 2010-09-09	Envisat ASAR IS2	436	4 x 20	Microwave (C band)	18
2015-01-01 / 2015-12-31	Sentinel-1 IW SLC	167	20 x 4	Microwave (C band)	45

2

2.3. Methodology

In order to study the land cover dynamics based on the data fusion of SAR and optical data, the implemented methodology follows this three steps (Fig. 2.6): (i) data preparation; (ii) land use classification; (iii) temporal evolution analysis of the obtained classification maps.

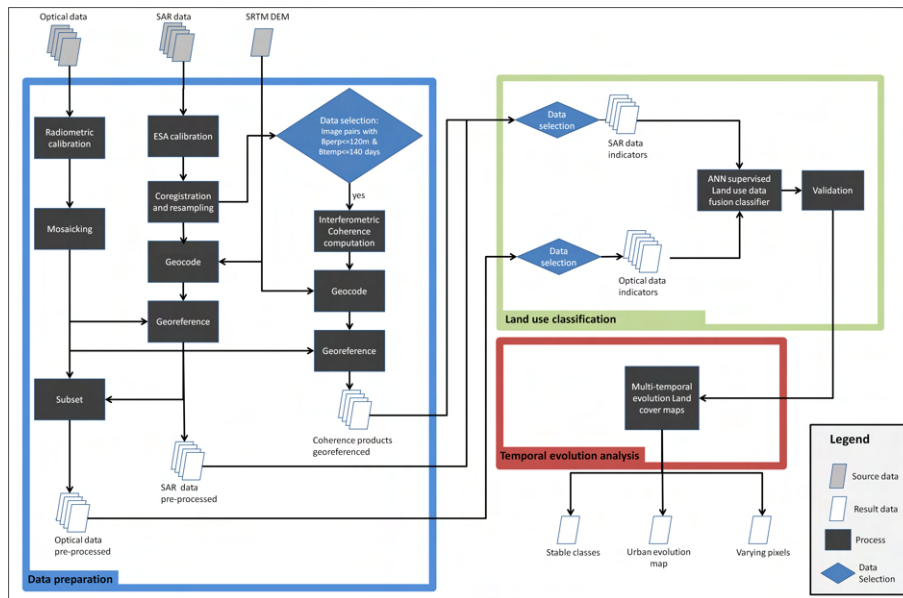


Figure 2.6: Methodology flow diagram for analyzing the land use dynamics by fusing SAR and optical imagery.

2.3.1. Data preparation

The first step is preparing the various datasets. Initially, ERS SAR and Envisat ASAR imagery are calibrated considering the incidence angle, look angle and the antenna pattern using ESA specifications implemented in the Next ESA SAR Toolbox (NEST) (ARRAY, 2010). Then, coregistration, resampling, interferometric coherence computation and geocoding are performed using the DORIS interferometric software from Delft University of Technology (Kampes et al., 2003). Precise orbits are used to recompute orbital information in order to reduce the coregistration errors. ERS-1/2 and Envisat precise

orbits were from Delft Earth Observation and Space Systems (DEOS). The interferogram image pairs are selected for the subsequent computation of the interferometric coherence based both on short temporal and perpendicular baseline criteria (maximum of 140 days and 120 m respectively for this study). Coherence can be affected by temporal, spatial and thermal decorrelation factors (Zebker et al., 1992). Hence, a short temporal baseline ensures that there will be minimum changes present in our scene due to the physical changes, and having a short perpendicular baseline minimizes geometric decorrelation (Zebker et al., 1992). This short temporal and perpendicular baseline condition is required to enable the preliminary identification of urban, desert and field areas using the interferometric coherence (Bruzzone et al., 2004). It is worth mentioning the seasonal effects of the sand storms characteristic of our study area around March-April every year. Hence, coherence maps with images acquired during the period with a higher frequency of sand storms in the region (i.e. March-April) were rejected for further analysis. Sand storms minimally affect the SAR C-band backscatter as only a thin layer of sand is moved, but it does affect the interferometric coherence of the affected desert areas as their changes are detectable with a drop of their coherence values (see Fig. 2.7). Finally, calibrated SAR images and coherence maps are geocoded using SRTM DEM information (downloaded from the Consortium for Spatial Information (CGIAR-CSI)) in order to have them geometrically corrected.

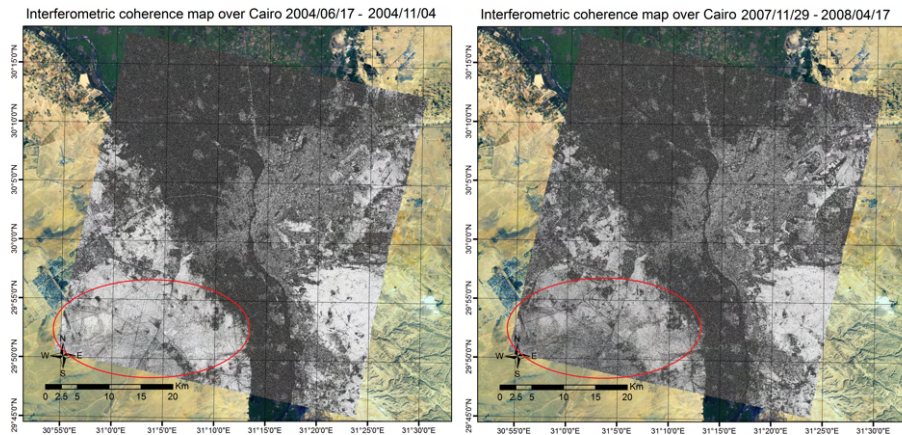


Figure 2.7: Coherence maps computed within SAR image pairs with low perpendicular baseline. The coherence map on the right is affected by sand storms that occurred during the period March-April 2008. This effect of the drop of coherence is visible in the desert areas, as inside the red ellipse.

In case of the Sentinel-1 data, similar approach to the ERS and Envisat data is followed, adapting for TOPSAR data using the SentiNel Application Platform (SNAP) (Veci et al., 2014) and using the Precise Orbits produced by the ESA Quality Control Group. In this case, all Sentinel-1 data could satisfy our requirements of maximum perpendicular and temporal baseline, so it has decided to take a temporal baseline of 120 days avoiding the aforementioned sand storm period. Processed data are then geocoded also using the same SRTM DEM employed for ERS and Envisat.

Radiance Landsat values are computed using the data provided in the Landsat

metadata using the radiometric calibration method suggested by USGS (Chander et al., 2009) and implemented in ENVI ESRI software. Four scenes are selected for 2004 and 2010, because of the scan line corrector failure (SLC-off) that occurred on 31st May 2003 (U.S. Department of the Interior, 2013). These four images were acquired within a maximum period of four months, minimizing the urbanization changes in such a short time period. Hence each group of four images is mosaicked in order to fill the gaps, since given any three Landsat 7 SLC-off images, there is a 90% probability that > 90% scene coverage can be achieved (Schneider, 2012).

Finally, all SAR images are georeferenced into the geometry of the Landsat data using 30 ground control points (GCPs) obtained by coregistering SAR with the Multi-spectral data. These GCPs are uniformly distributed all over the study area and represent road intersections on the satellite images. The final images are resampled using a first order polynomial, obtaining a final Root Mean Square Error (RMSE) lower than 1 pixel (30 m.) for all the different cases (Table 2.3). Optical images are finally cropped to match the SAR data over the study area. At the end of the data preparation all data are unified to the same image size and georeference system of the Universal Transverse Mercator (UTM) projection (Zone 36N) and Datum World Geodetic System 84 (WGS84).

Table 2.3: GCPs used in the SAR imagery georeferenciation step and RMS values

Dataset	Number GCPs	RMS error (pixels)
ERS SAR	30	0.97
Envisat ASAR	31	0.95
Sentinel-1 IW SLC	30	0.74

2.3.2. Land use classification

Four generic classes are proposed: (i) built-up area, hereafter named 'urban'; (ii) sandy and rocky desert combined in a 'desert' class; (iii) vegetation, crops, garden, grass and agricultural fields named as 'field' and; (iv) 'water' class mainly formed by Nile River and smaller water bodies present in the scene. In addition, we have also defined a new class named 'undefined anthropogenic disturbances' (UAD) that exploits the data fusion approach in order to identify areas inside the desert where anthropogenic disturbances are detectable, such as construction in early stages, cultural heritage sites, open pits and dirt roads (roads covered with sand). This class does not include finished man-made infrastructures. Hence, this class is expected to be characterized by having low coherence and high temporal variability of the radar signal, with high radiance values characteristic of soil and rocks in optical data (see Fig. 2.8).

Land use classification has been performed for computing land cover maps with the aforementioned five classes and finally, we have investigated the relationship between the UAD class with built-up areas classified in subsequent LULC maps.

In order to produce land use land cover (LULC) maps with SAR and optical imagery, neural network supervised classifier has been selected due to the higher accuracy reported by Chettri et al. (1992) and Cetin et al. (2004).

We decided to give equal weight to the information derived from each sensor in the mixed sensor approach. Hence, the designed data fusion supervised classifier have

equal number of input bands from the different sensors.

The SAR dataset is chosen according to the optical data acquisition dates (Table 2.2). Specifically, a group of SAR images is selected per optical image spanning one year around the date of the optical image. Two of these SAR images are expected to be able to produce an interferometric coherence product with both short temporal and perpendicular baseline (in this study with maximum of 105 m and 140 days).

The indicators to classify in the proposed LULC scheme were analyzed considering the peculiarities of the five-class problem addressed. Specifically, correlation of Landsat bands were performed, resulting in only four bands with correlation lower than 0.8 among them: Near Infra-Red (NIR), shortwave-1 (SWIR-1), shortwave IR-2 (SWIR-2) and thermal IR. Bands blue, green and red were highly correlated with SWIR-1. The Normalized Difference Vegetation Index (NDVI) was also introduced due to its capacity to distinguish between healthy fields among the other features. Consequently, we used five optical indicators, corresponding to the less correlated bands NIR, SWIR-1, SWIR-2, Thermal and the NDVI (see Landsat band specifications in Tab 2.4).

Table 2.4: Landsat bands correspondence with Red, Near Infra-Red, Short Infra-Red (1 and 2) and Thermal Infra-Red bands (USGS, 2021)

Satellite	Landsat 5 TM		Landsat 7 ETM+		Landsat 8 OLI/TIRS	
	band	wavelength (μm)	band	wavelength (μm)	band	wavelength (μm)
RED	3	0.63-0.69	3	0.63-0.69	4	0.636-0.673
NIR	4	0.76-0.90	4	0.77-0.90	5	0.851-0.879
SWIR-1	5	1.55-1.75	5	1.55-1.75	6	1.566-1.651
SWIR-2	7	2.08-2.35	7	2.09-2.35	7	2.107-2.294
Thermal-IR	6	10.40-12.50	6	10.40-12.50	10	10.60-11.19

In order to select the five indicators from SAR data, the multi-temporal behaviour of the SAR signal and its relationship with the analyzed classes are analyzed based on Wegmüller et al. (2000); Bruzzone et al. (2004). Essentially, desert and urban classes can be identified based on the low temporal variability of the backscattering coefficient compared to most other cover types. In contrast, the water and field classes showed high temporal variability because of their variations with seasons, rain and vegetation growth. Therefore, indicators based on the estimation of temporal variability were chosen as input for the supervised classifier. In addition, interferometric coherence was also selected due to its effectiveness in identifying urban areas as reported in other studies (Strozzi and Wegmüller, 1998).

Therefore, the input data selected for the classifier consists in 5 information bands of the multi-spectral imagery and 5 information bands derived from the SAR datasets, as follows: (i) near IR; (ii) shortwave IR-1; (iii) thermal IR; (iv) shortwave IR-2; (v) NDVI (Eq. (2.1)); (vi) temporal average calibrated SAR in decibel scaled (dB) (Eq. (2.2)); (vii) temporal standard deviation of calibrated SAR signal per pixel in dB (Eq. (2.3)); (viii) normalized temporal standard deviation in dB (Eq. (2.4)); (ix) ratio of maximum to minimum calibrated SAR signal per pixel (Bruzzone et al., 2004) defined as Eq. (2.5)

and; (x) interferometric coherence (Hanssen, 2001) defined as in Eq. (2.6);

$$NDVI = \frac{NIR - RED}{NIR + RED} \quad (2.1)$$

From Eq. (2.1), NIR corresponds with the Near Infra-Red band, RED with the Red band, for the different Landsat satellites. Specific information found in Tab. 2.4.

Table 2.5: Formulas of the 5 selected bands of SAR derived information employed as input in the LULC ANN classifier. Each index is calculated within the temporal data series of each pixel i for N images and L represents the window size employed in the interferometric coherence computation.

Indicator	Formula
Backscatter average	$\sigma_{avg,i} = 10 \log_{10} \frac{1}{N} \sum_{k=1}^N \sigma_{k,i}$ (2.2)
Backscatter standard deviation	$\sigma_{std,i} = 10 \log_{10} \sqrt{\frac{1}{N-1} \sum_{k=1}^N (\sigma_{k,i} - \sigma_{avg,i})^2}$ (2.3)
Normalized standard deviation	$\sigma_{normstd,i} = 10 \log_{10} \left(\frac{\sigma_{std,i}}{\sigma_{avg,i}} \right)$ (2.4)
Maximum-minimum backscatter ratio	$R_i = 10 \log_{10} \left(\frac{\sigma_{max,i}}{\sigma_{min,i}} \right)$ (2.5)
Interferometric coherence	$ \hat{\gamma}_i = \frac{ \sum_{k=1}^L A_{M_k} \cdot A_{S_k}^* }{\sqrt{\sum_{k=1}^L A_{M_k}^2 \cdot A_{S_k}^2}}$ (2.6)

Fig. 2.8 shows qualitatively the expected distribution of the five classes in the interferometric coherence and Shortwave IR-2 (SWIR-2) feature space derived from the SAR and optical sensors. It is noteworthy that the UAD class has low coherence values such as water and field classes, but also high values in SWIR-2 such as desert. Hence, only a combination of sensors would detect this new class.

As mentioned before, the classifier is designed based on artificial neural networks for land use classification. Among the different network typologies, the feed-forward back-propagation multi-layer perceptron (MLP) was selected, being the most commonly used neural network for remote sensing (Atkinson and Tatnall, 1997). It has shown its successful application for land cover classification purposes (Simone et al., 2002; Del Frate et al., 2007).

Concerning the number of nodes (named neurons) in the hidden layer, we selected for our study the heuristic by Kanellopoulos and Wilkinson (1997) and Hush (1989), in which the number of neurons in hidden layer is equal to 3 times the number of input bands.

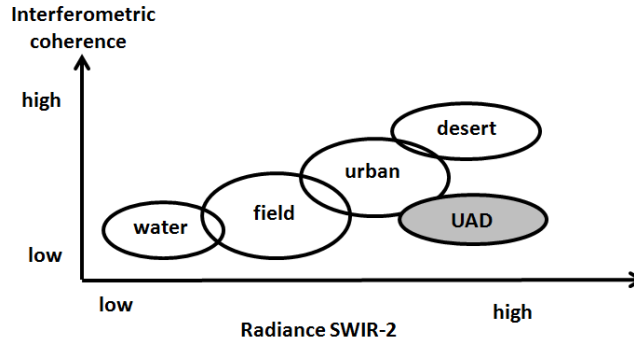


Figure 2.8: Qualitative classes distribution in the interferometric coherence and short-wave infrared (SWIR-2) feature space.

2.3.3. Validation approach

The validation of the classification maps is performed by visual inspection of the very high resolution imagery (< 3 meters) copyrighted by Digital Globe and available in Google Earth, selecting different point sets for the time periods 2004 and 2010, specifically 2661 and 2129 points respectively. It is possible to do this due to the historical dataset available that goes back to the year 2000. Hence, results obtained for 1998 could not be validated using this approach. We computed the accuracy of the final classification maps using the overall accuracy (or overall success rate) and also the agreement occurring by chance using the kappa index (Cohen, 1960), as performed by Congalton (1991) and Mather and Koch (2004).

Our assumption is that 1998 results behave in the same manner that for 2004, 2010 and 2015 as we have employed the same methodology to produce the LULC maps.

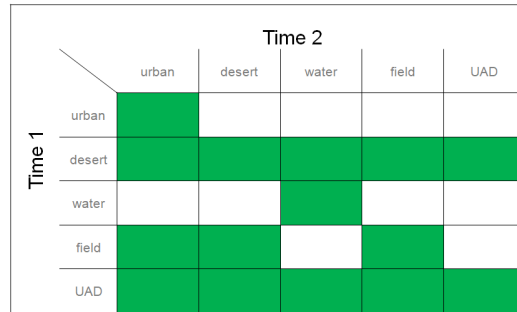
In our attempt to employ independent validation of our results, we use the Global Urban Footprint (GUF) provided by the German Space Agency (DLR) that was computed using TerraSAR-X data at 3 meters resolution for 2012, as well as the recent Prototype of Sentinel-2 Land Cover Map of Africa at 20 meters released by the ESA Climate Change Initiative (ESA-CCI).

The validation of the 2015 land cover maps, was done by comparing only our urban class with the GUF, and also comparing the common classes with the ESA-CCI Land Sentinel-2 Prototype Map of Africa after aggregating the vegetation classes into a single one to match with our four classes 'urban', 'desert' with the bare soil (ESA-CCI), 'water' and 'vegetation'.

2.3.4. Temporal evolution analysis

After obtaining the five-class LULC maps for the different time periods, we identify pixels that remained stable and those that underwent changes from one land use class to another between 1998 and 2015. Non-realistic changes are also detected and labelled as mis-classified pixels, by assuming that: 1) once a pixel is urban, it will stay urban in the following periods; 2) water cannot turn into urban, field or desert; 3) fields can

only become urban or UAD, but not desert or water. In our study area the water class mainly correspond to the River Nile, and has been stable during the considered time period. Fig. 2.9 shows the possible transitions of land use class between consecutive LULC maps.



		Time 2				
		urban	desert	water	field	UAD
Time 1	urban	Green				
	desert	Green	Green	Green	Green	Green
	water			Green		
	field	Green	Green		Green	
	UAD	Green	Green	Green	Green	Green

Figure 2.9: Accepted land transitions in consecutive LULC maps

2.4. Results

2.4.1. Land use classification

The resulting supervised land use classifications maps are shown for 1998 and 2015 in Fig. 2.10. Their analysis can be found in the discussion section.

Table 2.6: Confusion matrix, kappa index and overall accuracy of the resulting land use maps. Google Earth data is used as ground truth.

Year	GoogleEarth ground truth	Land use classification map					Accuracy criteria
		Urban	Desert	Water	Fields	UAD	
2004	Urban	369	32	0	32	4	kappa index (%)
	Desert	96	1121	2	29	38	82.47%
	Water	1	0	52	9	0	Overall accuracy
	Fields	42	4	2	789	5	88.54%
	UAD	1	8	0	0	25	
2010	Urban	342	37	1	20	0	kappa index (%)
	Desert	50	890	0	8	15	86.24%
	Water	3	0	30	5	0	Overall accuracy
	Fields	45	4	0	643	2	90.93%
	UAD	0	3	0	0	31	

The kappa index shows very good or almost perfect degree of accuracy according to Altman (1991) and Landis and Koch (1977) respectively (higher than 0.80 or 80%) for both 2004 and 2010 land cover maps.

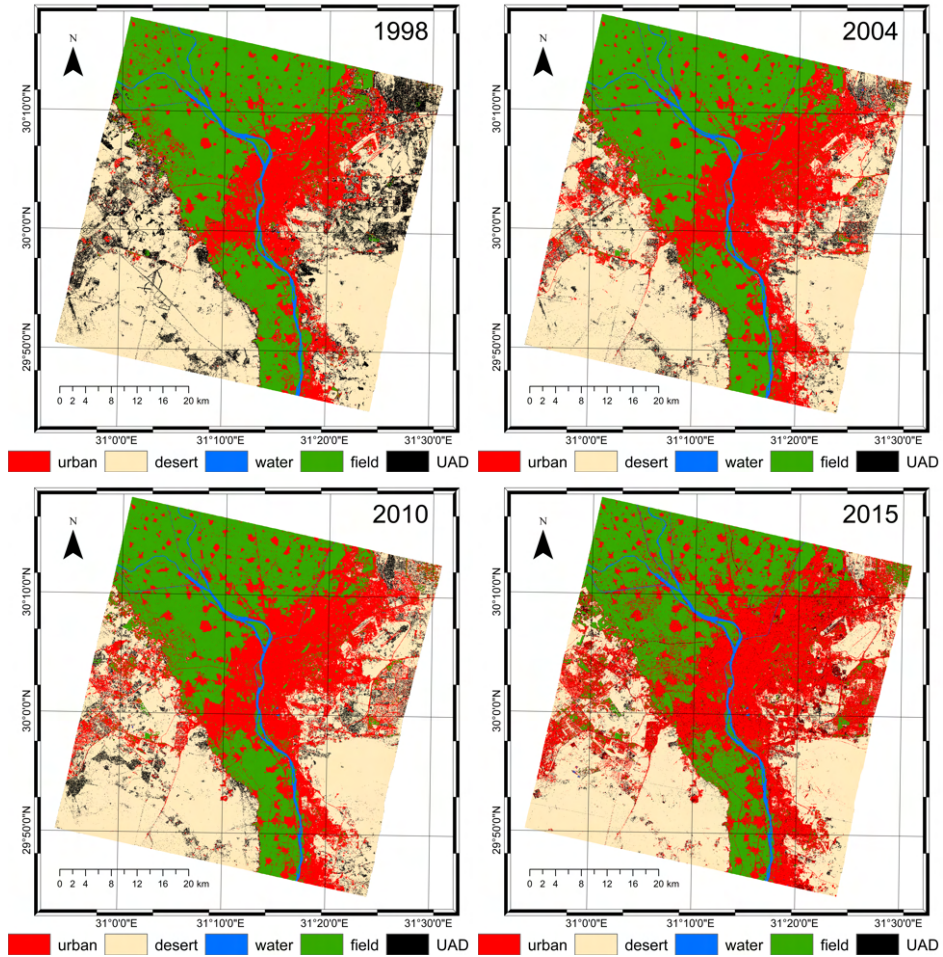


Figure 2.10: Land use classification maps obtained for 1998, 2004, 2010 and, 2015. UAD class (in black) detects the areas which had suffered any change during the analyzed period.

For evaluating the goodness of our approach, the 2015 LULC map was compared with the GUF provided by DLR over our study area, created with TerraSAR-X data at 3 meters resolution for 2012 and with the ESA CCI Prototype African LULC map computed with Sentinel-2 data from 2016 at 20 meters resolution. Note that both datasets are higher resolution than our results (30 meters) and not matching totally on the observed time (Fig 2.11).

Both GUF and ESA-CCI Land Cover map were resampled with at 30m and reprojected in UTM coordinates and clipped over our study area to ensure pixel to pixel matching. For the comparison between the different datasets we should consider that: i) both are produced with single sensor approach and our maps not; ii) Original spatial resolution is higher than ours, so we expect that these maps from ESA and DLR are able to detect

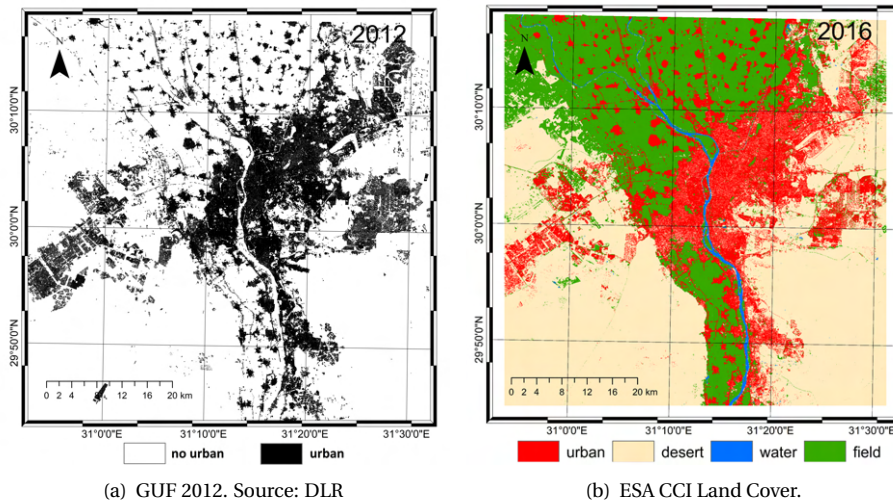


Figure 2.11: Global Urban Footprint (left) and ESA-CCI Prototype Land Cover of Africa (right) employed for evaluating the goodness of our data fusion approach.

smaller features than ours. Still, we consider necessary to compare with real products that can be nowadays found.

In addition, as the GUF is computed using data from 2012, our latest map from 2015 should contain the GUF detected features, as we also assumed that urban is an invariant class. In addition, we measure the same but for comparing the GUF with the ESA-CCI of Africa, finding interesting values, as shown in Tab. 2.7.

Table 2.7: Percentage of match between the 2012 GUF's urban class and the 4-classes aggregated ESA-CCI Land Cover map of Africa 2016 and our 5-classes Land Cover map for 2015.

		ESA-CCI 2016				Our LULC map 2015				
		Urban	Desert	Water	Fields	Urban	Desert	Water	Fields	UAD
GUF 2012	Urban	73.05	24.00	0.003	2.92	79.8	6.14	0.20	8.88	4.98

Tab. 2.7 shows that our LULC map obtained for 2015 is in agreement almost at 80% with the urban class detected in the GUF, being this agreement higher than the obtained between GUF and ESA-CCI Land use of Africa. In addition, large part of urban in the GUF is detected as bare areas / sand areas in the ESA-CCI Land use class, proving that optical sensor have problems in detecting features inside arid/desert areas as mentioned in the introduction.

In addition, we computed the Confusion Matrix between 2500 random pixels of the aggregated version of the ESA-CCI Sentinel-2 Prototype (which only 2442 felt into classified pixels in our LULC map) with our LULC map of 2015 which detailed values are

in Tab 2.8, showing a near 80% of agreement (overall accuracy) and 69.20% of Kappa Index, categorised as good level of agreement (Altman, 1991). In addition, it is worth to highlight that many pixels classified as desert (bare soil) on the ESA-CCI Prototype dataset in our approach are identified as 'urban' or 'UAD'.

Table 2.8: Confusion matrix, kappa index and overall accuracy of the 2015 resulting land use map with respect to the ESA-CCI Sentinel-2 Prototype Land Cover Map Africa at 20m used as ground truth.

Our LULC map 2015	Sentinel-2 Prototype LC map				Accuracy criteria
	Urban	Desert	Water	Fields	
Urban	371	198	0	99	kappa index (%) 69.20%
Desert	6	1022	0	9	
Water	1	3	19	11	Overall accuracy 79.81%
Fields	56	7	0	537	
UAD	22	72	0	9	

Zooming into the different maps to understand what is happening (see Fig 2.12), we see that in fact the ESA-CCI Land use of Africa missed many urban features, already detected in the GUF, and later detected in our map. In addition, the ESA-CCI also identifies as desert many urban pixels located within the cities. Moreover, the GUF and the ESA-CCI Land use map of Africa are not detecting as urban, among others roads, the part of the *Ring Rd* located behind the Pyramids Garden area, and others crossing desert areas, while with our approach it is clearly detected.

The spatial extents and locations of the results showed in Fig. 2.15 and Fig. 2.18 are represented in Fig. 2.13.

2.4.2. Temporal evaluation of the classified land use/cover maps

The land use maps were analyzed in order to ensure the feasibility of the existence of different classes based on their evolution. Therefore, a comparative analysis was done taking into account all the classification maps for identification of mis-classified pixels. The 1998, 2004 and 2010 classification maps were analyzed together and it was established that changes have to stay coherent for the whole time span analyzed. As a result, both the urban expansion and the stable areas in Greater Cairo are computed and mapped (see urban evolution map in Fig. 2.14).

The analysis of the Hadayek Al Ahram (Pyramids Garden) is done splitting the period before and after 2010. We suspect that the Arab Spring could have an effect also in the natural evolution behavior of this area.

Stable areas around the Giza Pyramids (Fig. 2.15, left) show the detected permanent UAD areas from 1996 until 2010, confirming the assumption that UAD class would include Cultural Heritage sites with intense transit of visitors. In addition, the Fig. 2.15 right, shows that the built-up evolution in Hadayek Al Ahram area increased much more during the period from 2005 to 2010 than before.

By applying these criteria three groups were found: (i) stable (non-varying); (ii) varying and; (iii) misclassified pixels. The non-varying pixels are 69% and the varying ones

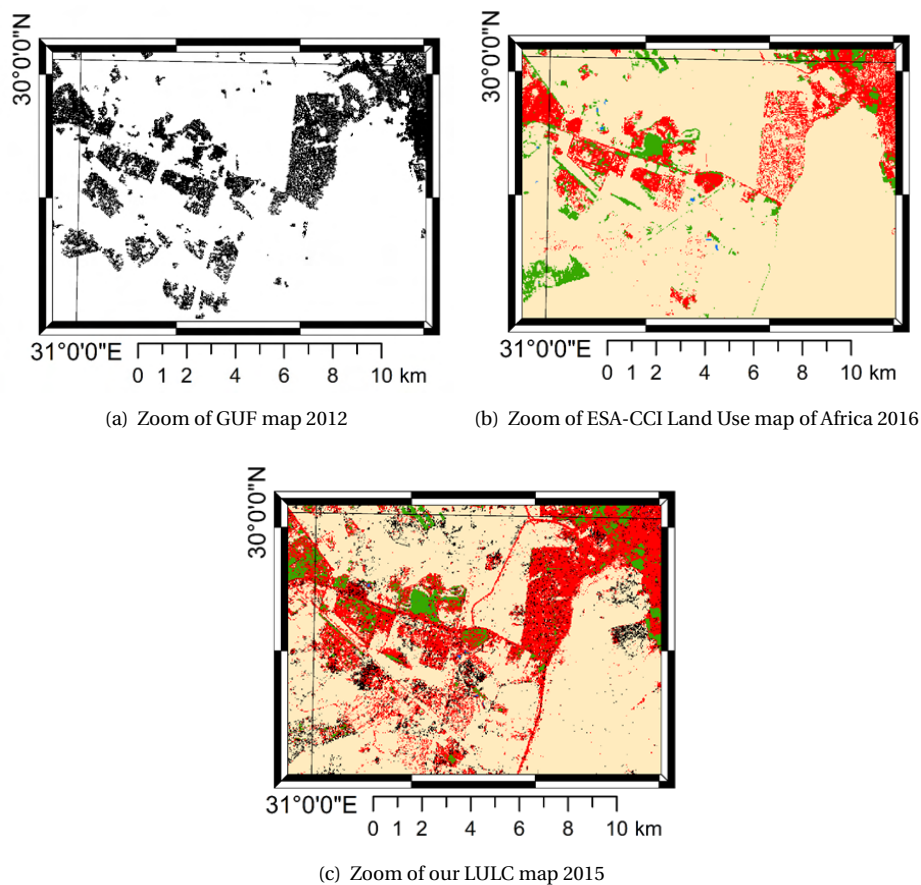


Figure 2.12: Zoom on the Giza Pyramids area and 6th October City for GUF 2012 (a), ESA-CCI 2016 (b)) and our LULC map 2015 (c). Urban is colored black in GUF map (a) and red in ESA-CCI (b) and our LULC map (c).

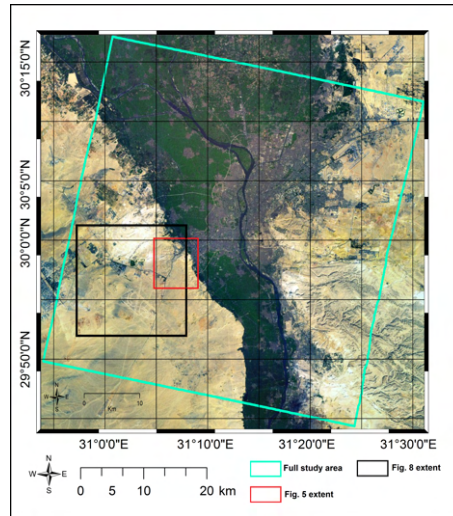


Figure 2.13: Spatial extents for full area of study (cyan), Fig. 8 (red) and Fig. 9 (black).

are 22%. Therefore, the total misclassified pixels are the 8% of the total number of pixels. Fig. 2.15 shows that the site of the Giza Pyramids is classified as stable UAD class. Hence, this supports our hypothesis that UAD represents Cultural sites with intense transit of visitors as well.

In 2010, the total constructed area equals 655 km^2 which corresponds to an increase in built-up areas of 72% since 1998. Of the 274 km^2 of newly constructed areas, 37% are situated in former desert areas. Between 2004 and 2010, half of newly constructed area is situated in the Nile floodplain (49%), while in the desert is 33% and 18% in UAD (see Tab. 2.9). This matches results obtained by de Noronha Vaz et al. (2011a), where the construction activities in the floodplain appeared to be more important than in the desert for the more recent time period. Moreover, in 2010 around 100 km^2 are identified as undefined anthropogenic disturbances (UAD), and part of this extension is identified as urban in 2013 (Fig. 2.18).

2.4.3. Built-up sprawl in Hadayek Al Ahram (Pyramids Gardens)

The results of the built-up expansion obtained from the temporal evolution analysis are detailed in Table 2.9.

In 1998, the built-up extent in Hadayek Al Ahram was about 1.01 km^2 . However, from 1998 to 2010, the built-up extent increased by 4.4 km^2 , occupying over 400% more area in 2010 than in 1998. In this case, since the Pyramids Gardens area is located completely inside the desert plateau, the new constructions appeared in desert and UAD detected areas in the previous LULC maps. During the period from 1998 to 2004, one third of the total constructions were built up, while in the period from 2004 to 2010 the growth accelerated, with the identified new constructions of this period more than two times that observed in the previous period (Table 2.9). Finally, for the latest period analyzed, the growth still continued with an intermediate rate, increasing the built up in 2.6 km^2 ,

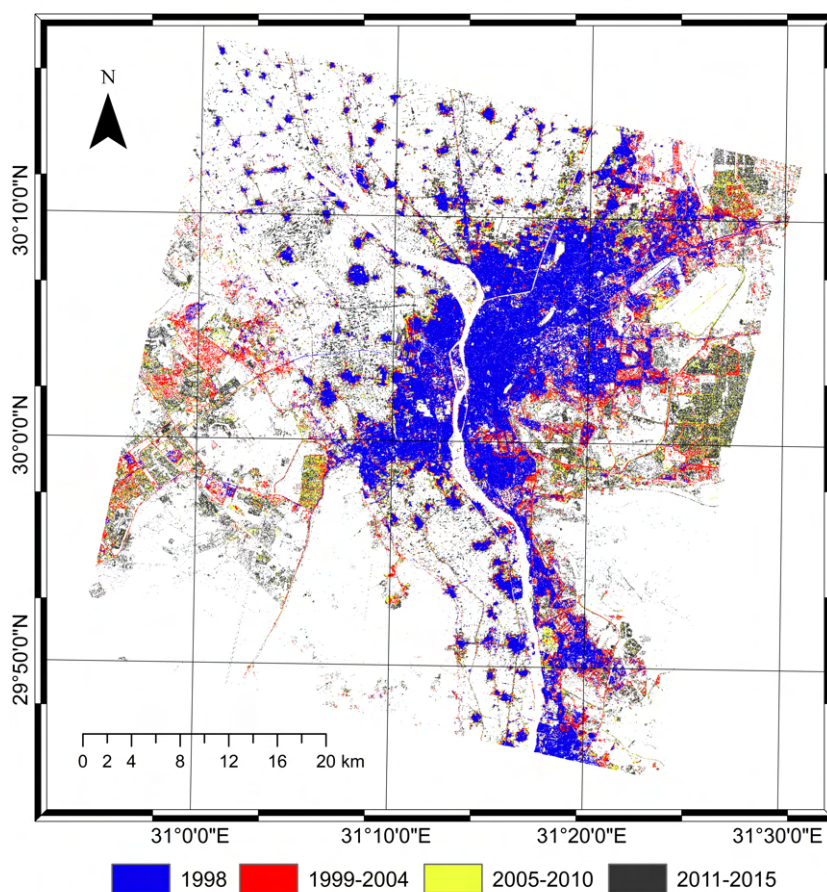


Figure 2.14: Built-up evolution of Greater Cairo since 1998 to 2015 computed considering the criteria described in section 2.3.4. Floodplain is located between the desert edge lines. Desert is located at west and east of the respective left and right desert edge lines.

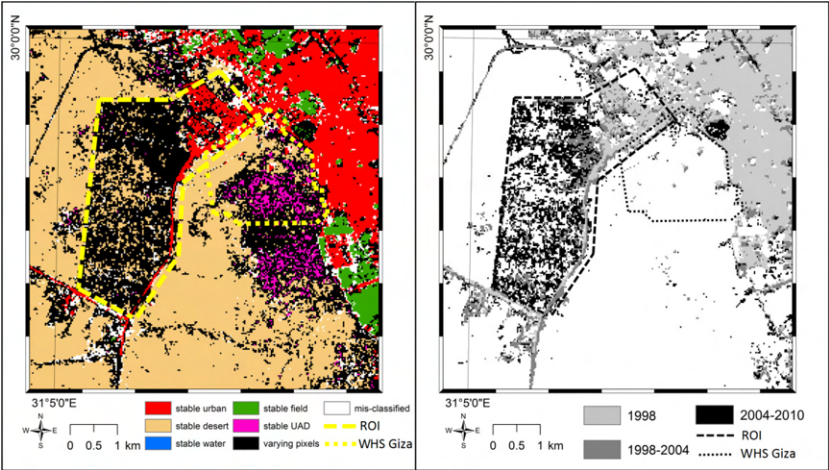


Figure 2.15: Zoom of stable areas(left) and built-up evolution (right) in Hadayek Al Ahram area (ROI) obtained from 1996 until 2010.

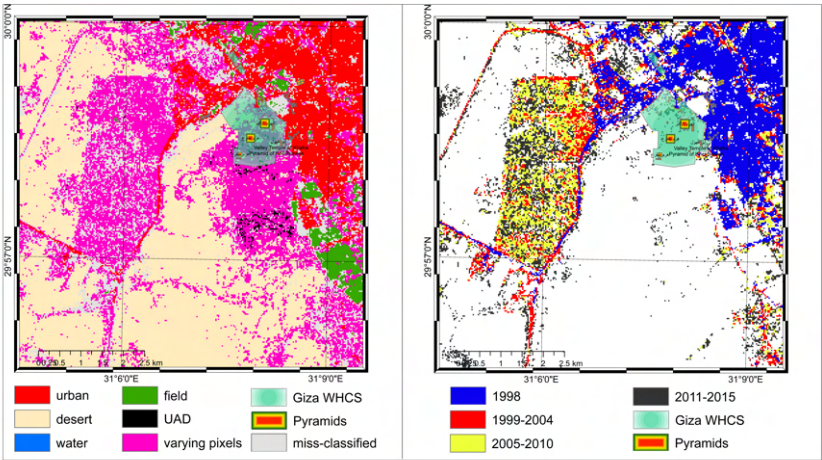


Figure 2.16: Zoom of stable areas(left) and built-up evolution (right) in Hadayek Al Ahram area (ROI) obtained from 1996 until 2015.

Table 2.9: Origin of new built-up areas (km²) for Greater Cairo and Hadayek Al Ahram area. Values obtained from the temporal evolution analysis considering only feasible changes.

Class	Greater Cairo				Hadayek Al Ahram			
	1999-2004	2005-2010	2011-2015	subtotal	1999-2004	2005-2010	2011-2015	subtotal
Desert	47.6	32.0	97.4	177.0	1.1	1.9	2.0	5.0
UAD	41.9	15	33.8	90.7	0.4	1.0	0.6	2.0
Field	35.4	39.8	84.5	159.7	-	-	-	-
subtotal	124.9	86.8	215.7	427.4	1.50	2.9	2.6	7.0

2

making a total computed growth during the period from 1998 to 2015 in 7 km², being a 700% of increase with respect to the urban detected at 1998.

In addition, our results shows that among the consequences of the Arab Spring on Egypt, we have observed a reduction of the activities around the Giza World Heritage Cultural Site (WHCS). Until that day, the Giza WHCS appeared as permanent UAD class (Fig. 2.15), while including the period until 2015, only a small part of it continue being permanent UAD (Fig. 2.16). Fig 2.17 illustrates the reduction of the number of arrivals of international tourists (The World Bank Group, 2017), that supports our assumption regarding the reduction of tourists visiting the Pyramids.

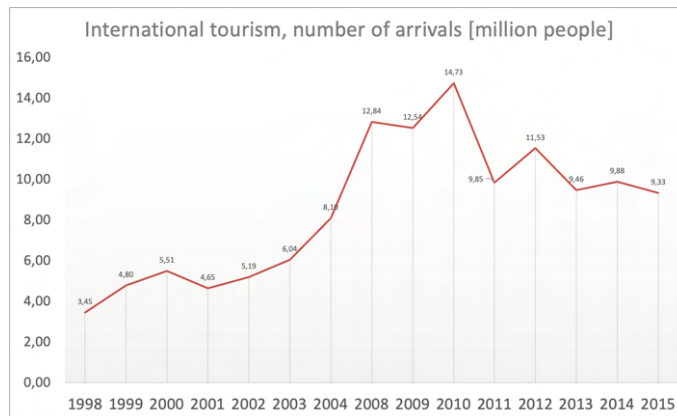


Figure 2.17: Tourist arrival in Egypt data, showing a decrease after Arab Spring in January 2011.

2.5. Discussion

The proposed data fusion approach enables to identify areas where undefined anthropogenic disturbances are potentially going on, such as early construction stages of new buildings (black pixels in Fig. 2.10). Moreover, the UAD class also represents arid areas of transit like dirt roads (asphalt roads eventually covered with sand) or areas with high human activity in cultural heritage sites, such as the surroundings of the Giza Pyramids area (Fig. 2.15).

Fig. 2.14 shows the temporal evolution of the built-up areas in the Greater Cairo region. In 1998, almost no built-up area was constructed outside the floodplain, but since the government started encouraging people to construct in arid areas, the new built-up area grew both inside and outside the floodplain, being the growth in the desert between 1998 and 2004 more significant. Despite government efforts, construction has not stopped in the floodplain.

The UAD class shows values in the thermal infrared similar to the ones measured for 'urban' and 'desert' classes. In addition, the UAD areas has as low coherence values as the ones found in 'water' and 'field' classes. This means that this new UAD class represents areas that had changed during the analyzed time period. It is remarkable that the new class completely overlaps the other classes and, therefore, its detection is only possible with the proposed data fusion approach.

The evolution of the detected areas classified as undefined anthropogenic disturbances is also analyzed. 17 km² of permanent areas of UAD have been detected during the period between 1998 to 2010. These permanent areas can be attributed to intense transit in cultural heritage sites as well as open air mining activities or traffic in dirt roads. Since 2004, 16 km² of UAD areas appeared, which remained invariant up to 2010. In 2010, around 67 km² of new UAD areas appeared in desert areas. This increase may have been caused by the early stages of new construction works. Moreover, from 1998 to 2010, about 71 km² of new urban areas (26% of the total new built-up areas) were constructed in areas which had been classified as UAD in previous land use maps. These results also support our hypothesis that the UAD class represents construction areas in early stages of development because part of the detected UAD areas in one period, evolve into urban areas in the next one.

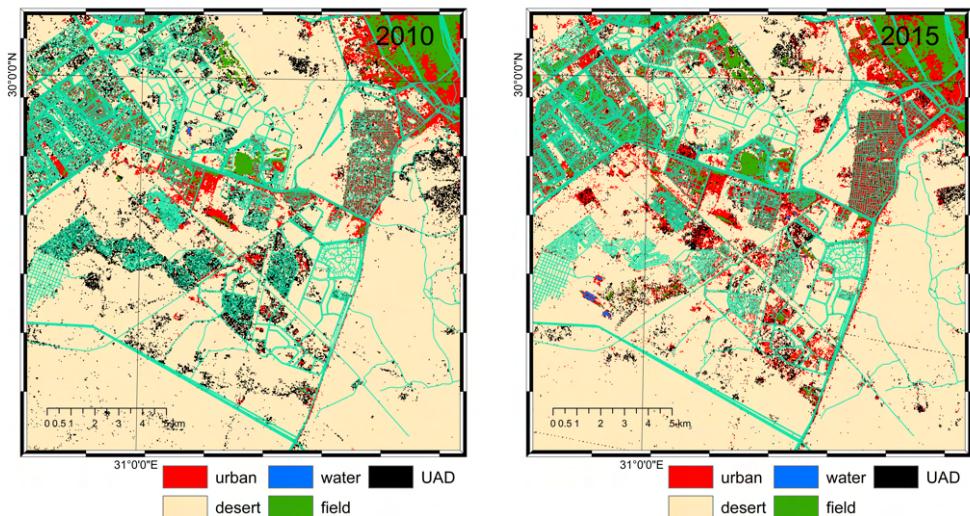


Figure 2.18: Zoom on the Western desert between Pyramids Garden and 6th October city, where UAD pixels were detected in 2010 (left) and 2015 (right), overlaid with the OpenStreetMap road layer of 2013, showing the correspondence between UAD and future built-up.

From 1998 to 2010, urbanization in both field and desert areas close to Cairo increased continuously. Between 1998 and 2004, new urban areas were constructed more in the nearby desert than in field areas, but the trend changed during the period from 2004 to 2010. However, in the land use map of 2010, 68 km² of UAD areas were detected in previously desert areas, part of which may become urban areas in the future (Fig. 2.18).

2.6. Conclusion

In this study we have applied a data fusion classification approach for quantifying the Greater Cairo urban sprawl from 1998 to 2010 with medium resolution optical and SAR data. This is useful in detecting areas affected by anthropogenic activities even if the natural environment does not show a significant change using only medium resolution optical imagery from space. This is only valid for short time lapses and short baselines in the image pairs used in the interferometric coherence computation. The individual limitations of SAR and optical images in detecting UAD areas in the desert have been overcome by mixing both sensors and defining a new class.

Including the new UAD class made it possible to detect construction areas at early stages. Also areas disturbed by other activities than building, such as the intense pressure related to tourist activities at the Giza Pyramid plateau were identified within this class. The identification of UAD is helpful for determining the built-up extension of rapidly changing environments such as Greater Cairo.

The extent of built-up areas in Greater Cairo increased by 73% between 1998 to 2010, corresponding to an average annual growth rate of 4.7%. However, an increase of 500% in 13 years is detected at Hadayek Al Ahram (Pyramids Gardens), at close proximity to the Giza Pyramids.

The potential of this data fusion approach requires the availability of suitable optical and SAR data. With the new generation of remote sensing satellites, higher resolution SAR and optical data is available, facilitating a more detailed analysis of the land cover dynamics in both temporal and spatial resolution.

Land cover dynamics in the Nile Valley and Middle Egypt

A good understanding of the landscape dynamics in Egypt should not be only focused on the analysis of the Capital and surroundings, but also analyze the changes in rural areas. To this aim we had applied similar methodology on data fusion land cover classification on the Middle Egypt region.

3.1. Introduction

Over the next 25 years, the world's population growth is expected to be concentrated in urban conglomerates within the developing world (Vermeiren et al., 2012). The challenges in achieving sustainable urban development will be particularly significant in Africa (Cohen, 2006; Cobbinah et al., 2015). Over the last decades, urban sprawl resulted in the loss of fertile soil for agricultural food production in the Egyptian Nile Valley. From the time of the 1996 population census onwards, the policy of the Egyptian government has been to avoid new constructions in the Nile floodplain, thus encouraging people to live outside the so-called 'green land' by settling in the arid areas of the eastern and western desert plateau (Sutton and Fahmi, 2001). Despite the restrictions introduced in 1996, inner-city slums have grown and informal settlements have bloomed on the urban fringes (Harris and Wahba, 2002).

Satellite remote sensing can provide rapid information to detect and map new built-up areas, and this information could be accessible by the decision-makers to act accordingly. Many studies have focused on urban sprawl for major centers around the globe (Schneider and Woodcock, 2008; Ward et al., 2000; Griffiths et al., 2010), including Africa (Vermeiren et al., 2012; Hou et al., 2016; Brinkmann et al., 2012). However,

This chapter has been published in *Remote Sensing* with the title *Mapping and Quantifying the Human-Environment Interactions in Middle Egypt Using Machine Learning and Satellite Data Fusion Techniques*, (Delgado Blasco, Cian, Hanssen and Verstraeten, 2020). To fit the publication in this study minor changes have been made.

increasing urbanization of the rural areas in the hinterland of major urban centers is less studied (Li, 2012; Inostroza et al., 2019).

Our aim is to analyze the landscape dynamics in Middle Egypt, which is an area of particular importance for several reasons. Compared to larger urban areas, such as Cairo, Middle Egypt is much more rural, yet experiencing a strong demographic trend (population increase) putting large pressure on arable land (see Fig. 3.1). Furthermore, the fertile Nile floodplain is a narrow strip (10–15 km) in an extensive desert area, leaving little space for urban and agricultural development. Next to loss of fertile land, the encroachment of desert areas by anthropogenic activities is, therefore, another major trend in land use.

In addition, to the west of the Nile floodplain, Middle Egypt is encroached by the South-Rayan dune field that stretches from the south of the Faiyum depression in an NNW-SSE direction (Embabi, 2004; Mohamed and Verstraeten, 2012). This dune-field contains barchan dunes migrating at a rate of 2–6 m per year (Mohamed and Verstraeten, 2012). Thus, desert dune dynamics at the interface of the floodplain may also lead to sand encroachment into the fertile floodplain (Willems and Dahms, 2017), and to anchored dunes within large vegetation fields. Moreover, the area is rich in archaeological sites that are threatened by the various land cover changes. Furthermore, the desert margin in Middle Egypt on the western side of the floodplain is also experiencing land reclamation efforts to increase the extent of arable land environments (Mohamed and Verstraeten, 2012).

Whilst many studies have been carried out to analyze Greater Cairo's urban area (de Noronha Vaz et al., 2011a; Hassan, 2011; Delgado Blasco et al., 2017; Mohamed, 2012a; Taubenböck et al., 2008; Osman et al., 2016; Stewart et al., 2004), little information is available on changes in land cover and, specifically, the urbanisation of the rural areas in the Nile floodplain upstream (or South) of Cairo. Some regional-scale studies (El-Bayomi, G., & Ali, 2015) have addressed land cover dynamics in this region, but little or no quantitative spatial information about the evolution of the urban extent of regional cities such as Mallawi is available (Wikipedia, 2018). The mixture of active or inactive sand dunes, tilled fields on reclaimed desert soils, as well as the construction of buildings in so-called 'mud bricks' makes a detailed analysis of land-use transformations in the Middle Egypt area challenging with optical imagery.

Together with other regions in Africa, Middle Egypt was mapped by the AFRICOVER project (Kalensky, 1998), using Landsat TM data acquired mainly in 1997. More recently, within the European Space Agency Climate Change Initiative (ESA-CCI), a land cover prototype of Africa has been produced using Sentinel-2 data acquired in 2016 (Lesiv et al., 2017). This approach showed the limitations of optical sensors in distinguishing spectral signatures of urban features made of materials similar to the ones composing the surrounding soil. This holds true for areas where buildings and roads are temporarily covered by sand or dust following intense sand storm events. Similar limitations for the classification of optical images were reported in past land cover classification studies (Stewart et al., 2004).

Previous studies have shown that the fusion of multi-spectral (including optical) remote sensing (MS) data in combination with Synthetic Aperture Radar (SAR) data may overcome this problem and can lead to improved land cover classification (Tupin, 2010;

Joshi et al., 2016). Given the amount of free multi-spectral and SAR data continuously acquired over the whole globe by different satellite missions, the fusion of the two types of data offers much potential. In this study, such a data fusion approach is followed to quantitatively analyze and map the landscape dynamics in Middle Egypt.

This work aims to create accurate land use land cover maps using the aforementioned data fusion approach to provide precise information about the evolution of urban and agricultural areas in Middle Egypt in relation to changes in population dynamics.

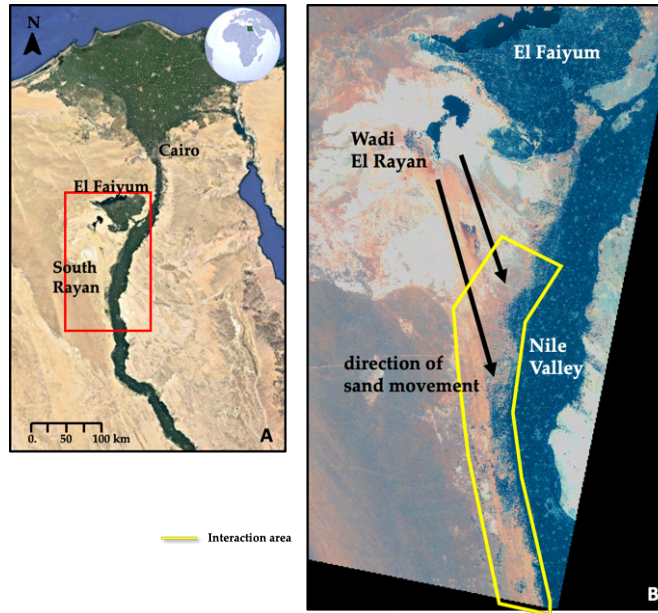


Figure 3.1: A) Google Earth image of Egypt indicating the location of B) within the red rectangle. B) False-color Landsat 8 OLI/TIRS image over the South-Rayan dune field and the direction of sand dune movement (source El Gammal and El Gammal (2010)), indicating the interaction area within the yellow polygon.

3.2. The Study Area

The study area is located in Middle Egypt (Figure 3.2) and includes part of the governorates of El-Minya and Asyut. It stretches from approximately 170 km to 280 km south of Cairo and comprises the regional cities of El-Minya, Mallawi and Dayrut from north to south. The study area comprises the Nile floodplain where almost all the urban areas and agricultural land is situated, but also a stretch of desert to the west and east.

Within the Nile floodplain, two major river channels are running south to north, i.e., the Nile River in the eastern part and the Bahr Youssef River in the western part. The latter branches of the Nile River near Dayrut is the main source of water flowing into the Faiyum depression in the North. The total study area comprised of 6170 km².

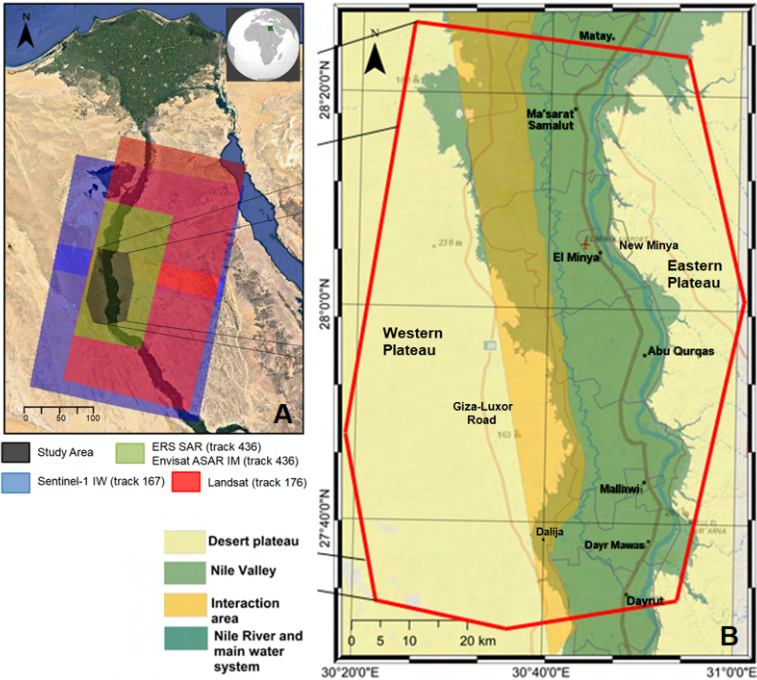


Figure 3.2: A) Location of the study area in Middle Egypt (black polygon), over the satellite imagery footprints (background image Google Earth). B) Detailed map of the study area highlighting the main cities and simplified representation of the landform regions.

3.3. Materials and Methods

In order to overcome the limitations of the optical sensors, we employed a satellite data fusion approach, combining Synthetic Aperture Radar (SAR) and optical multi-spectral data, covering the period from 1998 up to 2015 enabling the analysis of the human-environment interactions for almost three decades. Before 1998, there was not enough data available for the study area to apply this data fusion approach. Information on the selected SAR and optical data are provided in Table 3.1, whereas the footprint is shown in 3.2.

Table 3.1: The selected satellite remote sensing imagery.

LULC Map created	Acquisition date	Sensor	Path / Track	Spatial resolution (m)	Signal characteristics	N. images
1998	1997-05-15 / 1999-03-11	ERS-1/2 SAR IMS	436	4 x 20	C band, VV channel	12
	1988-01-01 / 1998-12-31	Landsat 5 TM	176 / 40,41	30 x 30	Visible, NIR, SWIR-1/2	39
2004	2003-11-20 / 2004-12-09	Envisat ASAR IS2	436	4 x 20	C band, VV channel	18
	2004-01-01 / 2004-12-31	Landsat 7 ETM+	176 / 40,41	30 x 30	Visible, NIR, SWIR-1/2	25
2010	2009-01-22 / 2010-08-05	Envisat ASAR IS2	436	4 x 20	C band, VV channel	18
	2010-01-01 / 2010-12-31	Landsat 7 ETM+	176 / 40,41	30 x 30	Visible, NIR, SWIR-1/2	16
2015	2015-01-01 / 2015-12-31	Sentinel-1A IW GRD	167	20 x 23	C band, VV channel	52
	2015-01-01 / 2015-12-31	Landsat 8 OLITIRS	176 / 40,41	30 x 30	Visible, NIR, SWIR-1/2	44

To analyze the land cover dynamics in the Middle Egypt region, the methodology employed can be described in the following three steps (Figure 3.3): (1) data preparation and extraction of land cover indicators; (2) spatio-temporal land use and land cover (LULC) mapping; (3) computation of urban and agricultural land cover changes, and changes in urban population density. Individual steps are further detailed in the following sections.

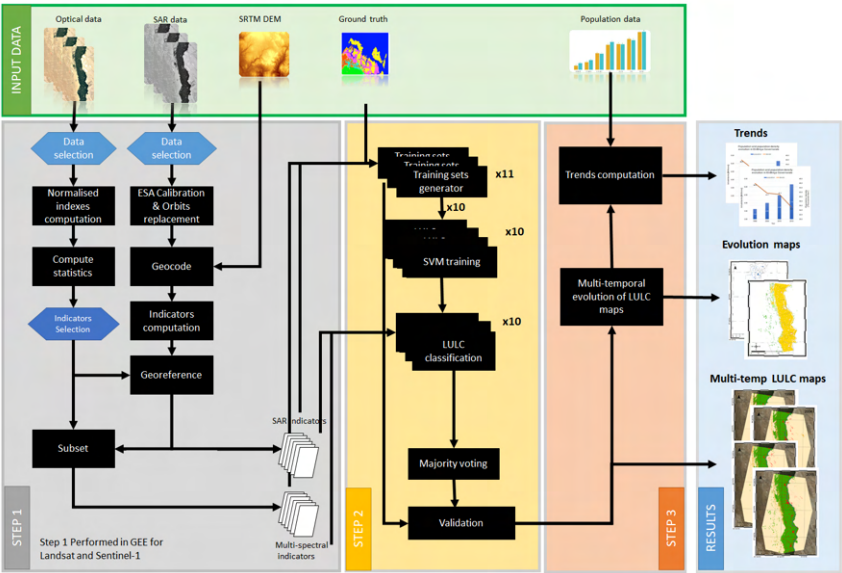


Figure 3.3: Overview of the methodological approach with the three steps discussed in the text.

3.3.1. Step 1: Data Preparation and Indicators Extraction

Step 1 was implemented within Google Earth Engine (GEE) (Gorelick, 2012) for the analysis of the Landsat (5 TM, 7 ETM+, and 8 OLI/TIRS) and Sentinel-1 IW GRD imagery, as it allows direct access and processing of the datasets to export the indicators used as input in step 2.

However, as the historical ERS SAR and Envisat ASAR are not available within GEE, these images were processed on a Virtual Machine provided by the ESA Research and Service Support through their CloudToolbox service (Delgado Blasco et al., 2016). These ERS and Envisat SAR datasets were calibrated using the ESA specifications in NEST (ARRAY, 2010) and calibrated SAR images were geocoded using the Digital Elevation Model from the Shuttle Radar Topography Mission. The resulting datasets were grouped in three periods: (i) ERS dataset acquired in a time range centered around 1998; (ii) Envisat data acquired around 2004; and (iii) Envisat data acquired in 2010 (see Table 3.1).

Finally, the images were registered with the corresponding Landsat dataset, using 20 ground control points that were manually selected and uniformly distributed over the study area and represent road intersections on the satellite images. The georeferenced SAR images were resampled using a linear polynomial, obtaining a final Root Mean Square Error (RMSE) lower than 1 pixel (30 m) for all the different cases. Optical images were finally cropped to match the SAR data extent. At the end of the data preparation, all data were unified to the same image resolution, namely 30 m posting, and georeferenced in the Universal Transverse Mercator (UTM) projection (Zone 36N) and World Geodetic System 84 (WGS84) Datum.

Satellite-Derived Indicators for Land-Cover Classification

Different sets of indicators, feeding the land-cover supervised classifier, are defined for SAR and multi-spectral data. Regarding the SAR data, we selected indicators (see Table 2) with significant temporal statistical information per pixel (Delgado Blasco et al., 2017). Different land cover classes are expected to exhibit different statistical backscatter properties. Among those, urban areas have the lowest temporal standard deviation as opposed to crop fields or water, which exhibit larger fluctuation of the signal measured over time.

Regarding the multi-spectral data, instead of using single spectral bands, often a linear combination of bands is used on normalized differences of different bands (Joshi et al., 2016; Angiuli and Trianni, 2014; Aswatha et al., 2016). Traditionally, many indexes (e.g., NDVI) have been defined as the normalized difference of two bands with the aim of highlighting specific features of the land, such as vegetation, water surfaces and built-up areas (Aswatha et al., 2016; Li and Chen, 2014; Silleos et al., 2006; Zhou et al., 2014). The advantages of this method are manifold. Firstly, data are globally consistent. Secondly, the information provided by each index gives the opportunity of analyzing the contribution of different features in mixed urban areas. Finally, the risk of ambiguities is minimised since the different indexes complement each other in distinguishing the land cover classes. This approach has been found to be effective by several studies (Aswatha et al., 2016; López-Caloca, 2015; Patel et al., 2015; Trianni et al., 2014) and has been selected as the starting point of this work.

As shown in Table 3.2, for SAR data, the following indicators were investigated: (i) temporal average calibrated SAR backscatter, Eq. (3.1), expressed in decibel scale (dB); (ii) temporal standard deviation of calibrated SAR backscatter signal per pixel in dB, Eq. (3.2); (iii) temporal coefficient of variation of calibrated SAR signal per pixel in dB, Eq. (3.3) and; (iv) coefficient of dispersion in linear scale, Eq. (3.4).

Table 3.2: Formulas of the four selected indicators of SAR derived information employed as input in the land use/land cover (LULC) classifier. Each index is calculated within the temporal data series of each pixel i and K images, with $K \in [1, N]$, being N the total number of images.

Indicator	Formula
Backscatter average [dB]	$\mu_{avg,i} = 10 \log_{10} \frac{1}{N} \sum_{k=1}^N \sigma_{k,i} \quad (3.1)$
Backscatter standard deviation [dB]	$\sigma_{std,i} [dB] = 10 \log_{10} \sqrt{\frac{1}{N-1} \sum_{k=1}^N (\sigma_{k,i} - 10^{\frac{\mu_{avg,i}}{10}})^2} \quad (3.2)$
Coefficient of variation [dB]	$\sigma_{normstd,i} [dB] = 10 \log_{10} \left(\frac{\frac{\sigma_{std,i}}{10}}{\frac{\sigma_{avg,i}}{10}} \right) \quad (3.3)$
Coefficient of dispersion	$D_i = \frac{10^{\frac{\sigma_{std,i}}{10}}}{10^{\frac{\sigma_{avg,i}}{10}}} \quad (3.4)$

As shown in Table 3.3, for multi-spectral data the following normalized ratios were computed: (i) Normalized Difference Built-up Index (NDBI, Eq. (3.5)); (ii) Normalized Difference between SWIR-1 and SWIR-2 (NDSWIR12, Eq. (3.6)); (iii) Normalized Difference Vegetation Index (NDVI, Eq. (3.7)) and; (iv) Normalized Difference Water Index (NDWI, Eq. (3.8)). Of these indicators, the 95th percentiles, respectively, were computed from the temporal distribution (N images) of each pixel (i) and selected as the final indicators. Using this 95th percentile, we avoid artifacts in the data such as the ones produced by the cloud-covered data.

Each of the inputs selected for the classifier helps to better discriminate one or more land cover classes we intend to identify. For example, from the optical indicators, the NDVI helps to discriminate vegetation cover class, providing higher values for vegetation cover and negative values for water and desert cover. The NDWI helps with the water class identification due to their positive and higher values while using NDVI and NDWI together facilitate the desert class identification. From the SAR indicators, the coefficient of variation helps to discriminate urban and desert cover as they exhibit lower values from the higher values of the vegetation and water cover. The coefficient of dispersion helps to discriminate the dunes class from the vegetation and water cover class being characterized the three classes by their higher SAR backscatter temporal variability.

Table 3.3: Formulas of the four normalized ratios derived from each of the multi-spectral datasets. Each index is calculated within the temporal data series of each pixel i and K images, with $K \in [1, N]$, being N the total number of images.

Indicator	Formula	
Normalized Difference Built-up Index	$NDBI_{i,k} = \frac{SWIR1_{i,k} - NIR_{i,k}}{SWIR1_{i,k} + NIR_{i,k}}$	(3.5)
Normalized Difference SWIR channels	$NDSWIR12_{i,k} = \frac{SWIR1_{i,k} - SWIR2_{i,k}}{SWIR1_{i,k} + SWIR2_{i,k}}$	(3.6)
Normalized Difference Vegetation Index	$NDVI_{i,k} = \frac{NIR_{i,k} - RED_{i,k}}{NIR_{i,k} + RED_{i,k}}$	(3.7)
Normalized Difference Water Index	$NDWI_{i,k} = \frac{GREEN_{i,k} - SWIR1_{i,k}}{GREEN_{i,k} + SWIR1_{i,k}}$	(3.8)

3.3.2. Step 2: Land Cover Mapping

In this work, we have chosen a pixel-based feature fusion approach, using the aforementioned pixel-based indicators as an input of the supervised classifier.

Supervised Classifiers

We made use of an open-source C++ suite of utilities for remote sensing (RS) image processing (McInerney and Kempeneers, 2015). This suite implements support vector machine (SVM) models that are machine learning supervised learning models with associated algorithms. In particular, the suite implements a supervised classification SVM model (C-SVM) based on the library libSVM and it uses a radial basis function (RBF) kernel (Vapnik, 1998; Keerthi S. S., 2003). Several steps are needed in order to perform a classification: (i) the input indicators composing the dataset to be classified were scaled in order to avoid values spanning greater numeric ranges dominate those with smaller numeric ranges (e.g., normalized between minus one and plus one); (ii) a training dataset (a shapefile of points) was prepared for each target class using Google Earth where each point corresponds to an array containing the correspondent values of the input indicators for that pixel; (iii) using the RBF kernel, the optimal parameters C (penalty parameter for the wrong classification) and g (transformation parameter in the kernel) were obtained maximising the accuracy in classifying test data. These C and g parameters were obtained using the `pkopt` function provided within the `pktools` package, which with iterations explores in the user-defined range of C and g values until finding the local minimum that minimises the errors produced by the classifier. At this stage, the classification engine was ready to process and classify unseen data.

Land Cover classes

We have defined five classes to be employed to create our classification maps. Four generic classes: (i) built-up area, hereafter named 'urban'; (ii) sandy and rocky desert combined into a 'desert' class; (iii) vegetation, crops, garden, grass, and agricultural fields named as 'field' and; (iv) 'water' class mainly formed by the Nile River and smaller water

bodies present in the scene. Finally, our fifth class named 'dunes' identifiable thanks to the data fusion approach, not only inside the desert but also inside the floodplain. This class is expected to be characterised by having high temporal variability of the radar signal, with high optical radiance values characteristic of a sandy desert. 'Dunes' and 'desert' behave differently from the SAR response of each of them.

Land Cover Classification

Land cover classification was performed by labeling land cover maps using the aforementioned five classes. We investigated the temporal continuity of land classes in subsequent LULC maps, with special focus on the transitions: (i) 'urban' → 'field'; (ii) 'field' → 'desert'; and (iii) 'dunes' → 'crop'.

The training dataset retrieved from the labeled classes using Google Earth, which was split into 11 sets, of which 10 were used to train as many classifiers, and the remaining one used as ground truth dataset for final validation. Subsequently, each classifier was applied to the datasets referring to the various years studied, thus returning 10 intermediate classifications per dataset. Unique final classification maps were obtained by feeding the intermediate results to a majority voting condition. The majority voting strategy assigns a pixel to class 'X' if it was classified as 'X' in 6 or more classification maps obtained for the same period.

Validation approaches

The proposed method is validated by evaluating the goodness of the resulting individual classification maps against the ground truth datasets by calculating the standard metrics typically employed in classification purposes, such as overall accuracy and Cohen's Kappa index (Cohen, 1960) as well as qualitatively comparing our resulting LULC maps with state-of-the-art available datasets, as explained in the following paragraphs.

Validation against ground-truth datasets The ground truth datasets were selected from the high-resolution (<3 m) historical imagery copyrighted by DigitalGlobe and available in Google Earth as of 2016. Different point sets were selected for the time periods 2004, 2010, and 2015. No data referring to 1998 was available when this work was performed. We computed the accuracy of the final classification maps using the overall accuracy and Cohen's Kappa (K) index, as performed by Congalton (Congalton, 1991) and Mather (Mather and Koch, 2004), in order to keep into account agreement occurring by chance.

Comparison with state-of-the-art datasets We employed independent state-of-the-art datasets to compare our results, namely: (i) the Global Urban Footprint (GUF) (Esch et al., 2017, 2011), processed by the German Aerospace Centre (DLR); (ii) the Prototype of Sentinel-2 Land Cover Map of Africa at 20 m (European Space Agency, 2017) released by the European Space Agency Climate Change Initiative (ESA-CCI); (iii) Global Human Settlements Layer using Landsat data for 2014 (Florczyk, Aneta; Politis, Panagiotis; Corbane, Christina; Pesaresi, 2018) (GHSL-L8), created by the Joint Research Center (JRC) and; (iv) Global Human Settlements Layer using Sentinel-1 data for 2016 (Corbane, Christina; Politis, Panagiotis; Syrris, Vasileios; Pesaresi, 2018) (GHSL-S1) with a 19 m

spatial resolution (Corbane et al., 2017), also created by the JRC. Note that the GUF, ESA-CCI and GSHL-S1 have a higher resolution than our results (30 m) and none of them totally matches the observation time of the data analyzed here.

Due to the heterogeneity of the different datasets (data sensor employed, spatial resolution, dates), in order to compare these, a harmonisation process is needed. All datasets were resampled with 30 m resolution and re-projected in the same projection system of our dataset.

Finally, we compared the urban class across the different datasets: GUF, GHSL-S1 and GHSL-L8, ESA-CCI and our classification maps for 2010 and 2015.

3

3.3.3. Step 3: Multi-Temporal Evolution Analysis

After obtaining the five-class LULC maps for the four time periods, we identified pixels that remained stable and those that underwent changes from one land-use class to another between 1998 and 2015. Non-realistic changes were also detected and labeled as miss-classified pixels, based on our "multi-temporal consistency rules", defined as follows: (1) once a pixel is urban, it will stay urban in the following periods; (2) water cannot turn into urban, field or desert; (3) fields can only become urban, and not desert or water. In our study area the water class mainly corresponds to the Nile River, and was stable during the considered time period and; (4) desert can change to urban land or crop fields, as well as to dunes. In the latter case, it implies that dunes have been migrating into rocky deserts or across desert pavement surfaces.

In the Middle Egypt region, rule 2 is a simplification as there has effectively been a change in the size of the islands in the Nile channel which may have impacted the area classified as water or agriculture. However, as this does not have an impact on the urbanised areas, being the focus of this work, we believe that this simplification is justified.

With the temporal evolution maps for the urban and field classes, together with the population data from Central Agency for Public Mobilization and Statistics of Egypt (CAPMAS) (Central Agency for Public Mobilization and Statistics (CAPMAS)., 2017), we have computed the trends of urban population density and field area per person. Since these data were not available for the entire study area, this analysis was limited to El-Minya governorate which is centrally located in the study area, as shown in Fig. 3.4.

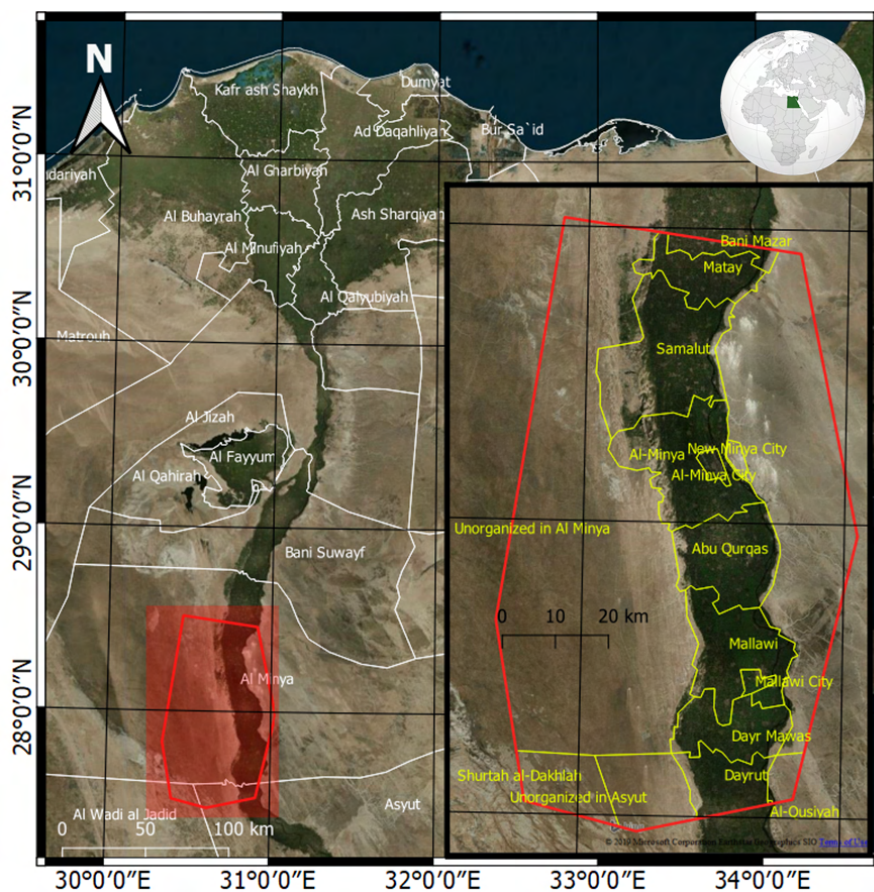


Figure 3.4: Google Earth image overlaid with the Egyptian administrative boundaries of its governorates (left), and zoom over the location of our study area with the district boundaries (right).

3.4. Result

Figure 3.5 shows the resulting land use and land cover maps for 1998 and 2015. Areas with important changes in LULC between 1998 and 2015 are indicated in Figure 3.5 as well. These areas include new urbanisation (black rectangles) both in the Eastern Deserts and within the Nile floodplain, expansion of irrigated agriculture in the Western Desert (cyan rectangles) and reclamation of dune fields in the interaction area with the expansion of agriculture (red rectangles).

3

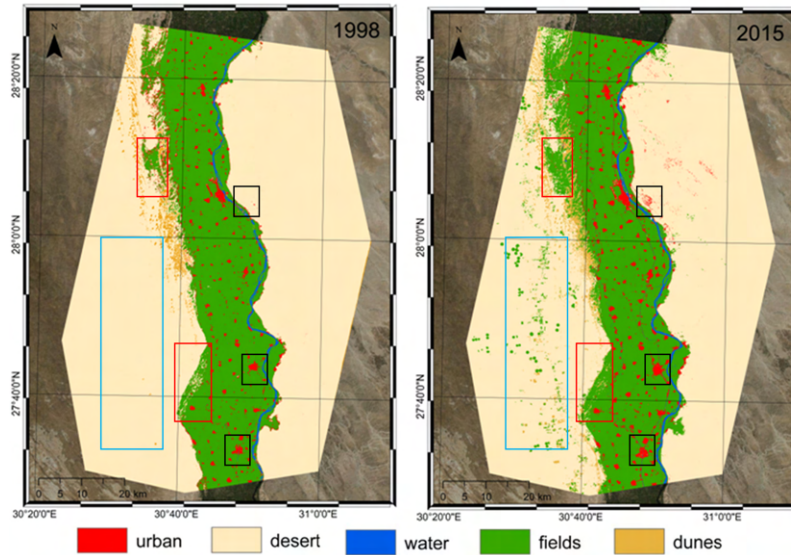


Figure 3.5: LULC maps obtained over the study area with a data fusion approach using SAR and multi-spectral data for 1998 and 2015. Black rectangles highlight areas with an urban increase, cyan rectangles correspond with fields increase in the desert area and red rectangles with crop increase within the Nile Valley and interaction area.

The accuracy of the land use and land cover maps is expressed in the confusion matrix, see Table 3.4. Overall, the agreement between the constructed LULC maps and ground truth data is very high as is illustrated by a Kappa index above 0.98 for the different time periods, which is considered an almost perfect agreement (Landis and Koch, 1977). Note that for the period of 1998, historical data in Google Earth over our study area was not available.

Tab. 3.5 clearly shows an increase in built-up areas in both the Nile Valley and the desert however, in the latter region, urbanization mainly took place between 2010 and 2015. Similarly, "land reclamation", i.e., the extension of agricultural fields in former desert environments, became more significant in the final period (2015), i.e., an 11-fold increase in its extent in comparison with the first period (2004), reaching a total new field class of almost 260 km² for the period between 2010 and 2015. Another visible trend is the constant reduction of the field class within the Nile Valley, as a consequence of the continuous urbanisation over the fertile soil of the Nile Valley. From 1998 to 2015,

Table 3.4: Confusion matrix, kappa index and overall accuracy of the resulting land use maps. Google Earth data is used as ground truth.

Year	GoogleEarth ground truth	Land use classification map					Accuracy criteria
		Urban	Desert	Water	Fields	Dunes	
2004	Urban	431	1	0	0	0	kappa index (%)
	Desert	1	6081	0	0	22	99.0%
	Water	0	0	150	0	0	Overall accuracy
	Fields	0	0	0	1936	0	99.5%
	Dunes	0	17	0	0	186	
2010	Urban	431	0	0	0	0	kappa index (%)
	Desert	1	6088	1	0	21	99.1%
	Water	0	0	151	0	0	Overall accuracy
	Fields	0	0	0	1936	0	99.6%
	Dunes	0	13	0	0	189	
2015	Urban	430	0	0	0	0	kappa index (%)
	Desert	1	6092	0	0	13	99.1%
	Water	0	0	147	0	0	Overall accuracy
	Fields	1	2	5	1936	7	99.6%
	Dunes	0	7	0	0	193	

almost 54 km² of arable land has been transformed into urbanized land cover in the Nile floodplain.

Table 3.5: Evolution in urban and field classes across the different landforms from 1998 to 2015 (km²).

Class	Landform	Year			
		1998	2004	2010	2015
Field	Valley	1705.1	1690.1	1679.7	1652.0
	Desert	0	22.1	46.5	259.7
Urban	Valley	85.5	100.5	110.9	138.6
	Desert	0	2.3	4.7	13.8

The temporal evolution of the different land use classes is extremely interlinked (field → urban, field → desert/dune, desert → dune, desert → field, desert → urban, dune → field, dune → urban), since an increase in one class is directly translated into the reduction of others. This is the case, for example, for the urban increase on the first periods analyzed (1998–2010), when most of the newly built-up area was located on the edges of the cities and villages (see Fig. 3.6), and the increase in fields was due to the "land reclamation" phenomena mainly linked to the reduction of desert classes by introducing crop fields with irrigation systems inside the arid environment (see Fig. 3.7).

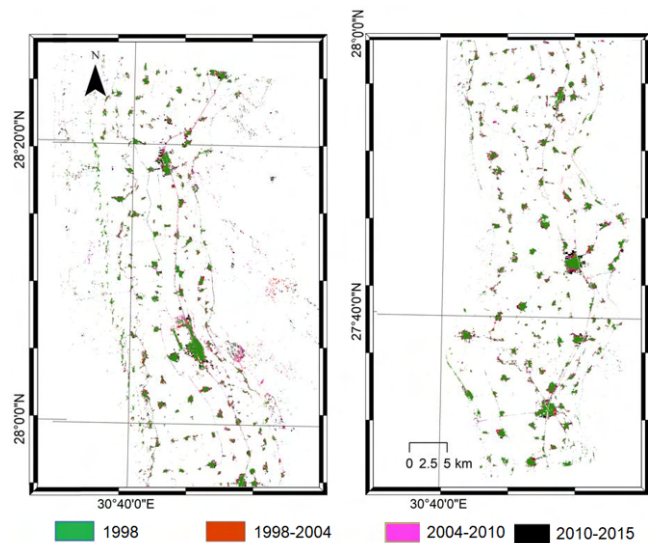


Figure 3.6: Urban expansion in the study area from 1998 to 2015. Green areas were already urban in 1998 whereas other colours show where urban expansion occurred during the corresponding time period.

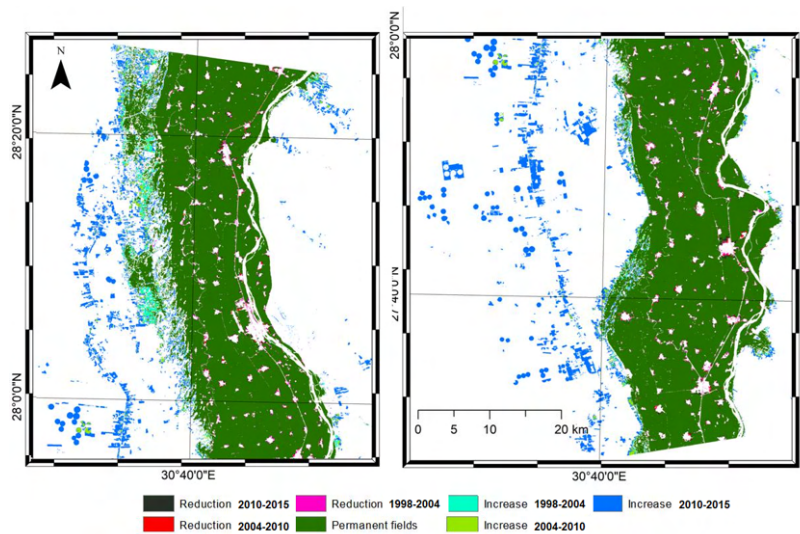


Figure 3.7: Changes in the spatial extent of agricultural fields for the El-Minya governorate from 1998 to 2015. Permanent fields in the edges indicate the limits of the Nile valley floodplain.

The urban extent and its evolution per district in the El-Minya governorate are summarised in Table 3.6. Growth rates vary between 0.01 and 0.61 km²/yr. Over the

entire period, urban areas have increased from 33 to 888% by 2015 compared to 1998. The lowest percentage increase is for El-Minya city itself, whereas a more prominent increase is observed for the new cities in the desert (New Minya and unorganized El-Minya district).

Table 3.6: Urban spatial extent (km^2) within the different analyzed districts in Middle Egypt for four time periods, and urban growth rates (% and km^2/yr) for the period 1998–2015 (total size of the study area equals 6170 km^2).

District	District Area [km^2]	Urban spatial extent [km^2]				Urban Growth Rate 1998-2015	
		1998	2004	2010	2015	[%]	[km^2/yr]
Abu Qurqas	279.54	10.54	13.33	14.81	19.07	80.93	0.47
Al-Minya	356.24	10.97	13.86	15.94	21.29	94.07	0.57
Al-Minya City	21.80	6.62	7.49	8.06	8.86	33.84	0.12
Dayr Mawas	195.85	7.32	8.96	10.06	12.81	75.00	0.31
Dayrut	221.66	11.90	13.68	14.66	18.61	56.39	0.37
Malawi	294.51	10.66	13.08	14.66	18.39	72.51	0.43
Malawi City	17.96	3.13	3.58	3.91	5.13	63.90	0.11
Matay	169.03	3.18	3.63	4.08	5.67	78.30	0.14
New Minya City	15.66	0.08	0.15	0.23	0.79	887.50	0.04
Samalut	468.49	12.29	15.19	17.24	23.34	89.91	0.61
Surtah Al Dakhlah	177.72	0.09	0.09	0.11	0.24	166.67	0.01
Unorganised Al-Minya	3697.48	2.07	3.06	4.83	11.51	456.04	0.52
Total	6170	78.85	96.09	108.9	145.74	84.83	3.72

Figure 3.8 shows the evolution in population density for the built-up environment in El-Minya governorate. These values were calculated by dividing the population census data by the urban spatial extent as shown in Table 3.6. Overall, there is a decrease from 46 thousand people/ km^2 urban area in 1998 to 35 thousand people/ km^2 urban area in 2015. Figure 3.8. also shows how with an increasing population but a decrease in the class 'fields', the average size of agricultural land available per inhabitant is decreasing from 4.7 ha/person in 1998 to 3.6 ha/person in 2015.

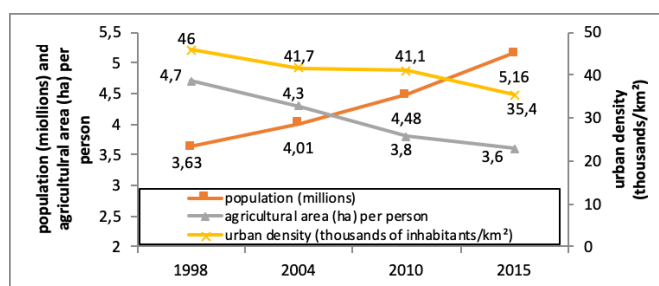


Figure 3.8: Changes in population, urban population density and agricultural land per person in El-Minya governorate in the period 1998–2015.

Finally, we compared the urban features detected using our approach with the state-of-the-art urban global datasets, such as GUF and GHSL, as well as the urban class from the ESA-CCI Land Cover Prototype over Africa. In addition, we computed the urban

extent detected on El-Minya governorate, in order to understand whether it is possible or not to use these datasets together for urban expansion analysis. Details of the urban extent measured per dataset are shown in Table 3.7.

Table 3.7: Characteristics of the different urban layers and land cover maps employed and measured urban extent across the El-Minya governorate. The temporal evolution of the urban extent shows unrealistic urban extension over time, as urban extent only increased in our study area during that period.

Year	Urban extent [km ²]	Producer	Data employed	Dataset name	Spatial resolution [m]
2010	109.01	Our	Envisat ASAR IMS/ Landsat 7 ETM+	Results	30
2012	184.35	DLR	TerraSAR-X / TanDEM-X	GUF	12
2014	207.31	JRC	Landsat 8 OLITIRS	GHSL-L8	38
2015	148.88	Our	Sentinel-1 / Landsat 8 OLITIRS	Results	30
2016	145.81	ESA	Sentinel-2	ESA-CCI	20
2016	147.45	JRC	Sentinel-1	GHSL-S1	19

We visually compared the urban extent over two smaller areas contained within our study area detected on all the datasets shown in Table 3.7, one over El-Minya City and surroundings (Figure 3.9) and the second one over Mallawi and surroundings (Figure 3.10), from where it was possible to obtain additional information regarding old urban extent and modern cemeteries from Willems et al. (Willems and Muammad, 2010). The main differences are highlighted within colour ellipses in these figures and described in the discussion section. It is important to note the non-realistic changes in the temporal evolution of detected urban extent for different datasets as seen in Table 3.7. and Figure 3.9. These inconsistencies reveal the limitations of performing a blind analysis using data obtained from different producers with their particular data sources and methods.

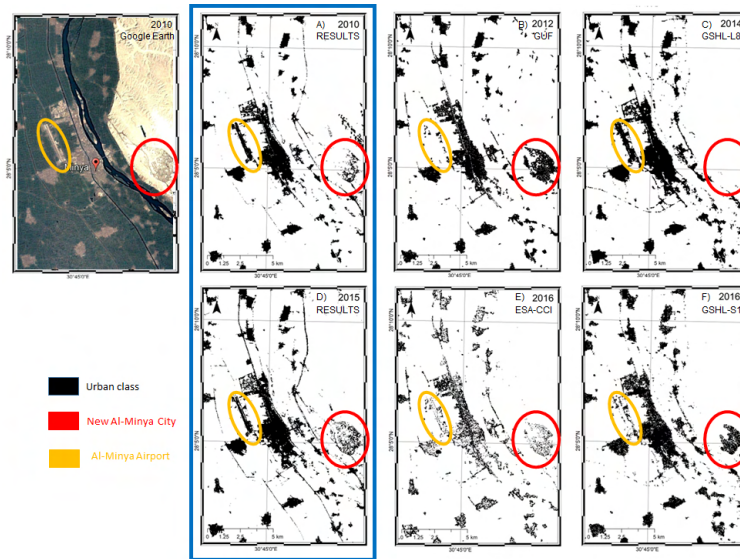


Figure 3.9: Urban/built-up area of El-Minya city and surroundings from the different datasets: (A) 2010, this study, (B) GUF for 2012, (C) GHSL-L8 2014, (D) 2015, this study, (E) ESA-CCI Prototype 2016 and (F) GHSL-S1 2016. In colour circles, different areas highlighting different classification performances. The blue rectangle highlights our results.

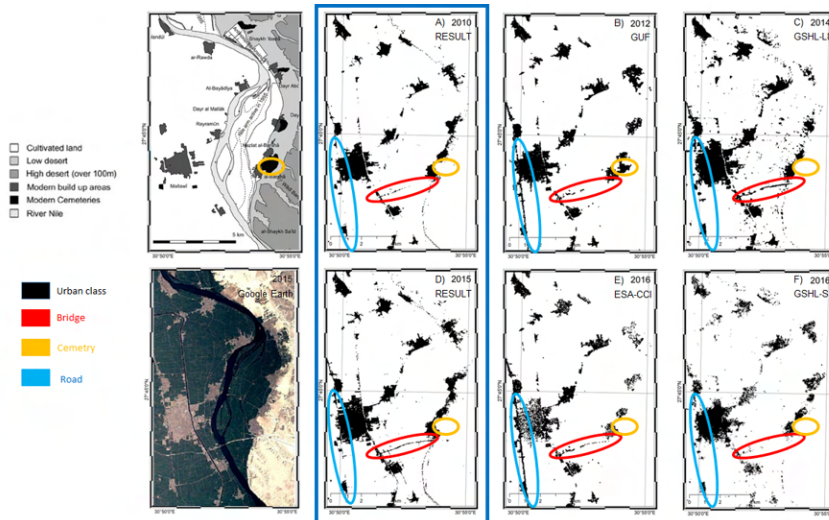


Figure 3.10: Urban/built-up of Mallawi city and surroundings from the different datasets: (A) 2010, this study, (B) GUF for 2012, (C) GHSL-L8 2014, (D) 2015, this study, (E) ESA-CCI Prototype 2016 and (F) GHSL-S1 2016. Top left map showing the location of modern cemeteries [55]. In colour circles different areas highlighting different classification performances. The blue rectangle highlights our results.

3.5. Discussion

3.5.1. Quality of the Data Fusion Approach Compared to Single Platform Approaches

Table 3.7 and Figures 3.9 and 3.10 compare the results of urban expansion obtained in this study with the data fusion approach to urban global datasets, as well as with a high-resolution visual Google Earth image. A direct and accurate comparison, however, is complicated as the timing of the imagery is different, such that discrepancies between the various urban maps are not solely related to differences in methodology but partly also to real changes in urban extent between the periods covered by each map. Nevertheless, some differences emerge from this comparison. The Global Urban Footprint dataset (Esch et al., 2017, 2011) does not detect flat urban areas, such as the Minya airport tracks (see Figure 3.9 —yellow oval), as the method employed is optimised for the detection of man-made building structures with a vertical component. Both Sentinel products (ESA-CCI and GHSL-S1) are also having difficulties in mapping the spatial extent of the airport correctly. Only the data fusion approach (this study) and the GHSL-L8 dataset correctly identifies these flat urbanised areas. On the other hand, narrower strips of urban land, such as road surfaces, are in some cases mapped by the GUF and ESA-CCL dataset but not by the data fusion approach (Figure 3.10 – blue oval). This could be related to the resolution of the imagery used to create these maps. Indeed, the GUF and ESA-CCL maps are using 12 and 20 m resolution data, respectively, whilst in this study, we used 30-m resolution data. A 30-m resolution image could be too low to identify narrow roads accurately. The newly constructed Nile bridge and access road (Figure 3.10 —red oval) is identified relatively well on most images, except the GHSL-S1 dataset. Note that road construction started in 2008–2009 and that the bridge and road were only finished in 2013–2014. Hence, the differences in mapping quality between the various datasets likely correspond to the building progress. The GHSL-L8 dataset performs very poorly when it comes to detecting the new urban expansions of New Minya (red oval in Figure 3.9). The GUF and GHSL-S1 data seem to overestimate the urban density of this new settlement and suggest a similar density as the ancient city center. However, this is not observed, i.e., the new town has more open spaces and parts are not yet developed. Here, the data fusion approach correctly predicts the expansion of the new town between 2010 and 2014 but at a lower density than the El-Minya city center itself. Furthermore, the ESA-CCI classifies many city centers as bare soil, thus showing a lower built-up density (Figure 3.9 El-Minya city and Figure 3.10 Mallawi city center). We attribute this to the fact that many buildings have similar spectral properties as bare soil: many buildings have been constructed from soil material (mud bricks) and deposition of dust on rooftops and against buildings walls in this extremely dry environment may also contribute to this effect. Finally, some large cemeteries can be found along the Eastern Desert margin (Figure 3.10 —yellow). These cemeteries are detected only in the GUF layer, due to the higher spatial resolution and characteristics of the data employed. In our specific case, it is advantageous not to map cemeteries as urban, as the urban extent is used to compute the urban population density estimates.

Overall, the detailed comparisons of the various urban datasets show that in general, the data fusion approach outperforms the quality of the global urban datasets that

are constructed from a single data platform, whether it is optical or radar data. In particular, the data fusion of radar and optical imagery is able to correctly capture the extent of urban areas s.s., i.e., buildings. Errors in the classification of roads are probably related to the lower resolution. Our results also show that comparing data on the urban extent mapped using different approaches is not an accurate method to map and quantify rates of urban expansion through time. Table 3.7 could incorrectly suggest urban expansion took place between 2010 and 2014 (from 109 to 207 km²), followed by a significant reduction in urban expansion in 2015 (again 148 km²). In the next section, we will, therefore, discuss changes in urban and agricultural land areas using a single methodology, i.e., the data fusion approach applied to 1998, 2004, 2010 and 2015 imagery.

3.5.2. Urban and Agricultural Land Dynamics

Urbanisation follows a trend that accelerated during the last period analyzed (see Table 3.6). Whereas urbanisation rates were already high in the first two periods, 2.5 and 1.8 km²/year for the periods 1998–2004 and 2004–2010, respectively, it is mainly in the period 2010–2015 that new urban land was created at a rate of 6.1 km²/year. Urban expansion is mainly linked to a reduction in arable land ("fields" class) within the floodplain (compare Figures 3.6 and 3.7). This type of urban expansion typically involves a diffusion process whereby cities and villages grow along their edges. This is illustrated in the area around the city of Mallawi in the El-Minya governorate (Figure 3.11). No less than 60% of the urban growth near Mallawi between 1998 and 2015 took place in the last five years. It involved mainly new building blocks to the north and south of the city of Mallawi. In more recent time periods, however, urbanisation is no longer restricted to the floodplain. Table 3.5 shows how between 2010 and 2015, a significant part of the urban expansion took place in the desert. This is strongly linked to government-led urban planning whereby new cities are built in desert areas, such as New Minya, located within the eastern desert (see Figure 3.9, red circle). Around Cairo, desert cities such as 6th of October City, 10th of Ramadan City and New Cairo, amongst others, have been developed since the 1970s and 1980s (Stewart, 1996). This process has also gradually impacted Middle and Upper Egypt from the 1990s and 2000s onwards, with new towns being planned near Minya, Assiut and Qena, amongst others (Ibrahim and Masoumi, 2016).

Urban expansion goes hand in hand with a reduction in land used for agricultural activities in the Nile floodplain: 53 km² of arable land has been irreversibly converted into urban land between 1998 and 2015 in the entire study area (Table 3.5). However, this does not imply that agricultural land is decreasing. In the same period, no less than 260 km² of barren desert or former dunes has been reclaimed for agricultural purposes. This includes areas in the western and eastern desert where large-scale irrigation schemes have been set up, as well as dune-levelling in the interaction area (Mohamed and Verstraeten, 2012). Figure 3.7 shows that the levelling of dunes in the interaction area already started in the late 1990s, whereas land reclamation in the desert is a more recent phenomenon. It is mainly the latter process which is responsible for the increasing rate at which new agricultural land is created. These two phenomena are

also illustrated in Figures 3.12 and 3.13 respectively.

3

The aim of the Egyptian government with the new-town policy has been to release pressure on the fertile agricultural land with a rising population and to improve the living conditions in highly populated ancient urban centers (Stewart, 1996). However, whilst our data indeed shows that urban expansion in the desert takes place at increasing rates, it is clear that urban expansion in the Nile Valley is far more important in absolute numbers. Contrary to the planned desert cities, this type of urban expansion is not planned and often informal (Hegazy, 2016). Between 1998 and 2015, approximately 1500 ha of fertile land has still been converted into urban land each year. Despite the overall increase in arable land through land reclamation in the desert, it cannot keep pace with increasing population numbers. In the El-Minya governorate, the average extent of agricultural land per inhabitant has decreased from 4.7 to 3.7 ha/person, i.e., a reduction of 21% over 17 years. Hence, we can conclude that at least for Middle Egypt, the new town policy did not halt the reduction in the availability of fertile soils for crop cultivation. Newly reclaimed areas are also more vulnerable as water has to be pumped from the Nile Valley or from groundwater resources, which is not only very costly but it may also lead to failures in water supply in the case of malfunctioning systems, thus questioning the sustainability of this type of agriculture (e.g., (Adriansen, 2009; Barnes, 2012)). On the other hand, urban population density decreased from 46,000 to 35,400 inhabitants/km² built-up area in the same period (Figure 3.8). Despite this reduction, these average urban population densities of more than 350 people per hectare remain very high to global standards (Angel et al., 2010). Furthermore, population densities in the new desert towns are often lower as more open spaces are provided and not all towns are yet successful. For New Minya, the population is currently estimated at 45,000, whilst it should reach 638,000 in 2050 (New Urban Communities Authorities, 2019). This means that population densities in the towns and villages in the Nile Valley so far remain densely populated, similar to many residential areas in Greater Cairo (Harms, 2017). Furthermore, contrary to the planned desert cities, this type of urban expansion is not planned and often informal (Hegazy, 2016). Hence, living conditions remain in general very poor.

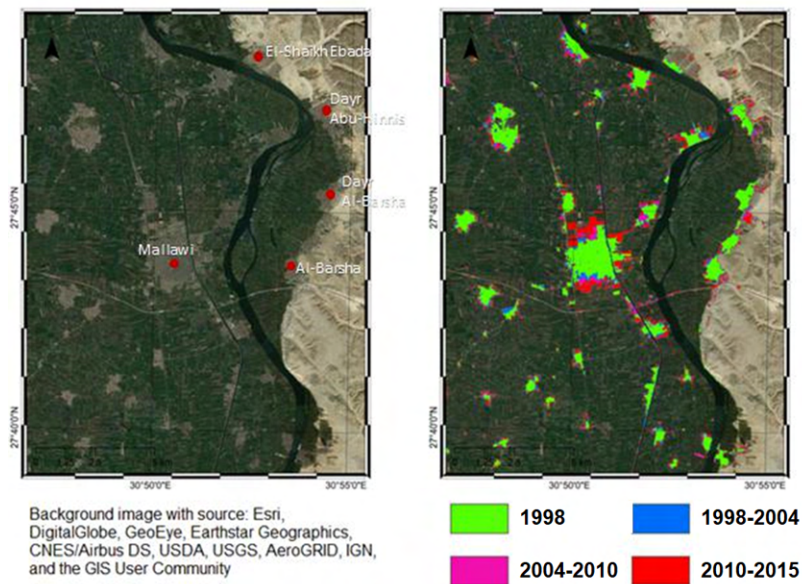


Figure 3.11: Urban classes detected for 1998, 2004, 2010 and 2015 in Mallawi province overlaid on optical image (right) and optical image over the area (left).

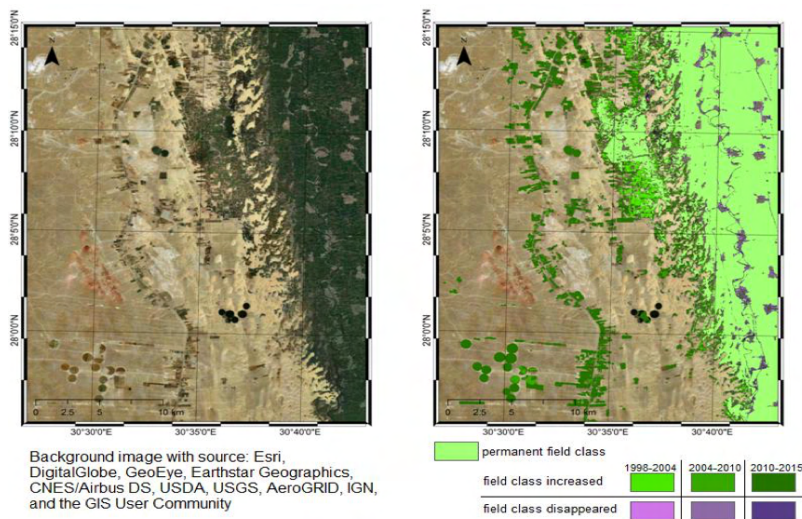


Figure 3.12: Field classes detected for 1998, 2004, 2010 and 2015 in the Eastern South-Rayan dune field area overlaid on high-resolution optical image (right) and optical image over the area (left).

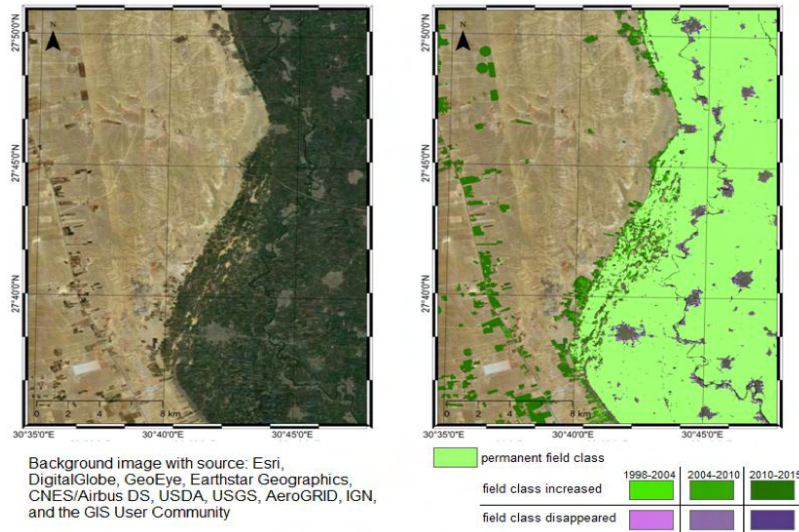


Figure 3.13: Field classes detected for 1998, 2004, 2010 and 2015 in the Western Dajla region overlaid on a high-resolution optical image (right) and optical image over the area (left).

3.6. Conclusions

In this study, we applied a data-fusion approach to map land-use dynamics in Middle Egypt for the period 1998–2015. Our data-fusion approach proved to be an effective method to discriminate urban areas where other approaches fail, especially when urban areas are built with mud bricks or constructed within desert areas. The combination of optical imagery (Landsat 5 TM, 7 ETM+ and 8 OLITIRS) with radar imagery (ERS-2 SAR, Envisat ASAR and Sentinel-1 IW) resulted in four multi-temporal land cover maps at a resolution of 30 m. Comparison with high-resolution optical images (Google Earth) showed very high accuracy, stressing the efficacy of the data-fusion approach in mapping land cover dynamics. Furthermore, comparison with globally available urban datasets shows that the data fusion approach is performing better than the single platform-based approaches when it comes to identifying new settlements in the desert or to discriminate urban buildings from bare arable land. Our study also suggests that multi-temporal studies on the land cover that combine results from various producers obtained with different methodologies could lead to erroneous nonrealistic interpretations.

Our data show a rapidly increasing trend in urbanisation in Middle Egypt (65 km²), in particular, along the margins of existing towns and villages in the Nile Valley. As a result, a continuous decrease of fertile Nile floodplain soils for agricultural practices can be seen. This loss is compensated by land reclamation processes whereby former dunes in the Nile Valley are levelled, and by irrigation practices in the desert (over 200 km²). Finally, the results show that both the urban population density and the amount of agricultural land per person have decreased by more than 20% since 1998. Finally, we

have demonstrated that the proposed data-fusion approach is a viable tool to continuously monitor future land cover changes and can be used to update the management and planning of urban areas.

4

Automatic dune dynamics analysis using multi-temporal SAR data

Sand dunes can freely move in deserts with limited sand source and a predominant wind direction. However, dunes can become a real hazard when approaching agricultural land or human settlements. Being able to analyse their position and dynamics periodically at low cost can help decision-makers to act beforehand. This chapter presents an automatic method for the monitoring of sand dune dynamics applicable everywhere.

4.1. Introduction

An understanding of dune dynamics becomes critical in cases where dunes represent a real hazard due to their proximity to villages or agricultural fields and when dunes move towards them, as is the case for (Lorenz et al., 2013a) and (Mohamed and Verstraeten, 2012; Verstraeten et al., 2014, 2017), respectively.

In order to increase our understanding of this, the accumulation of windblown sand into sand dunes has been the subject of numerous studies using both traditional field surveys and remote sensing techniques. Field surveys may include the use of measuring tape roads (Barnes, 2001; Al-Harathi, 2002), optical and electronic levelling (Käyhkö, 2007), DGPS (Santalla et al., 2009; Kostaschuk and Best, 2005; Baptista, P; Bastos, L; Bernardes, C; Cunha, T; Dias, 2008), RTK-GPS (Pardo-Pascual et al., 2005; Mitasova et al., 2005), total station (Arteaga et al., 2008), terrestrial laser scanning (Łabuz, 2016) and ground penetrating radar (Santalla et al., 2009; Buynevich et al., 2011). However, field surveys are expensive and have limited spatial coverage and revisits compared to satellite remote sensing techniques, which can cover very wide areas systematically, repetitively,

This chapter has been published in *Remote Sensing* with the title *Sand Dune Dynamics Exploiting a Fully Automatic Method Using Satellite SAR Data*, (Delgado Blasco, Chini, Verstraeten and Hanssen, 2020). To fit the publication in this study minor changes have been made.

and at a very low cost. Nowadays, satellite data is systematically acquired globally with a repetition frequency that can range from 1 to 16 days with spatial resolutions from below a meter up to tens of meters, such as PlanetScope, Sentinel-1/2 or Landsat 8 (European Space Agency., 2019). Furthermore, satellite RS has the advantage of being able to analyze less accessible dune regions and/or regions with extreme climatic conditions that may restrict field surveys. This even includes extraterrestrial dune systems, such as those on Mars (Luke and King, 2019), or on equatorial regions of Titan (Radebaugh et al., 2010; Paillou et al., 2014; Le Gall et al., 2012; Lopes et al., 2010; Radebaugh et al., 2008; Paillou et al., 2016).

4

Monitoring sand dunes on Earth is mostly performed by optical RS data, using multi-spectral datasets (Hugenholtz et al., 2012), applying multi-temporal false RGB color techniques (Mohamed and Verstraeten, 2012), manual delineation of dunes, GIS models (Ghadiry and Koch, 2010) or even more advanced techniques such as sub-pixel correlation of multi-temporal acquisitions, e.g. COSI-CORR (Hermas et al., 2004). The potential of microwave (SAR) sensors for monitoring dune dynamics has not been fully exploited, despite being able to acquire data independently from daylight, cloud coverage and weather conditions. Early works focused on deriving linear dune attributes (Qong, 1996), such as dune height using JERS-1 and ERS-1 data, studies using SAR for detecting dunes on Earth using SAR or SRTM data (Blumberg, 2006, 1998), some works based on correlation of SAR images for automatic detection of dune area (Gouinaud et al., 2013) and more recently using interferometric SAR techniques (Havivi et al., 2018; Song et al., 2020). In this work we go a step further automatizing the full dune dynamics' analysis.

As demonstrated by Blumberg (1998), dunes can be identified easily in radar images, appearing darker than their surroundings when they are located in either rougher or vegetated environments. In optical images, sand dunes are more difficult to delineate as their composition can be the same as their surroundings, see Fig. 4.1. How dark they appear within an SAR image can vary depending on the incidence angle, signal wavelength, dune type and orientation, and their being able to return a higher signal that becomes a white pixel (like a corner reflector) on the dunes' crests and edges, see Fig. 4.1). However, the predominant dune characteristic is that they appear darker than their environment. Furthermore, even when interdune areas are also characterized by sand, with the same optical properties as the dune itself, the dune can still be detected on SAR images when the SAR signal attenuation produced in the dune returns a backscatter signal much lower than its surroundings. A recent study (Nashashibi et al., 2012) modelled the radar backscatter response of sand-covered objects to radar signals, measuring the backscatter response of a surface covered with very dry sand, showing a predominant volume scatter mechanism with values lower than 15 dB for sigma0 VV channel.

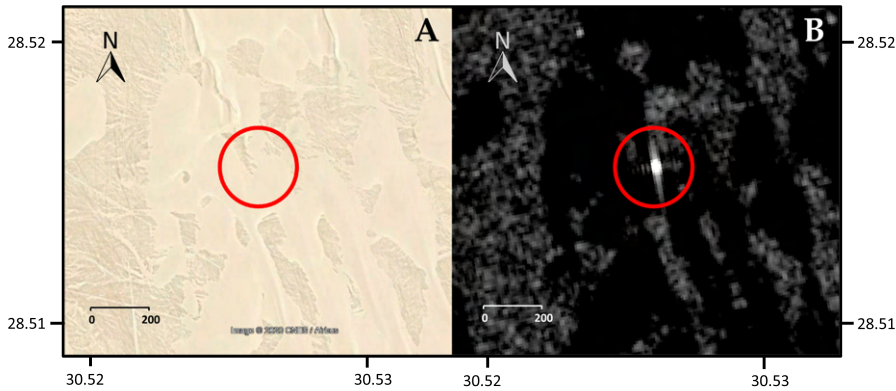


Figure 4.1: (A) Google Earth image over South Rayan dune field centered on latitude 28.51465, longitude 30.52506 in WGS84. (B) Sentinel-1 image over the same area showing a strong radar backscatter, corner reflector-alike, over a sand dune.

It is essential to highlight the importance of developing an effective and accurate sand dune monitoring system, as it is critical to monitor sand dunes that could become a threat. In the last years, migrating dunes had threatened water wells and infrastructures (Government of Western Australia, 2017; Ahmed Mutasim Abdalla Mahmoud, The Conversation, 2021), archaeological sites (Greenwatch Trust, Twitter, 2022), or buried famous film sets (Lorenz et al., 2013b). These are only some examples of situations where the proposed monitoring technique could help to prevent.

The potential and advantages of SAR imagery over in situ and optical methods is related to the geomorphology of dunes and the difficulties of monitoring their dynamics. Sand dunes may be classified by their (i) size and shape, (ii) location (coastal, desert, polar), (iii) growth stages and degree of complexity and (iv) the wind direction responsible for their formation (Lancaster, 1994). In addition, a geomorphological classification groups dunes by shape, number of slip faces and the wind directions that form them, resulting in six categories: barchan, transverse, barchanoid, longitudinal, parabolic and star (Tsoar, 2001).

In this work, we focus on the dune dynamics of barchan dunes, see Fig. 4.2, which are characterized by a crescent shape with a concave slip face and "horns" or arms extending downwind (Lancaster, 1994). Barchan dunes can form when the terrain is flat while winds blow from one dominant direction (15 degrees difference or less), vegetation cannot grow and sand is available but limited (Lancaster, 1994). If the sand supply increases, barchan dunes begin to connect with others, forming barchanoid ridges and eventually transforming into transverse dunes. Barchan dunes have the ability to migrate long distances with only a minor change in form when the above conditions are in place (Wippermann and Gross, 1986).

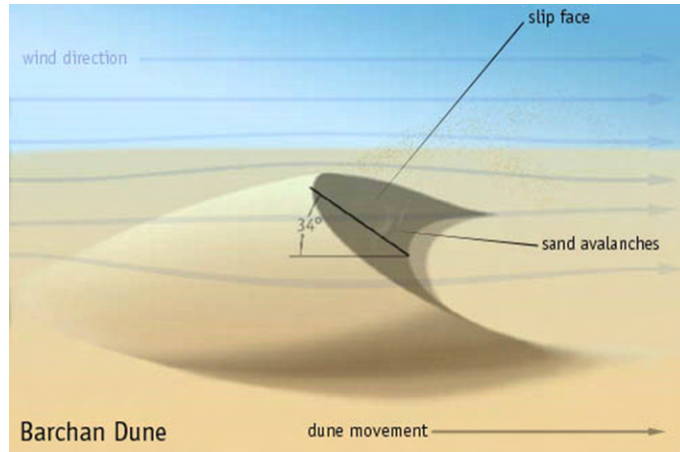


Figure 4.2: Barchan dune schematic illustrating wind, dune movement and slip face (licensed CC BY-SA 3.0).

In this study, we propose a fully automatic method to analyze the dynamics of isolated barchan dunes using SAR data. We have applied this method over two dune fields with multi-temporal C-band SAR satellites, allowing us to identify a consistent, efficient and reliable way to derive dune shapes, dunes migration rates, and directions, that is applicable globally. We focus our analysis only on this type of dune for the sake of simplicity and to test the proposed approach.

4.2. Study area

To test the proposed methodology, we have selected two sandy deserts in Western Sahara-Mauritania (WSM) and Egypt, whose locations are illustrated in Fig. 4.3. We will focus our work on the dune dynamics of isolated barchan dunes found at the two sites. These frequently propagate as a group, sometimes interacting with one another through collisions and indirect sand exchange (Livingstone et al., 2007), making more difficult the automatic analysis of them. Isolated barchans in equilibrium move without changing their shape (Wippermann and Gross, 1986) enabling the usage of the proposed automatic analysis approach.

Both sites have different topography and wind conditions. The yearly average wind in the WSM area is much higher than in Egypt, being, N-NE 4-6 and NW 1-2, corresponding to 20-50km/h and 1-10 km/h respectively (WeatherOnline, 2019). On one side, the WSM site comprises a sand dune field with barchan dunes, with an almost flat topography, having an average slope of 7 m/km in a westerly direction (USGS, 2018) and its substrate layer is a desert pavement formed by gravel and coarse sand (Ould Ahmedou et al., 2007). The South Rayan dune field (SRDF) in Egypt lays over a substrate similar to WSM desert pavement, also formed by gravel and coarse sand (Said, 2012; Mohamed, 2012b) and starts with linear dunes that develop into isolated barchan dunes, which encroach on the western part of the Nile valley. Due to the tilted topography with an average slope of 50m/km in West-East direction, the barchan dunes are not as symmetric as the ones from WSM site, but have an elongated eastern horn as illustrated in Fig. 4.3G.

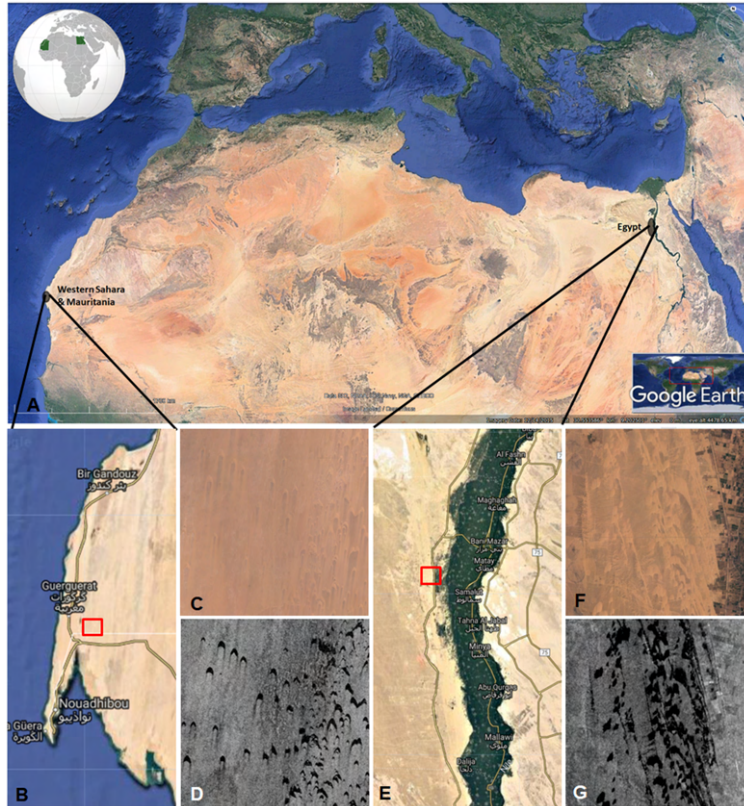


Figure 4.3: A) Overview of the location of both areas of interest: i) in Western Sahara and Mauritania desert (B) and, ii) in the South Rayan dune field in Egypt (E). Barchan dunes viewed from optical (C and F) and SAR satellites (D and G) over the respective red rectangles from B and E.

4.3. Materials and Methods

4.3.1. Materials

The selected datasets are from previous and current European SAR satellites, i.e. the European Remote Sensing satellite (ERS), the Environmental Satellite (Envisat) and the Copernicus Sentinel-1 (S-1). Due to the spatial resolutions (about 20 m for all three sensors) and the expected dune migration rate on the study area, we have selected time intervals distant enough to measure the dune movement. Detailed information on the employed dataset is provided in Table 4.1.

4.3.2. Methodology

The key element of our automatic method consists in the identification of the dunes using SAR images, assuming that in a SAR image, dunes look like dark areas surrounded by brighter pixels, see Fig. 4.4.

Table 4.1: The selected satellite remote sensing imagery.

Study area	Satellite	Acquisition date	Relative orbit / track	Orbit path	Mean incidence angle [degrees]
South Rayan (Egypt)	ERS-1/2 SAR IMS	2000/09/05	207	Descending	23
	Envisat ASAR IMS	2004/07/06 2010/08/24	207	Descending	23
	Sentinel-1 IW GRD	2014/10/14 2019/01/15	131	Ascending	33.4
West-Sahara and Mauritania	ERS-1/2 SAR IMS	1992/12/11 1999/09/20	309	Descending	22.8
	Envisat ASAR IMS	2003/07/27 2006/09/05 2009/09/17	309	Descending	22.8
	Sentinel-1 IW GRD	2015/04/07 2018/02/26	60	Ascending	33.4

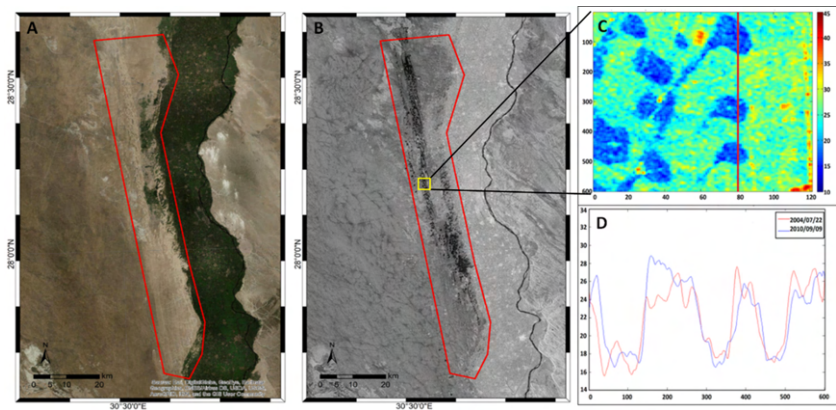


Figure 4.4: Optical (A) and SAR (B) view over the South-Rayan dune field, delimited by the red polygon. Barchan dunes are the dark areas within the red line in B). C shows the intensity of the SAR backscatter signal in decibels over the yellow rectangle in B in radar coordinates. D shows the profile of the vertical red line in figure C for two different SAR data acquired on 2004/07/07 and 2010/09/09 depicting very low intensity of signal over the barchan dunes.

The method is divided into three steps, see Fig. 4.5: i) SAR data preprocessing; ii) dune identification using the Hierarchical Split Based Approach (HSBA) algorithm (Havivi et al., 2018) and; iii) dune movement computation using Geographic Information System command line tools and validation. The validation is performed using existing data and Google Earth and validated data over the South Rayan dune made available from (Mohamed, 2012b).

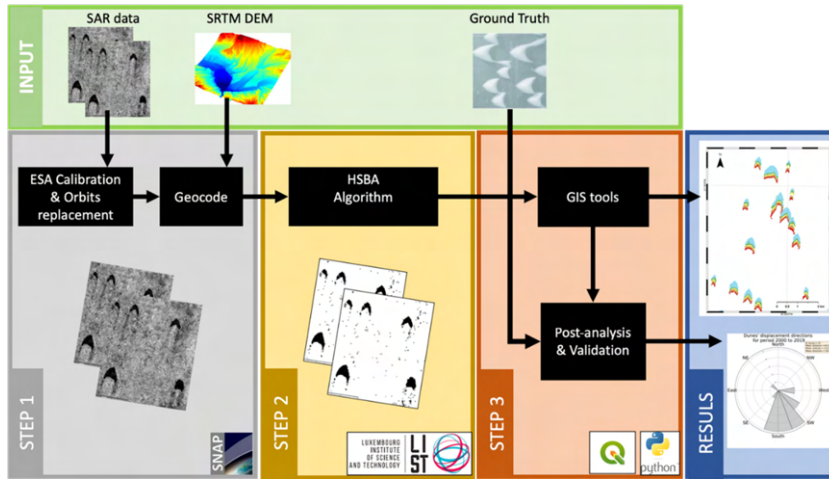


Figure 4.5: Overview of the methodological approach with the three steps discussed in the text.

SAR data preprocessing

SAR data has been calibrated and geocoded using the ESA calibration method incorporated in the Sentinel-1 Toolbox (Veci et al., 2014) integrated in the SentiNel Application Platform (SNAP), using the Precise Orbits and the SRTM DEM for accurate geocoding determination. Output SAR data has been converted to decibel scale, enhancing the contrast of the image, and making the backscattering distributions more symmetrical and Gaussian, suitable for the subsequent identification step.

Dune identification using the HSBA algorithm

This step uses as input the calibrated and geocoded SAR data in decibel scale and produces using the HSBA algorithm, a raster binary image where dunes are identified. The HSBA algorithm assumes that dune backscattering is very low, positioning its probability density function (PDF) in the lowest part of the image histogram, see Figs. 4.6B and D.

To separate the target class from the background, a thresholding approach is frequently used (Rosin, 1998). The drawback of this method is that the classification heavily relies on the adequacy of the selected threshold. To this aim, parametric thresholding algorithms are preferable because they estimate PDFs of the target class and its background, and based on them the threshold is selected (Bruzzone and Prieto, 2002). In this context, one of the main difficulties in parameterizing these functions originates from the fact that the target class often represents only a small fraction of the image. Under such circumstances, the histogram of the image values is often not obviously bimodal, and it becomes difficult to parameterize PDFs. In the case of water detection, HSBA searches for tiles of variable size allowing the parameterization of PDFs of two classes (Chini et al., 2017a). This is here applied for dunes detection, see Fig. 4.6. The approach has also been successfully applied for detecting buildings at a global scale (Chini et al., 2017a, 2018) and volcanic lava flow induced changes (Bignami et al., 2020) from SAR intensity images.

To fit the PDF of the dunes class (PDFD) we use HSBA, a statistically based algorithm which makes use of a hierarchical tiling of the image. Based on PDFD, we combine histogram thresholding and region-growing processes to identify the dunes. The parameters of the region-growing and thresholding processes are automatically derived from PDFD. The definition of PDFD starting from the entire SAR acquisition is possible if the class is sufficiently represented, i.e. identifiable, and this generally depends on the shape of the histogram. The PDFD may not be easily fit from the histogram when dunes represent only a small percentage of the entire image. Therefore, it is necessary to focus on those areas of the image that are composed of a similar number of pixels belonging to dunes and the background (PDFB) classes respectively. To this aim, HSBA has been used for automatically identifying regions in any given SAR image where the two PDFs of dunes and background are well separated and giving rise a bimodal histogram of the region. The main scope of this is to obtain a robust parameterization of the PDFD and PDFB, making more reliable the classification of the dune class. Here, the PDFD and PDFB are assumed Gaussian. This choice is motivated by the fact that the input data are multi-looked and log-transformed SAR intensity images to increase the equivalent number of looks (ENL) and to have more Gaussian distributions (Xie et al., 2002).

The proposed approach is described in detail in Chini et al. (Chini et al., 2017a). In HSBA, a hierarchical tiling of the scene is initiated starting with 40 tiles (i.e., the entire image) on the first level and then continuing by iteratively subdividing the image into 4^L sub images, with L being the hierarchical level of splitting. At $L = 1$, the image is split into quarters; with $L = 2$, the image is subdivided into sixteenths; and so on. Depending on L , the tiles will thus be characterized by different sizes. At each level, descending from the upper level to the lower one, only tiles fulfilling fixed criteria are selected, while the others will be further split.

The criteria to select a tile are: 1) The histogram of the tile has to be bimodal and composed of two Gaussian PDFs (Fig. 4.6D); 2) The number of pixels belonging to dunes class must be composed at least of 20% of the considered tile; 3) The mode of PDFD has to be lower than a predefined value, which is set to -17 dB, because the backscattering of dune class is expected to be low.

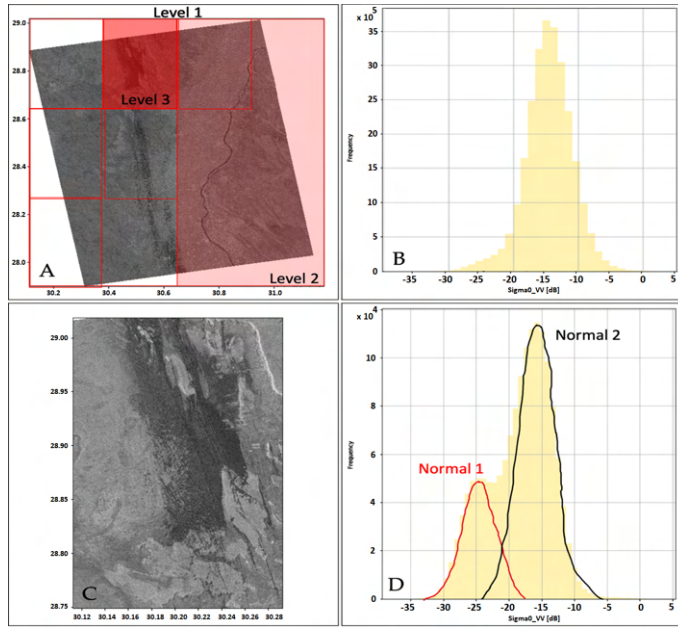


Figure 4.6: A) Sentinel-1 image acquired over Egypt including the South-Rayan dune field showing three levels of tiles similar to the employed in the HSBA. B) Level 1 (full scene) backscatter histogram. C) Sentinel-1 image zoomed over the Level 3 tile colored in red in A), and D) its corresponding histogram, highlighting the separability of the normal distributions of the dune backscatter (red Gaussian) in the lower part and the other Gaussian in black for the non-dune areas.

To fit PDFD and PDFB from the histogram of a given tile, we use the Levenberg – Marquardt algorithm, a technique to solve nonlinear least square problems (Marquardt, 1963). To check the bimodality of the histogram we use the Ashman D coefficient (Ashman et al., 1994), which quantifies how well two Gaussian distributions are separated, e.g., PDFD and PDFB, by considering the distance between their main modes and their dispersions, i.e., standard deviations. To consider the PDFs as well-separated, the Ashman D coefficient has to be higher than 2.

All tiles selected based on the three previously defined criteria are merged together and the resulting histogram is used to fit the final PDFD and PDFB to be used in the next steps for thresholding the image. Although the resulting PDFs are well-separated, some overlap is still present, consequently setting the threshold where PDFD is equal PDFB can produce some over- and under-detection. To reduce these latter drawbacks, contextual information is also used via a region-growing approach (Chini et al., 2017b; Giustarini et al., 2012). The region-growing algorithm starts from seed pixels and adds to them connected pixels that lie within a predefined tolerance value. The choice of the threshold values for the seeds and for stopping the growth is a crucial point. The strategy we follow to select these two parameters is based on PDFD. We select seed pixels with a high likelihood to belong to the dunes class, e.g., pixels with backscattering values lower than the PDFD mode, while many different thresholds to stop the growth are tested, and we select the one that minimizes the RMSE between the theoretical PDFD and the empirical histogram resulting from the region-growing.

Dune movement using GIS functions

This last step uses as input a pair of binary images obtained after the dune identification step and it computes the movement of individual dunes based in centroid differences of the intersecting dunes, see Fig. 4.7 as done in (Mohamed and Verstraeten, 2010). The algorithm assumes that a dune shift is less of its width in the moving direction, thus an adequate SAR time sampling is necessary. This latter will be guaranteed by new satellites constellations which are able to image systematically the surface with a very small repeat cycle, e.g. the six days of Sentinel-1.

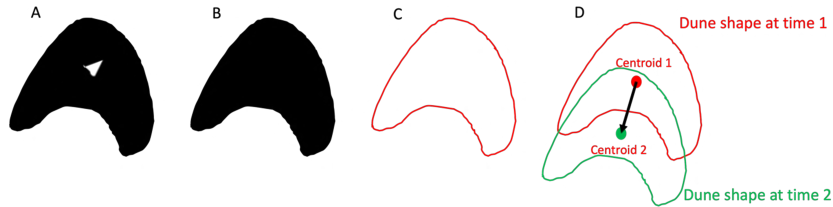


Figure 4.7: Schematics of: A) Detected dune, B) Filled dune, C) Polygonized dune and, D) dune movement computation based on centroid difference, resulting in the black arrow symbolising the displacement vector.

The functions employed in this step are: i) hole-filling of the binary images; ii) polygonize them; iii) compute x and y centroid coordinates for the different polygons; iv) intersection of the polygons in two dates and; v) movement and direction estimation. Directions of dunes movement range, clockwise, from 0 to 360 degrees, where 0 degree corresponds to north direction. The QGIS processing modeler (Graser, 2013) has been employed for defining and creating the automatic processing employed in this step, see Fig. 4.8.

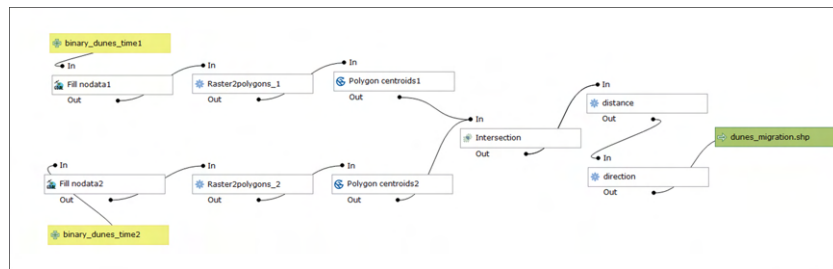


Figure 4.8: Processing diagram defined using the QGIS processing modeller.

The obtained results are finally filtered based on an area consistency criterion that we have defined in line with the area consistency principle of the isolated barchan, which move conserving their shape and hence also their area. This area consistency criterion can be translated as the dune area loss between the observed dates, as illustrated in Eq. (4.1). Based on that criterion, variations on the area measured using our method

can take values ranging in the interval $[0, 1]$ and it can help us to discriminate individual dunes from other cases such as dune merging, dune splitting, (see Fig. 4.9) which could produce high variability of the observed dune area. The area consistency criterion measures the area loss, given by

$$arealoss = \frac{abs(area_{t1} - area_{t2})}{max(area_{t1}, area_{t2})} \quad (4.1)$$

where *area* is the dune area for each time observed $t1$ and $t2$ and measures the area loss between two observations respect to the maximum area observed.

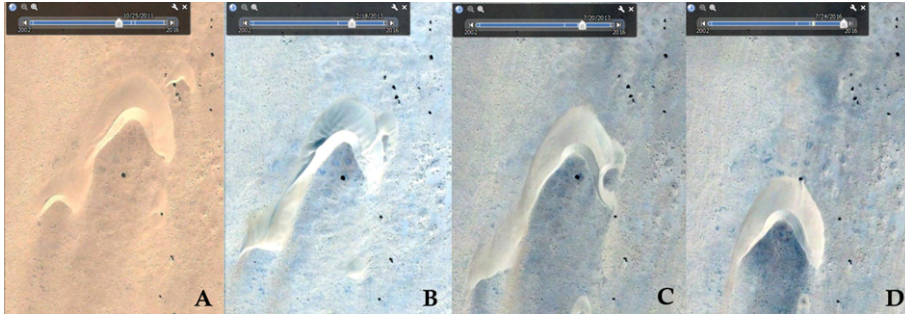


Figure 4.9: Example of the merging and splitting phenomena that can occur in dune fields when smaller dunes reach larger dunes. Barchan dunes are characterized for conserving shape while moving, as illustrated in the images available in Google Earth over the WSM site. Images sorted in acquisition time from left to right. A) acquired in 25/10/2011; B) in 18/02/2013; C) in 20/07/2013 and D) in 24/07/2016.

Validation

We have manually delineated dunes from both WSM and SRDF areas on two different time periods using very high resolution optical data available in Google Earth, enabling the comparison of the results obtained from our automatic approach versus the manually delineation and analysis, in terms of dunes locations, and movement characteristics such as distance, average velocity, direction and area loss for both delineated and satellite-derived data.

In addition, and for the specific case of the South-Rayan dune field, we have also used the existing dataset obtained from (Mohamed and Verstraeten, 2012).

4.4. Results

4.4.1. West Sahara - Mauritania

In order to obtain ground truth data over the WSM site, we have manually delineated 6 dunes over VHR optical data on 2 dates, one in 2003, matching one of our datasets, and in 2013, as it was the last data available in Google Earth over that area, see Fig. 4.10. By doing so, it was possible to obtain a value that could be used in our study as threshold for the area loss computation, see Eq. (4.1). Moreover, we are able to compute their long-term movement characteristics. Furthermore, Fig. 4.10G shows a small area of the WSM site where are located the six dunes employed as ground-truth, showing the crescent shape of the barchan dunes, being symmetric for most of the cases. Their

computed distance, velocity, area loss and direction, are found in Table 4.2 confirming the area consistency principle of isolated barchan dunes (with area loss <0.2), and also confirms the average direction obtained using the automatic method (direction SSE, from 180 to 190 degrees).

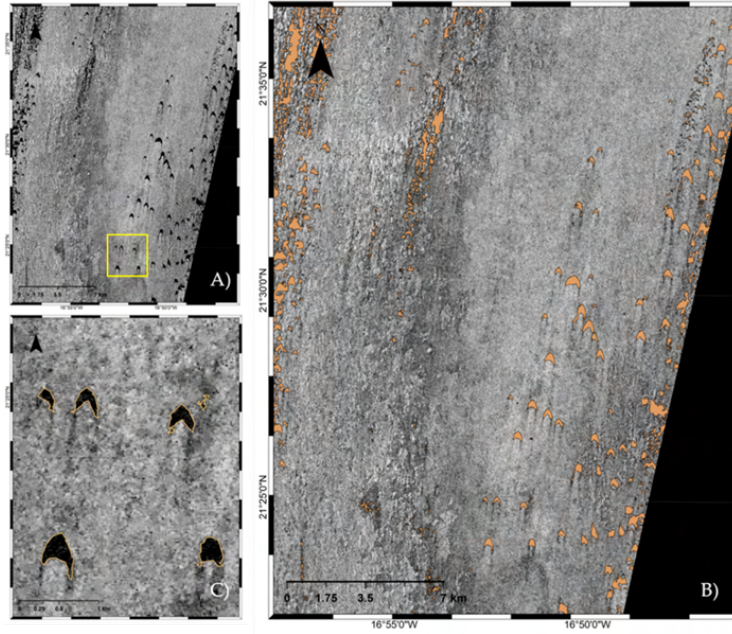


Figure 4.10: West Sahara dunes detected for 2003. A) Subset of the SAR image covering the dune field. B) SAR image overlaid with the detected sand bodies in orange. C) Zoom showing SAR image in the yellow rectangle in Figure A) as background overlaid with the contour of the dunes in orange.

Table 4.2: Dune migration information of the delineated dunes, obtained between 2003 and 2013, specifying distance, velocity, heading direction, mean area and area loss.

Id. dune	Distance [m]	Velocity [m/yr]	Heading [degrees]	Mean area (t1,t2) [ha]	Area loss (%)
A	142	13	190	22.90	5
B	305	28	190	2.42	5
C	213	19	190	5.27	14
D	152	14	189	16.35	3
E	152	14	189	14.53	9
F	162	15	189	11.58	0

We have applied the aforementioned methodology to the West Sahara dataset, detecting a total amount of sand bodies (not only isolated dunes) which varies from one image to another (Table 4.3). Biggest differences among the detected sand bodies correspond to images acquired with different sensor, and not having the exact same geographic coverage. Higher number correspond to images acquired with same sen-

sor, i.e.: ERS2-ERS2, Envisat-Envisat, S1-S1 (Table 4.3). One example of sand bodies identification obtained using Envisat data acquired on 2003 is shown in Fig. 4.11.

Table 4.3: Detected sand bodies, and average distance, velocity and heading of the isolated barchan dunes obtained applying the dune area consistency criterion, obtained over the West Sahara-Mauritania dune field.

Period	Sensors	Detected sand bodies	Isolated barchans	Distance [m]	Velocity [m/yr]	Heading [degrees]
1992-1999	ERS-2 / ERS-2	2032	181	119	15	183
1999-2003	ERS-2 / Envisat	2724	116	132	26	219
2003-2006	Envisat / Envisat	7148	369	74	19	192
2006-2009	Envisat / Envisat	4911	211	76	19	181
2009-2015	Envisat / S1	4696	289	112	16	189
2015-2018	S1 / S1	5052	400	79	20	180

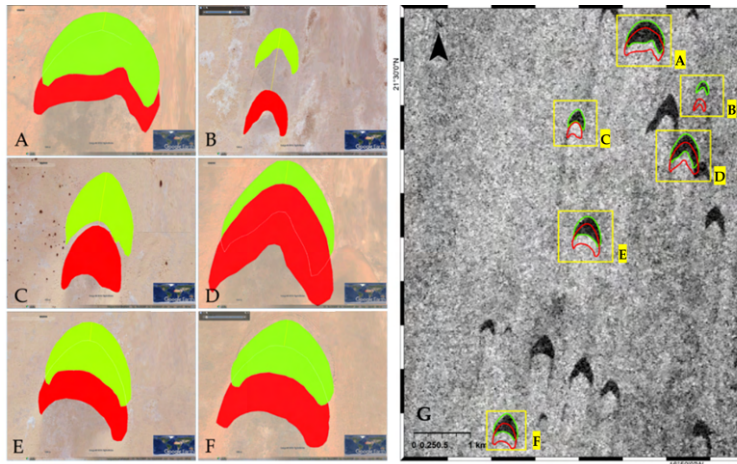


Figure 4.11: Figure showing the delineated dunes in green for 2003 and red for 2013 in A, B, C, D, E, F and in G (right) the Envisat SAR image for 2003 as background, overlaid with the outline polygons of the manually delineated dunes within yellow rectangles.

We have applied the area consistency criterion to using Eq. (4.1), ensuring that dunes measurement reported are obtained over isolated barchan dunes, which characteristic is the shape invariant in ideal situation, which results are reported in Table 3. We have obtained average dune velocities ranging from 15-26 m/yr over the analyzed area. Note that the resulted number of isolated dunes with overlap between dates is much lower than the total amount of detected sand bodies. Fig. 4.12 illustrates the histogram of the heading direction of movement of these isolated barchans in WSM.

Looking at the values reported in Table 4.3 and Fig. 4.12, seems that it could be an error on the average heading obtained, which could also interfere in the calculated velocity. We will analyze this in the discussion section.



Figure 4.12: Dune displacement directions for the different periods analyzed, indicating the number of dunes and the mean values of migration distance, migration rate and direction or heading. A), C), E), F) show dunes displacement direction in SSW direction for the periods 1992-1999, 2003-2006, 2006-2009, 2009-2015 and 2015-2018 respectively. B) shows a dunes displacement direction in WSW for the intersensor period 1999-2003 and, D) shows a main displacement direction ranging from SSW-SSE for the period 2006-2009.

The values obtained using the proposed method for the delineated dunes are shown in Table 4.4. There is a very good agreement between the velocities obtained with the automatic method and the ground truth, as well as the heading (max difference of 7

degrees) and distance. Despite these agreements, there are differences in the mean area detected, being more important for the smallest dunes (B and C) detecting near 36% less against the 12-20% for the others. These differences in detected area are linked to: i) the spatial resolution of the sensor (20 m x 20 m) and; ii) the non-detected areas are located in the borders of the dunes, as a certain volume of sand accumulated is needed in order to appear dark in the SAR data.

Table 4.4: Dune migration information obtained using the automatic method over the delineated dunes, obtained between 2003 and 2015, specifying distance, velocity, heading direction, mean area and area loss.

Id. dune	Distance [m]	Velocity [m/yr]	Heading [degrees]	Mean area (t1,t2) [ha]	Area loss (%)
A	170	13	183	22.29	6
B	178	25	197	1.56	8
C	264	20	190	3.36	12
D	147	11	190	14.44	14
E	193	15	189	11.87	18
F	193	15	190	9.27	11

4.4.2. South-Rayán Dune Field in Egypt

We also applied our methodology to the SRDF dataset. A general overview of the results obtained in the dune detection step is illustrated in Fig. 4.13C, and Fig. 4.13A shows the Google Earth overview of the SRDF (within the red polygon). Fig. 4.13B illustrates how dunes can be easily identified using SAR data, compared to optical data (Fig. 4.13A), as they appear darker than their surroundings, as explained in the introduction section.

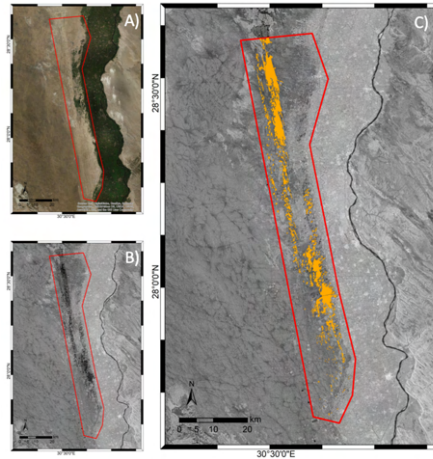


Figure 4.13: South-Rayán Dune field view in optical (A), Envisat ASAR (B) and Envisat ASAR overlaid with the detected sand bodies (C).

Furthermore, we delineated three dunes using Google Earth, selecting the ones which were specially monitored and validated with GPS and VHR optical data in (Mohamed,

2012b). These three manually delineated dunes in the South Rayan dune field are illustrated in Fig. 4.14 and their values obtained are shown in Table 4.5. Table 4.6 reports the information over the same three dunes observed in (Mohamed, 2012b).

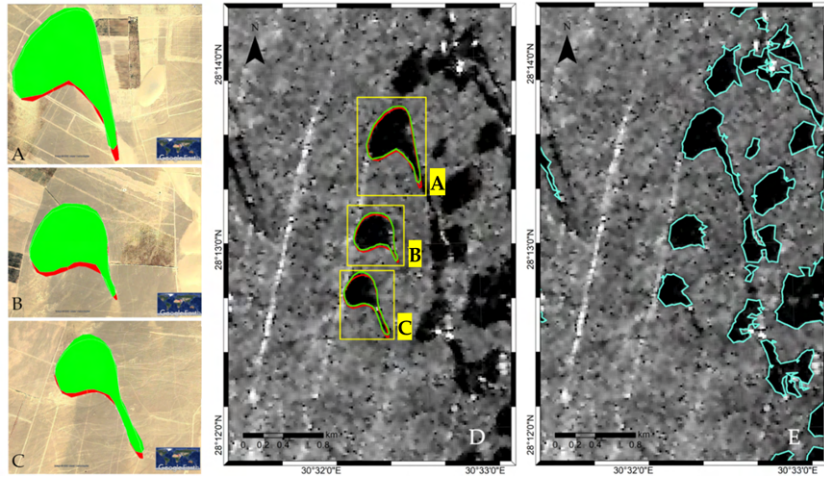


Figure 4.14: A-C shows the delineated dunes in green for 2007 and red for 2010. D (middle) the Envisat SAR image for 2010 as background, overlaid with the outline polygons of the manually delineated dunes within yellow rectangles. E (right) shows the Envisat SAR image for 2010 as background, overlaid with the outline polygons of the detected dunes using the automatic approach.

Table 4.5: Dunes' information extracted from the manually delineated dunes on Google Earth in 2007 and 2010.

Id. dune	Distance [m]	Velocity [m/yr]	Heading [degrees]	Mean area (t1,t2) [ha]	Area loss (%)
A	10	3	163	19.81	3
B	20	5	174	11.90	0
C	20	5	186	10.12	3

Table 4.6: Information extracted from (Mohamed, 2012b) over the three selected dunes from 1984 and 2003 using Landsat 5 TM.

Id. dune	Distance [m]	Velocity [m/yr]	Heading [degrees]	Mean area (t1,t2) [ha]	Area loss (%)
A	83	4	174	20.35	4
B	87	5	178	11.29	1
C	99	5	166	10.48	0

Applying our automatic method, we have detected a total amount of sand bodies reported in Table 4.7. Again, the biggest differences among the detected sand bodies with overlap corresponded to images acquired with different sensors, and not always to the same exact geographical extent.

Table 4.7: Average filtered results based on dune area consistency criteria, measured over the South-Rayan dune field.

Period	Sensors	Detected sand bodies	Isolated barchans	Distance [m]	Velocity [m/yr]	Heading [degrees]
2000-2004	ERS-2 / Envisat	1928	43	66	13	208
2004-2010	Envisat / Envisat	2729	434	45	6	158
2010-2014	Envisat / S1	2785	93	36	7	177
2014-2019	S1 / S1	1714	112	176	29	169
2000-2010	ERS-2 / Envisat	1866	64	89	8	201
2000-2019	ERS-2 / S1	581	73	188	9	184

According to (Mohamed, 2012b), the average velocity of the dune movement for the SRDF is expected to be around 2–6 m/yr. Similar values were found for some of the analyzed periods reported in Table 4.7. These values can be affected by the merging or splitting of several dunes (Horvat, 2006). This was observed when smaller dunes moving faster reached larger dunes moving at a slower pace (Horvat, 2006). Furthermore, dunes in the SRDF could have been affected by new fields that had appeared in the proximities of the dune field, even surrounding dunes, in the Western Desert.

In Table 4.6, information extracted from (Mohamed, 2012b) over the dunes A, B and C are reported and it is possible to appreciate that both velocity and area are in agreement with the dunes extracted from Google Earth.

Fig. 4.14 shows the manually delineated dunes using Google Earth from 2007 and 2010, in green and red respectively. In the middle image (D) we show the delineated dunes over the Envisat ASAR data acquired on 2010/08/24, highlighting the good agreement between the outline polygons of dunes in left (A, B and C) and the black dunes in the SAR image. In the right Fig. 4.14E, the Envisat image is overlapped with the outline of the dunes detected using our automatic method. We can observe some differences in the detected shapes in D and E, that will be discussed in Section 4.5.

From Fig. 4.14E we can see that detected dunes do not exactly match the delineated ones, as some dunes do not appear totally black in the SAR images as they have white pixels due to high backscatter produced over the sharp edged created with the help of the topography (average slope of 50m/km). These bright spots on the dunes were not encountered in the uniform and regular barchan shapes on the WSM dune field, see Fig. 4.10.

In Table 4.7, there are reported the average values for distance, velocity and direction obtained for isolated dunes after applying the area consistency criterion. For the periods from 2000 to 2004 and from 2014 to 2019, values are higher than in the other observed periods. In the South-Rayan dune field, dunes move slower, and for some cases, the observed movement is near the sensitivity of the technique. A good area detection become critical when the expected movement is only 1 or 2 pixels (with 20m pixel spacing). In this case, the topography influences the dune morphology creating sharp edges on dunes. These sharp edges appear as white pixels in the SAR image, not being detected as dune, and hence, affecting the dune area measured and finally its movement. However, long-term migration is well detected, both in speed and direction.

In Table 4.7, we have analyzed the dune migration within consecutive observations,

and also the observations with more time difference for both sensor change: i.e. ERS2-Envisat (2000-2010) and ERS2-S1 (2000-2019). It is also important to highlight that different sensor data had not the same extent, for which the maximum overlap is obtained within the same sensor: i.e. Envisat-Envisat (2004-2010) and S1-S1 (2014-2019) where we have detected higher number of individual dunes.

For the dunes remaining after applying the area consistency criterion, in order to validate further our results we have compared our dunes map with the data from (Mohamed, 2012b), obtaining 30 overlapping dunes. From these 30 dunes, we have analyzed the variation in their area detection for the different dates, obtaining the results illustrated in Fig. 4.15. From this figure, we can identify 8 dunes for which there are area differences at least in 2000 and 2019 with respect to the other observed years. This means that on 22 of the 30 total intersected dunes, our method is in total agreement with the results from (Mohamed, 2012b) regarding the dunes areas, while in 8 dunes, something could have happened for those specific time periods.

4

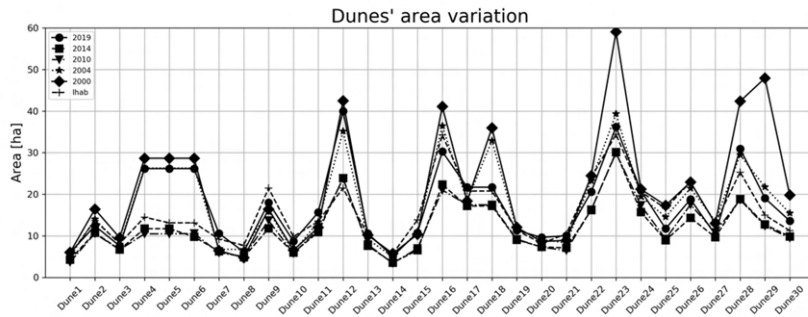


Figure 4.15: Dune's area variation for the different years of the 30 dunes in common with (Mohamed, 2012b).

Finally, our method provided dune migration information also for the dunes A, B and C which values are reported in Table 4.8. These values are not totally in agreement with the ones found in literature, probably due to the detected dune area, being a 85%, 80% and 65% the area detected in the SAR images for the dunes A, B and C respectively. This underestimation of the dune area directly affects their centroid coordinates and hence the distance and velocity. Despite of this, the obtained values are still in the range of the expected dune migration and close to the ground-truth values.

Table 4.8: Dune information provided by the automatic method on SAR data acquired in 2004 and 2010 for the same dunes which were also manually delineated, located in the South Rayan dune field.

Id. dune	Distance [m]	Velocity [m/yr]	Heading [degrees]	Mean area (t1,t2) [ha]	Area loss (%)
A	38	5	141	17.31	2
B	23	3	149	9.12	2
C	21	3	163	6.80	8

4.5. Discussion

The total number of the detected sand bodies reported in Table 4.3 and Table 4.7 showed high variability among different periods. One of the possible causes of this high variability could be explained by the differences in area detected which are minimized after applying the proposed criterion.

An intrinsic characteristic of free dunes belonging to the same dune field is that the distance that rove the dunes have an inverse relationship with their size, i.e. small dunes move longer and faster than bigger ones, with the characteristic of keeping their shape invariant in case of barchans in equilibrium (Wippermann and Gross, 1986). Dunes can fuse when smaller and faster dunes reach bigger and slower ones, and this fusion can be temporary or permanent (Horvat, 2006).

Fig. 4.16 illustrates the curve fitting of the aforementioned characteristic (the distance that the dunes rove has an inverse relationship with their size) of our manually delineated dunes on the WSM site (in blue) and the dunes from SRDF delineated in Mohamed (2012b) (in orange), and clearly shows the differences in area and migration rate of the dunes of both analyzed sites.

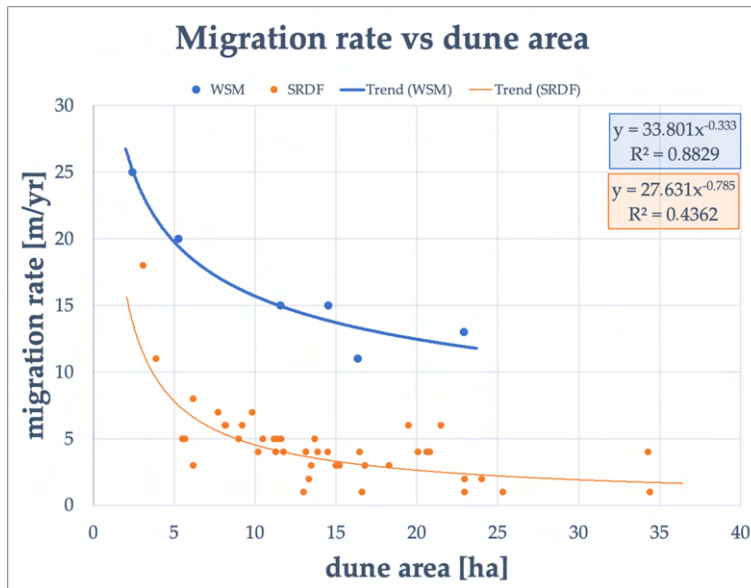


Figure 4.16: Curve dune area versus migration rate for the WSM and SRDF sites, including trend lines.

Small dunes rove faster than larger dunes, as illustrated in Fig. 4.16. This may produce their non-intersection between two time periods, which excluded them from our analysis due to the non-intersection condition. In order to provide dune migration information, our method needs each dune shape to intersect in space for the analyzed time periods. Nowadays, and due to the revisit times of the new satellite constellations such as Sentinel-1, we could also analyze faster dunes, just by decreasing the time interval between images. Barchan dunes located in the almost flat WSM area have a more regular shape, helping the proper detection of the dune area. And, the average

velocity measured on the intersected dunes is over 18 m/yr, and almost as fast as the barchan dunes in Chad, considered some of the fastest dunes on Earth, moving at an average velocity of about 20 m/yr (Vermeesch and Drake, 2008). Moreover, we measured an average ratio of the dune migration rates (automatically computed versus ground truth) of 0.96, being very consistent with the estimated migration rates. Moreover, we also computed the differences in the dune area measured, which varied from 11% to 36% of area difference compared to the ground truth, being more critical for smaller dunes. This is directly linked to the spatial resolution of the data employed. However, this misdetection of the dune area seems systematic and is located on the dune edges, where thinner sand layers are located, allowing us to compute reliable migration rates despite the dune area difference.

We also computed the dune migration information for the different periods analyzed for the intersecting dunes in the SRDF dune field, obtaining an average movement of 4–5 m/yr in the SSE direction in agreement with (Mohamed, 2012b), which reported an average migration rate of 4.4 m/yr also in the SSE direction. We also observed that the dune area on the SRDF site is slightly underestimated, probably due to the bright pixels that appear, preventing better detection, see Fig. 4.2. However, long-term migration information is properly detected.

We have also noticed a miss-alignment of the ERS-2 SAR data with respect to the Envisat ASAR and Sentinel-1 dataset. This is visible when computing the dune's displacement direction for the period 1999 to 2003 in Fig. 4.12B and Fig. 4.17C. This shift found could not be avoided and could be attributed to the precision of the orbital information available and employed during the pre-processing of the ERS-2 data. We can observe this shift when comparing multi-sensor data but does not appear when considering the analysis of the results obtained from each sensor independently. Moreover, this has been only found for the historical ERS-2 data, and not for the other datasets employed.

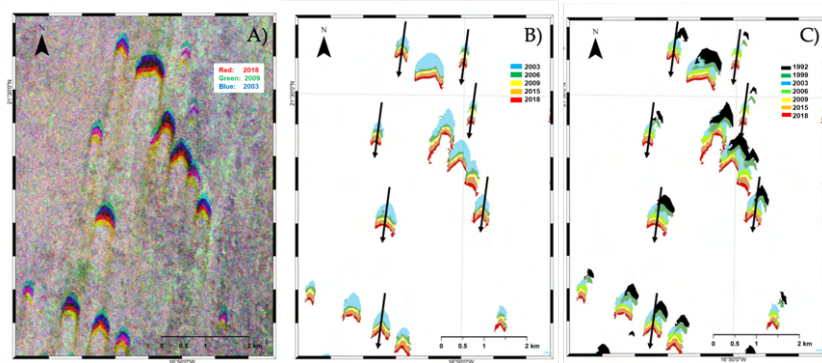


Figure 4.17: A) False RGB composition of SAR images acquired on 2018 (Red), 2009 (Green) and 2003 (Blue). B) Polygons of the dunes detected for Envisat and Sentinel-1 data with movement direction indicated with black arrows. C) Polygons of the dunes detected for all period, including ERS-2 SAR, which appear misaligned for the periods 1992 and 1999 (black and dark green polygons respectively).

Hence, despite the fact that dunes may appear slightly smaller in SAR images compared to optical images, we have demonstrated that SAR data can be used to analyze dune

dynamics at the dune field scale, as shown in the consistency of the dune migration rates between our results and the ground-truth data.

4.5.1. Overall comments from the proper exploitation of the proposed approach

For all the sandy areas detected, we discarded larger volumes of sand corresponding to dune groups in our analysis, analyzing only individual dunes for which the detected area has varied less than 20%. By doing this, additional dunes are discarded, for example, when such dunes join and separate from other dunes through the analyzed period.

Considerations identified for a proper usage of our approach can be grouped into two categories: (i) dune detection; and (ii) dune migration analysis. For the former, obtaining an accurate detection is linked directly to the spatial resolution of the employed sensor and to bright pixels that sometimes appear on dunes, while for the latter, dune migration information can only be provided for isolated dunes that have spatial overlap on the analyzed images.

To maximize the number of dunes with overlap, it is suggested that the number of images to be processed is increased, thus reducing the time interval between two consecutive ones, in order to ensure a geographical overlap of the moving dunes. This can be foreseen by knowing the wind speed of the area of interest and by selecting the proper dataset with spatial-temporal resolution to ensure the success of the method presented here.

As seen in the case of the South Rayan dune field, dunes located there are more likely to show SAR bright pixels on their large tail, which our approach sometimes cuts off from the dune, affecting their detected area, and hence their movement. However, this has not been found in dunes located in the West Sahara-Mauritania dune field.

It is important to note that on the SRDF site, for some cases we have tried to measure movements near the limit of the detection error, as one pixel counts for 20 m, and this is, on average, the distance an average dune in that field will move in four years, at the speed of 5 m/yr. Hence, we obtained better results for longer periods (i.e., 2000 to 2019 or 2004 to 2014).

Moreover, special attention must be paid to the proper geolocation of the satellite data, to avoid misalignments among data coming from different sensors, as is the case for the older dataset employed, i.e., ERS-2 SAR, and as we have shown happens on the WSM test site, but not on the SRDF. Note that this misalignment does not happen with the newer satellite data, as seen with Envisat and Sentinel-1.

Despite our both dune fields moving mainly in the N-S direction, we consider that our method should work as well in dune fields where the main direction is E-W as there is no constraint in our method that limits the migration direction.

Anywhere where no criterion is applied based on dune area consistency (area loss < 0.2), individual dune migration information might be perturbed.

Future research directions will lead to an enhancement of the method we propose to enable dune matching even for dunes that do not overlap using computer vision algorithms and analyzing dunes in both ascending and descending orbits when possible.

4.5.2. Implications in other domains

Climate change studies point towards the increase in wind speed on Earth, which will directly affect the dune dynamics of entire dune fields. Our automatic approach could be used to measure such wind variations of dune fields from all the world, providing results more rapidly and in a systematic manner. This systematic and global monitoring is not possible using other non-automatic techniques, such as traditional field campaigns or using optical data, the limitations of which were already mentioned in the introduction section.

Deriving the dune migration information from multiple dates, and obtaining the dune speed and movement direction could help to derive wind parameters, such as average direction, speed or the possible variations of them over time. This could help us to understand whether these conditions have changed over time during the analyzed periods.

Moreover, extra-planetary research, as already mentioned in the introduction section, has observed dunes on Mars and Titan. Hence, applying the proposed approach when sufficient data is available could help measure wind speeds on their surface. These wind speeds could become crucial pieces of information for the planning of space exploration missions, especially for those planning to land on them.

4.6. Conclusions

We have developed a totally automatic approach to measure dune dynamics, and have applied it to different test sites where barchan dunes move freely, but at different speeds and in different directions, showing the robustness of our method.

We have demonstrated the possibility of extending the applicability of techniques that were originally developed for other purposes, such as flood mapping, to dune dynamic analysis, due to the similar behavior of dunes and water to the SAR co-polarized signal, and hence we have also demonstrated the usability of SAR data for dune migration analysis at scale.

The proposed methodology has been demonstrated to work on isolated barchan dunes and provides dune migration information about dunes with an overlap between images. This methodology can be exported to other barchan dune fields. As a future work, the applicability of this method to other dune types could be explored.

We have measured, for our analyzed time period, dune migration rates of 11–20 m/yr moving in a south–south westerly direction for the West Sahara/Mauritania study area and 2–6 m/yr moving in a south-easterly direction for the South Rayan dune field, being very consistent with the available ground truth being 13–28 m/yr and 3–5 m/yr respectively.

5

Conclusions and Recommendations

IN this final chapter, the findings from the research will be discussed in the light of the research questions introduced in chapter 1. We also discuss the scientific and technical achievements and evaluate the potential of the developed methods and their applications. Finally, a set of recommendations is provided.

5.1. Conclusions

The main objective of this research is to improve methodologies to analyze the multi-temporal evolution of some specific landscape features due to natural and anthropogenic dynamics with a focus on Egypt. Below, we provide an answer to the main research questions:

- **Can current urban classification methods be improved by using satellite SAR data and machine learning techniques? Are we able to provide accurate urban expansion maps over urban and rural areas in Egypt?**

In chapter 2 and chapter 3 we presented two different methodologies, one using Multi-Spectral, SAR and SAR interferometric coherence data and the second based on exploiting large Multi-Spectral and SAR amplitude time series data, both using machine learning data fusion approaches for multi-temporal land cover classification. In chapter 2, we have demonstrated that introducing SAR and SAR interferometric coherence together with information derived from the optical satellites overcomes limitations imposed by the usage of optical satellite data only, while in chapter 3, we have exploited the statistics derived from large satellite data from SAR and optical sensors to derive accurate land cover maps.

With these methods, we improved the discrimination of urban features in arid regions and defined a new land use class that captures the transitions between the desert and urban classes, even in the early stages of construction. By using this new

class it was possible to detect areas subject to continuous changes, such as the Giza Pyramids World Heritage Cultural Site due to the intense movement of cars, buses, and people. And it was also possible to see the transition of the highly visited area to a less disturbed area after the Spring Arab Revolution. The reduction of such UAD class over the Giza Pyramid WHS during the period from 2010 to 2015 correlates with the reduction of tourists during several years after the revolution (see page 27).

Recently developed land cover classification strategies follow similar approaches to the ones developed in this work, such as in the new *WorldCover* (ESA, 2021b) and *WorldCereal* (ESA, 2021a) or the already completed *SinCohMap* (ESA, 2019), among others. Our land classification maps improved the urban detection of state-of-the-art global layers, i.e. we detect more than 6% more urban areas over the Greater Cairo area when comparing with ESA-CCI¹ using GUF² as reference dataset. In particular, we improved the detection of urban features located with respect to ESA-CCI and GHSL³ at least when analyzing at local and regional scale. Our maps show a better match with the urban areas visible in Google Earth datasets, where the ESA-CCI underestimates old city centers and GHSL misses, in some cases, entire cities located outside the floodplain, as it happened with New Al-Minya city, as shown in Fig. 3.9 (page 47).

It shall be highlighted that the above-mentioned layers used different methods, and satellite data and were developed with global data from heterogeneous areas, while the proposed method has been developed with data specifically collected for the study areas presented in this dissertation.

Results of our research showed a continuous increase of urban areas in within the Nile floodplain, causing a reduction of crop fields. In chapter 2, we have measured the Greater Cairo urban extent in 1998 corresponded to 381 km^2 and, from 1998 to 2015, the urban areas increased by 427 km^2 . These new urban areas were constructed on previous cropland (almost 160 km^2), but also within the desert areas (over 267 km^2) over both previous desert and UAD classes. In chapter 3, we have measured an increase of urban area of 53 km^2 within the Valley at expenses of cropland, and we have also seen how new cities appeared within desert areas (i.e. New Al-Minya). In addition, we have measured a decrease of agricultural land (hectares per person) and, a decrease of urban population density, meaning that new urban areas become more residential.

These results show that the building activities over fertile soil had never stopped during the analysed period, despite government's efforts, as urban areas continued to appear on the Nile Valley, reducing fertile cropland areas. However, new urban areas had growth within the desert, such as New Cairo, Pyramids Gardens, 6th October, Sheikh Zayed city and New Al-Minya.

Moreover, within the period 2010-2015, both crop fields and urban areas had proliferated in an accelerated rate in areas inside the desert areas (page 43). More than 200 km^2 of cropland appeared within the desert areas during this period on the analysed part of the Middle Egypt region. Probably part of these new croplands in the desert would be later abandoned, as suggested in (NASA Earth Observatory, 2021), but this could be the scope of future work. Finally, our resulting urban detection excludes cemeteries, which

¹ESA-Climate Change Initiative: Land Cover — S2 Prototype land cover 20 m map of Africa

²Global Urban Footprint of the German Aerospace Center

³JRC Global Human Settlements Layers

allows us to better compute population density estimates on urban areas. More precise information on the quality assessment is described in chapter 2 and chapter 3.

- **Can satellite SAR data help to improve the current methods of dune migration analysis? Can this analysis be done automatically? Can this be done at dune field scale?**

In chapter 4 we presented a new fully automatic method, which exploits C-band SAR data to derive dune dynamics information on isolated barchan dunes. We have tested this method in two dune fields with different dune migration characteristics. This is the first automatic method using SAR C-band presented in literature designed for this purpose and that facilitates dune migration analysis at dune-field scale.

The results correlate with values found in literature, demonstrating that our method allows for fast, automatic, and accurate barchan dune migration mapping. Our approach is as fast as almost near-real time, and as accurate as other approaches which may be not automatic and more expensive. Contrary to the results used for the comparison, derived from Landsat data using a method that required manual intervention, our method operated fully automatic, which facilitates operational applications. Other contemporary methods are based on optical satellite data (with its intrinsic limitations), or on VHR resolution optical data, which is expensive. The C-band SAR data employed in this study is weather independent, and free, which can be even more beneficial for areas where clouds is a real problem.

5.2. Contributions

The main contributions of this research are summarized as follows:

1. The development of two urban detection methods, fusing SAR, SAR coherence, Multi-spectral and Thermal data with ANN classifiers.
2. The generation of urban detection maps that improve existing urban maps produced by ESA and JRC, in our specific region of interest, using single sensor data (Delgado Blasco et al., 2013, 2020).
3. The definition of a new land cover class, Undefined Anthropogenic Disturbances (UAD), allowing to identify new urban areas, i.e., urban being built or completed, see chapter 2.
4. Prove that the use of temporal statistical data for LULC mapping improves traditional methods that employ a single satellite image (SAR and/or optical) see chapter 3.
5. Development of an automatic method for dune dynamics using SAR data, which is able to provide dune dynamics information in a reliable and robust way, see chapter 4. The method is exportable to other environments containing sand dunes, including extraterrestrial dune fields found on Mars and Titan. The method is able to provide dune migration rates and directions of individual barchan dunes.

While demonstrated on the test sites used in this study, our methods can be used in other (arid) environments, such as urban expansion in countries with similar environmental conditions to Egypt, such as Tunisia, Sudan, or the United Arab Emirates (UAE). The methods could be used by authorities, NGOs, or other entities which need updated and accurate information about urban expansion.

The dune migration analysis are particularly important when dunes represent a hazard, e.g., when they are moving towards villages or agricultural fields, but also when oil and gas companies plan to install new wells in desert areas, to avoid installing them in the dune's path. Dune migration can be monitored using SAR data and the technique developed in chapter 4. The techniques may be valuable for Mars landing mission planning, as a Mars lander may bounce several times and end up near active dunes, cf. (Kavulich Jr, 2008).

Regarding the implications for society, the results indicate that Egyptian crop field areas are not increasing at the same pace as population growth in rural areas such as the Middle Egypt region, and that the new urban areas built in there are more residential, as the population urban density decreased.

5

5.3. Recommendations

Despite the existence of Global land cover layers, regional geospatial studies need to be performed using dedicated regional maps, because they have shown to be more accurate than global layers, as they are generated using techniques specifically designed and trained on data from that region.

Secondly, the fusion of SAR and multi-spectral satellites is able to overcome each sensor's limitations, and hence we recommend the usage of data fusion approaches when analyzing landscape dynamics in similar environments.

It is also recommended to extend this work following the same approach, especially to understand how tourism activities evolved in Greater Cairo, as it is highly relevant to understand how to monitor tourism activities from space.

In this research, we have focused on the land cover dynamics while it is recommended to analyze also the land use, as combining both information sources it is possible to provide a more detailed and precise urban population density, as in this research we assumed the urban population density to be uniformly distributed over the detected urban cover areas. Hence imperviousness information could be retrieved and applied together with the land cover classes to improve the reported figures in this research.

The correlation of SAR and optical data and their capabilities of reconstructing cloudy optical data should be investigated.

Due to the presence of speckle in SAR data and its difficulties for image interpretation, the use of SAR data with a high revisit frequency is recommended, so that their derived temporal statistics are able to better discriminate the different land use classes. When such high temporal acquisition density is not available, such as for the historical ERS and Envisat missions, it is recommended to add interferometric coherence products to compensate it. However, the best combination, when possible, is to use both high temporal density SAR datasets as well as their derived interferometric coherence to achieve the most accurate results.

It is also recommended to use online platforms as they are a valuable tool for fast prototyping, algorithm development, and for using large volume datasets. However, currently, there is no online processing platform that provides analysis-ready data for both SAR and InSAR products. This makes the usage of both SAR high temporal density data and their interferometric coherence products more difficult.

Due to the highly changing environment in Egypt, we recommend national authorities to operationally implement the analysis described in this dissertation to generate more frequent maps, since our results showed that, despite the government's efforts initiated after the 1996 population census from which they tried to avoid new constructions on the Nile floodplain, agricultural fields within the floodplain have been replaced by urbanized areas for the whole analyzed period, and it might be happening still today.

Furthermore, since the automatic algorithm described in chapter 4 has been tested only on barchan dunes and located in desert areas with a specific geomorphological set-up, we recommend proceeding with further testing of our algorithm for different desert environments and for other dune types. Besides, it is recommended to possess a prior knowledge of the average dune migration rates/speeds as this is needed for an appropriate data sampling selection to be employed for the analysis. In case this information is not available, we suggest using a data sampling of 1 year.

New technologies such as deep learning techniques could be explored for enhancing data and methods of this research, in particular for: SAR speckle noise reduction, end-to-end dune dynamics analysis, and land classification purposes.

Finally, multidisciplinary research is recommended for increasing the impact of the new products and methods developed for analyzing its social-economic, cultural and geological implications.

Bibliography

- Adriansen, H. K. (2009). Land reclamation in Egypt: A study of life in the new lands. *Geoforum*, 40(4):664–674.
- Ahmed Mutasim Abdalla Mahmoud, The Conversation (2021). In Sudan, shifting sand dunes threaten the world's largest collection of pyramids. <https://scroll.in/article/998119/in-sudan-shifting-sand-dunes-threaten-the-worlds-largest-collection-of-pyramids>. accessed: 27 June 2021.
- Al-Harathi, A. (2002). Geohazard assessment of sand dunes between Jeddah and Al-Lith, western Saudi Arabia. *Environmental Geology*, 42(4):360–369.
- Altman, D. G. (1991). Mathematics for kappa. *Practical Statistics for Medical Research*, pages 406–407.
- Angel, S., Parent, J., Civco, D. L., and Blei, A. M. (2010). *Persistent Decline in Urban Densities: Global and Historical Evidence of 'Sprawl'*. Lincoln Institute of Land Policy.
- Angiuli, E. and Trianni, G. (2014). Urban mapping in Landsat images based on normalized difference spectral vector. *IEEE Geoscience and Remote Sensing Letters*, 11(3):661–665.
- ARRAY (2010). NEST-Calibration Operator.
- Arteaga, C., de Sanjose, J., and Serrano, E. (2008). Terrestrial photogrammetric techniques applied to the control of a parabolic dune in the Liencres dune system, Cantabria (Spain). *Earth Surface Processes and Landforms*, 33(14):2201–2210.
- Ashman, K. M., Bird, C. M., and Zepf, S. E. (1994). Detecting bimodality in astronomical datasets. *arXiv preprint astro-ph/9408030*.
- Aswatha, S. M., Mukhopadhyay, J., and Biswas, P. K. (2016). Spectral slopes for automated classification of land cover in landsat images. In *2016 IEEE International Conference on Image Processing (ICIP)*, pages 4354–4358. IEEE.
- Atkinson, P. M. and Tatnall, a. R. L. (1997). Introduction Neural networks in remote sensing. *International Journal of Remote Sensing*, 18(4):699–709.
- Baptista, P; Bastos, L; Bernardes, C; Cunha, T; Dias, J. (2008). Monitoring sandy shores morphologies by DGPS-a practical tool to generate digital elevation models. *Journal of Coastal Research*2, pages 1516–1528.

- Barnes, J. (2001). Barchan dunes on the Kuiseb River delta, Namibia. *South African Geographical Journal*, 83(3):283–292.
- Barnes, J. (2012). Pumping possibility: Agricultural expansion through desert reclamation in Egypt. *Social Studies of Science*, 42(4):517–538.
- BELSPO (2019). APLADYN - Anthropogenic and physical landscape dynamics in large fluvial systems? "<https://eo.belspo.be/en/stereo-in-action/projects/anthropogenic-and-physical-landscape-dynamics-large-fluvial-systems>". accessed: 03-10-2022.
- Bignami, C., Chini, M., Amici, S., and Trasatti, E. (2020). Synergic Use of Multi-Sensor Satellite Data for Volcanic Hazards Monitoring: The Fogo (Cape Verde) 2014–2015 Effusive Eruption. *Frontiers in Earth Science*.
- Blumberg, D. (2006). Analysis of large aeolian (wind-blown) bedforms using the Shuttle Radar Topography Mission (SRTM) digital elevation data. *Remote Sensing of Environment*, 100(2):179–189.
- Blumberg, D. G. (1998). Remote sensing of desert dune forms by polarimetric synthetic aperture radar (SAR). *Remote Sensing of Environment*.
- Bowden, L. W. and Brooner, W. G. (1970). Aerial photography: A diversified tool. *Geoforum*, 1(2):19–32.
- Brink, A. B., Bodart, C., Brodsky, L., Defournay, P., Ernst, C., Donney, E., Lupi, A., and Tuckova, K. (2014). Anthropogenic pressure in east africa—monitoring 20 years of land cover changes by means of medium resolution satellite data. *International Journal of Applied Earth Observation and Geoinformation*, 28:60–69.
- Brinkmann, K., Schumacher, J., Dittrich, A., Kadaore, I., and Buerkert, A. (2012). Analysis of landscape transformation processes in and around four West African cities over the last 50 years. *Landscape and Urban Planning*, 105(1-2):94–105.
- Bruzzzone, L., Marconcini, M., Wegmuller, U., Wiesmann, A., Member, S., and Wegmüller, U. (2004). An advanced system for the automatic classification of multitemporal SAR images.
- Bruzzzone, L. and Prieto, D. F. (2002). An adaptive semiparametric and context-based approach to unsupervised change detection in multitemporal remote-sensing images. *IEEE Transactions on image processing*, 11(4):452–466.
- Buynevich, I. V., Bitinas, A., Souza-Filho, P. W. M., Pupienis, D., Asp, N. E., Goble, R. J., and Kerber, L. E. (2011). Rapid coastal dune migration into temperate and equatorial forests: optical chronology of imaged upper slipface strata. *Journal of Coastal Research*, pages 726–730.
- Central Agency for Public Mobilization and Statistics (CAPMAS). (2017). Egypt Administrative Boundaries. <https://www.diva-gis.org>.

- Cetin, M., Kavzoglu, T., and Musaoglu, N. (2004). Classification of multi-spectral, multi-temporal and multi-sensor images using principal components analysis and artificial neural networks: Beykoz case. In *XXth International Society for Photogrammetry and Remote Sensing-Congress*, pages 12–23.
- Chander, G., Markham, B. L., and Helder, D. L. (2009). Summary of current radiometric calibration coefficients for Landsat MSS, TM, ETM+, and EO-1 ALI sensors. *Remote Sensing of Environment*, 113(5):893–903.
- Chettri, S. R., Crompton, R. F., and Birmingham, M. (1992). Design of neural networks for classification of remotely sensed imagery. *Telematics and Informatics*, 9(3-4):145–156.
- Chini, M., Hostache, R., Giustarini, L., and Matgen, P. (2017a). A hierarchical split-based approach for parametric thresholding of SAR images: Flood inundation as a test case. *IEEE Transactions on Geoscience and Remote Sensing*, 55(12):6975–6988.
- Chini, M., Hostache, R., Giustarini, L., and Matgen, P. (2017b). A hierarchical split-based approach for parametric thresholding of SAR images: Flood inundation as a test case. *IEEE Transactions on Geoscience and Remote Sensing*, 55(12):6975–6988.
- Chini, M., Pelich, R., Hostache, R., Matgen, P., and Lopez-Martinez, C. (2018). Towards a 20 m global building map from sentinel-1 sar data. *Remote Sensing*, 10(11):1833.
- Cobbinah, P. B., Erdiaw-Kwasie, M. O., and Amoateng, P. (2015). Africa's urbanisation: Implications for sustainable development. *Cities*, 47:62–72.
- Cohen, B. (2006). Urbanization in developing countries: Current trends, future projections, and key challenges for sustainability. *Technology in Society*, 28(1-2):63–80.
- Cohen, J. (1960). A Coefficient of Agreement for Nominal Scales. *Educational and Psychological Measurement*, 20(1):37–46.
- Congalton, R. G. (1991). A Review of Assessing the Accuracy of Classifications of Remotely Sensed Data. *Remote Sensing of Environment*, 46(October 1990):35–46.
- Corbane, C., Pesaresi, M., Politis, P., Syrris, V., Florczyk, A. J., Soille, P., Maffenini, L., Burger, A., Vasilev, V., Rodriguez, D., and Others (2017). Big earth data analytics on Sentinel-1 and Landsat imagery in support to global human settlements mapping. *Big Earth Data*, 1(1-2):118–144.
- Corbane, Christina; Politis, Panagiotis; Syrris, Vasileios; Pesaresi, M. (2018). GHS built-up grid, derived from Sentinel-1 (2016), R2018A. European Commission, Joint Research Centre (JRC).
- de Noronha Vaz, E., Caetano, M., and Nijkamp, P. (2011a). A multi-level spatial urban pressure analysis of the Giza pyramid plateau in Egypt. *Journal of Heritage Tourism*, 6(2):99–108.
- de Noronha Vaz, E., Caetano, M., and Nijkamp, P. (2011b). A multi-level spatial urban pressure analysis of the Giza Pyramid Plateau in Egypt Research Memorandum 2011-43.

- Del Frate, F., Pacifici, F., and Solimini, D. (2007). Urban land cover in rome, italy, monitored by single-parameter multi-temporal sar images. In *2007 Urban Remote Sensing Joint Event*, pages 1–5. IEEE.
- Delgado Blasco, J., Sabatino, G., Cuccu, R., Rivolta, G., Giorgio, P., and Marchetti, M. (2016). Research and service support: Bringing users to data. In *European Space Agency, (Special Publication) ESA SP*, volume SP-740.
- Delgado Blasco, J., Verstraeten, G., and Hanssen, R. (2017). Detecting modern desert to urban transitions from space in the surroundings of the Giza World Heritage site and Greater Cairo. *Journal of Cultural Heritage*, 23.
- Delgado Blasco, J. M., Cian, F., Hanssen, R. F., and Verstraeten, G. (2020). Mapping and quantifying the human-environment interactions in middle egypt using machine learning and satellite data fusion techniques. *Remote Sensing*, 12(3):584.
- Delgado Blasco, J. M., Verstraeten, G., and Hanssen, R. F. (2013). Monitoring the urban expansion of Cairo from 2004 to 2010 through SAR data using a non-parametric supervised classifier. In *Proc. 'Living Planet Symposium 2013', Edinburgh, UK 9–13 September 2013 (ESA SP-722, December 2013)*, volume 1. ESA Communications ESTEC, Noordwijk, The Netherlands.
- Dong, N., Liu, Z., Luo, M., Fang, C., and Lin, H. (2019). The effects of anthropogenic land use changes on climate in china driven by global socioeconomic and emission scenarios. *Earth's Future*, 7(7):784–804.
- El-Bayomi, G., & Ali, R. R. (2015). Assessment of Urban Sprawl on El Minya Archeological Sites, Egypt. *Journal of Applied Sciences*, 15(2):264–270.
- El Gammal, E. S. A. and El Gammal, A. E. D. A. (2010). Hazard impact and genetic development of sand dunes west of Samalut, Egypt. *Egyptian Journal of Remote Sensing and Space Science*.
- Embabi, N. S. (2004). The geomorphology of Egypt, landforms and evolution, Volume I: The Nile Valley and the Western Desert. *Spec. Pub., Egypt. Geograph. Soc*, 447.
- ESA (2019). The Sentinel-1 Interferometric Coherence for Vegetation and Mapping (SInCohMap) project. <http://www.sincohmap.org/>. accessed: 2021-10-09.
- ESA (2021a). The ESA WorldCereal Project. <https://esa-worldcereal.org/en>. accessed: 2021-10-09.
- ESA (2021b). The ESA WorldCover Project. <https://esa-worldcover.org/en>. accessed: 2021-10-09.
- Esch, T., Heldens, W., Hirner, A., Keil, M., Marconcini, M., Roth, A., Zeidler, J., Dech, S., and Strano, E. (2017). Breaking new ground in mapping human settlements from space–The Global Urban Footprint. *ISPRS Journal of Photogrammetry and Remote Sensing*, 134:30–42.

- Esch, T., Schenk, A., Ullmann, T., Thiel, M., Roth, A., and Dech, S. (2011). Characterization of land cover types in TerraSAR-X images by combined analysis of speckle statistics and intensity information. *IEEE Transactions on Geoscience and Remote Sensing*, 49(6):1911–1925.
- European Space Agency (2017). CCI Land Cover -Sentinel-2 Prototype Land Cover 20m of Africa 2016. <http://2016africallandcover20m.esrin.esa.int/>.
- European Space Agency. (2019). Some Commonly Used EO Satellite Systems.
- Florczyk, A., Politis, P., Corbane, C., and Pesaresi, M. (2018). GHS-BUILT R2018A - GHS built-up grid INPUT DATA, Landsat multitemporal collections (1975-1990-2000-2014). European Commission, Joint Research Centre (JRC).
- Florczyk, Aneta; Politis, Panagiotis; Corbane, Christina; Pesaresi, M. (2018). GHS-BUILT R2018A - GHS built-up grid INPUT DATA, Landsat multitemporal collections (1975-1990-2000-2014). European Commission, Joint Research Centre (JRC).
- Ghadiry, M. and Koch, B. (2010). Developing a monitoring system for sand dunes migration in dakhla oasis, western desert, egypt. In *Proceedings of the 30th EARSeL Symposium on Remote Sensing for Science, Education and Culture, Paris, France*, volume 31.
- Giustarini, L., Hostache, R., Matgen, P., Schumann, G. J.-P., Bates, P. D., and Mason, D. C. (2012). A change detection approach to flood mapping in urban areas using TerraSAR-X. *IEEE transactions on Geoscience and Remote Sensing*, 51(4):2417–2430.
- Gorelick, N. (2012). Google Earth Engine. In *AGU Fall Meeting Abstracts*, volume 1, page 4.
- Gouinaud, C., Doutoum, A. I., Gouinaud, P., and Traore, M. K. (2013). SAR IMAGE AUTOMATED DETECTION OF DUNE AREA. In *IGARSS 2013*, pages 1489–1492.
- Government of Western Australia (2017). Migrating sand dunes pose potential risks to roads, homes and infrastructure. <https://www.dmp.wa.gov.au/News/Migrating-sand-dunes-pose-21368.aspx>. accessed: 4 September 2022.
- Graser, A. (2013). *Learning QGIS 2.0*. Packt Publishing Ltd.
- Greenwatch Trust, Twitter (2022). Somalia in worst Desertification! Not only drought, sand dunes affected the water wells infrastructure in Dhinowda village 30KM from Garacad (Mudug). <https://twitter.com/GreenwatchTrust/status/1543601952331862020>. accessed: 4 July 2022.
- Griffiths, P., Hostert, P., Gruebner, O., and van der Linden, S. (2010). Mapping megacity growth with multi-sensor data. *Remote Sensing of Environment*, 114(2):426–439.
- Hanssen, R. F. (2001). *Radar Interferometry: Data Interpretation and Error Analysis*. Kluwer Academic Publishers, Boston, MA (USA).

- Harms, H. (2017). Challenges for sustainable development of informal settlements and of desert new towns in Cairo. In *Revitalizing City Districts*, pages 147–169. Springer.
- Harris, R. and Wahba, M. (2002). The Urban Geography of Low-Income Housing : Cairo (1947 – 96) Exemplifies a Model. *International Journal of Urban and Regional Research*, 26(March):58–79.
- Hassan, A. A. M. (2011). Change in the urban spatial structure of the Greater Cairo metropolitan area, Egypt. *Archives*, XXXVIII(Udms):133–136.
- Havivi, S., Amir, D., Schwartzman, I., August, Y., Maman, S., Rotman, S. R., and Blumberg, D. G. (2018). Mapping dune dynamics by InSAR coherence. *Earth Surface Processes and Landforms*, 43(6):1229–1240.
- Hegazy, I. R. (2016). Informal settlement upgrading policies in Egypt: towards improvement in the upgrading process. *Journal of Urbanism: International Research on Placemaking and Urban Sustainability*, 9(3):254–275.
- Hermas, E. A., Elmagd, I. H. A., Alharbi, K., and Al-mukkarramah, M. (2004). MEASUREMENT OF SAND DUNE MOVEMENTS USING THE SUB-PIXEL CORRELATION OF ASTER IMAGES : A PREMIMINARY RESULTS FROM NORTH SINAI ,. *Sciences-New York*, pages 1–4.
- Horvat, B. (2006). Barchan dunes Seminar 2. <http://www-fl.ijs.si/~rudi/sola/Sem4.pdf>.
- Hou, H., Estoque, R. C., and Murayama, Y. (2016). Spatiotemporal analysis of urban growth in three African capital cities: A grid-cell-based analysis using remote sensing data. *Journal of African Earth Sciences*, 123:381–391.
- Hugenholtz, C. H., Levin, N., Barchyn, T. E., and Baddock, M. C. (2012). Remote sensing and spatial analysis of aeolian sand dunes: A review and outlook. *Earth-Science Reviews*, 111(3-4):319–334.
- Hush, D. (1989). Classification with neural networks: a performance analysis. In *Proceedings of the IEEE International Conference on Systems Engineering, Dayton, Ohio, USA*, pages 277–280.
- Ibrahim, M. R. and Masoumi, H. E. (2016). Will Distance to the Capital City Matter When Supplying New Cities in Egypt? *GeoScape*, 10(2):35–52.
- Inostroza, L., Hamstead, Z., Spyra, M., and Qhreshi, S. (2019). Beyond urban–rural dichotomies: Measuring urbanisation degrees in central European landscapes using the technomass as an explicit indicator. *Ecological indicators*, 96:466–476.
- Joshi, N., Baumann, M., Ehammer, A., Fensholt, R., Grogan, K., Hostert, P., Jepsen, M., Kuemmerle, T., Meyfroidt, P., Mitchard, E., and Others (2016). A review of the application of optical and radar remote sensing data fusion to land use mapping and monitoring. *Remote Sensing*, 8(1):70.

- Kalensky, Z. D. (1998). AFRICOVER land cover database and map of Africa. *Canadian journal of remote sensing*, 24(3):292–297.
- Kampes, B. M., Hanssen, R. F., and Perski, Z. (2003). Radar Interferometry With Public Domain Tools. In *Third International Workshop on ERS SAR Interferometry "FRINGE 2003"*, page 6 pp, Frascati, Italy.
- Kanellopoulos, I. and Wilkinson, G. (1997). Strategies and best practice for neural network image classification. *International Journal of Remote Sensing*, 18:711–725.
- Karan, P. P. (1960). A land use reconnaissance in nepal by aero-field techniques and photography. *Proceedings of the American Philosophical Society*, 104(2):172–187.
- Karuga, J. (2019). 15 biggest cities in africa. World Facts.
- Kavulich Jr, M. J. (2008). *The Physics of Sand Dune Formation and Migration on Mars*. PhD thesis, WORCESTER POLYTECHNIC INSTITUTE.
- Käyhkö, J. (2007). Aeolian blowout dynamics in subarctic Lapland based on decadal levelling investigations. *Geografiska Annaler: Series A, Physical Geography*, 89(1):65–81.
- Keerthi S. S., L. C. J. (2003). Asymptotic behaviors of support vector machines with Gaussian kernel. *Neural computation*, 15(7):1667–1689.
- Kostaschuk, R. and Best, J. (2005). Response of sand dunes to variations in tidal flow: Fraser Estuary, Canada. *Journal of Geophysical Research: Earth Surface*, 110(F4).
- Kozlov, V. (1979). Use of satellite photographs to study deep crustal structures of petro-liferous regions. report iii. lineaments of the aral-caspian region, their classification and association with fractures. *International Geology Review*, 21(11):1337–1344.
- Łabuz, T. A. (2016). A review of field methods to survey coastal dunes—experience based on research from South Baltic coast. *Journal of Coastal Conservation*, 20(2):175–190.
- Lancaster, N. (1994). Dune morphology and dynamics. In *Geomorphology of desert environments*, pages 474–505. Springer.
- Landis, J. R. and Koch, G. G. (1977). The measurement of observer agreement for categorical data. *biometrics*, pages 159–174.
- Law, G. (2016). Egypt Governorates: Population history.
- Le Gall, a., a.G. Hayes, Ewing, R., Janssen, M., Radebaugh, J., Savage, C., and Encrenaz, P. (2012). Latitudinal and altitudinal controls of Titan's dune field morphometry. *Icarus*, 217(1):231–242.
- Lesiv, M., Fritz, S., McCallum, I., Tsendbazar, N., Herold, M., Pekel, J.-F., Buchhorn, M., Smets, B., and Van De Kerchove, R. (2017). Evaluation of ESA CCI prototype land cover map at 20m. *Working Paper of the International Institute for Applied Systems Analysis*.

- Li, S. and Chen, X. (2014). A new bare-soil index for rapid mapping developing areas using landsat 8 data. *The International Archives of Photogrammetry, Remote Sensing and Spatial Information Sciences*, 40(4):139.
- Li, Y. (2012). Urban–rural interaction patterns and dynamic land use: implications for urban–rural integration in China. *Regional Environmental Change*, 12(4):803–812.
- Livingstone, I., Wiggs, G. F. S., and Weaver, C. M. (2007). Geomorphology of desert sand dunes: A review of recent progress. *Earth-Science Reviews*, 80(3-4):239–257.
- Lopes, R. M. C., Stofan, E. R., Peckyno, R., Radebaugh, J., Mitchell, K. L., Mitri, G., Wood, C., Kirk, R. L., Wall, S. D., Lunine, J. I., Hayes, a., Lorenz, R., Farr, T., Wye, L., Craig, J., Ollerenshaw, R. J., Janssen, M., LeGall, a., Paganelli, F., West, R., Stiles, B., Callahan, P., Anderson, Y., Valora, P., and Soderblom, L. (2010). Distribution and interplay of geologic processes on Titan from Cassini radar data. *Icarus*, 205(2):540–558.
- López-Caloca, A. A. (2015). Data fusion approach for Urban area identification using multisensor information. In *8th International Workshop on the Analysis of Multitemporal Remote Sensing Images (Multi-Temp)*. IEEE, 2015. IEEE.
- Lorenz, R. D., Gasmi, N., Radebaugh, J., Barnes, J. W., and Ori, G. G. (2013a). Dunes on planet Tatooine: Observation of barchan migration at the Star Wars film set in Tunisia. *Geomorphology*, 201:264–271.
- Lorenz, R. D., Gasmi, N., Radebaugh, J., Barnes, J. W., and Ori, G. G. (2013b). Dunes on planet Tatooine: Observation of barchan migration at the Star Wars film set in Tunisia. *Geomorphology*.
- Luke, J. and King, D. T. (2019). Automated Object-Based Identification of Dunes at Hargraves Crater , Mars. In *50th Lunar and Planetary Science Conference, held 18-22 March, 2019 at The Woodlands, Texas. LPI Contribution No. 2132, id.1157*, pages 2–3.
- Manguet, M. (1984). Space observation of saharan aeolian dynamics. In *Deserts and arid lands*, pages 59–77. Springer.
- Marquardt, D. W. (1963). An algorithm for least-squares estimation of nonlinear parameters. *Journal of the society for Industrial and Applied Mathematics*, 11(2):431–441.
- Mather, P. M. and Koch, M. (2004). *Computer Processing of Remotely-Sensed Images: An introduction*. John Wiley & Sons Ltd, Chichester, UK., third edit edition.
- McInerney, D. and Kempeneers, P. (2015). Pktools. In *Open Source Geospatial Tools*, pages 173–197. Springer.
- Meikle, J. (2011). Note on: Informal Construction. In *International Cooperation Program 2011, 5th Technical Advisory Group Meeting*, Washington D.C., USA. World Bank.
- Milisavljevic, N., Closson, D., and Bloch, I. (2010). Detecting human-induced scene changes using coherent change detection in SAR images. In *ISPRS TC VII Symposium-100 Years ISPRS*, volume XXXVIII, pages 389–394.

- Miller, L. D. (1978). *Analysis of the dynamics of shifting cultivation in the tropical forests of northern Thailand using landscape modeling and classification of Landsat imagery*, volume 79545. National Aeronautics and Space Administration, Goddard Space Flight Center.
- Mitasova, H., Overton, M., and Harmon, R. S. (2005). Geospatial analysis of a coastal sand dune field evolution: Jockey's Ridge, North Carolina. *Geomorphology*, 72(1-4):204–221.
- Mohamed, H. E. (2012a). Analysis of urban growth at Cairo, Egypt using remote sensing and GIS. *Natural Science*, 4(6):355–361.
- Mohamed, I. and Verstraeten, G. (2010). Investigating dune dynamics of the South-Rayan Dune Field (Egypt) based on multi-temporal analysis of Landsat images. In *International Conference on Aeolian Research "ICAR VII"*, Date: 2010/07/05-2010/07/09, Location: Santa Rosa-LaPampa, Argentina.
- Mohamed, I. N. L. (2012b). *Evolution of South-Rayan Dune-Field (Central Egypt) and its interaction with the Nile fluvial system*. PhD thesis, KU Leuven.
- Mohamed, I. N. L. and Verstraeten, G. (2012). Analyzing dune dynamics at the dune-field scale based on multi-temporal analysis of Landsat-TM images. *Remote Sensing of Environment*, 119:105–117.
- NASA Earth Observatory (2021). The Nile Delta's Disappearing Farmland. <https://earthobservatory.nasa.gov/images/149183/the-nile-deltas-disappearing-farmland>. accessed: 2021-11-09.
- Nashashibi, A. Y., Sarabandi, K., Al-zaid, F. A., and Alhumaidi, S. (2012). Characterization of Radar Backscatter Response of Sand-Covered Surfaces at Millimeter-Wave Frequencies. *IEEE Transactions on Geoscience and Remote Sensing*, 50(6):2345–2354.
- New Urban Communities Authorities (2019). New Minia.
- Nuyts, S., O'Shea, M., and Murphy, J. (2020). Monitoring the morphodynamic cannibalization of the rossbeigh coastal barrier and dune system over a 19-year period (2001–2019). *Journal of Marine Science and Engineering*, 8(6):421.
- Osman, T., Arima, T., and Divigalpitiya, P. (2016). Measuring urban sprawl patterns in Greater Cairo Metropolitan Region. *Journal of the Indian Society of Remote Sensing*, 44(2):287–295.
- Ould Ahmedou, D., Ould Mahfoudh, A., Dupont, P., Ould El Moctar, A., Valance, A., and Rasmussen, K. R. (2007). Barchan dune mobility in mauritania related to dune and interdune sand fluxes. *Journal of Geophysical Research: Earth Surface*, 112(F2).
- Paillou, P., Bernard, D., Radebaugh, J., Lorenz, R., Le Gall, a., and Farr, T. (2014). Modeling the SAR backscatter of linear dunes on Earth and Titan. *Icarus*, 230:208–214.

- Paillou, P., Seignovet, B., Radebaugh, J., and Wall, S. (2016). Radar scattering of linear dunes and mega-yardangs: Application to Titan. *Icarus*.
- Pardo-Pascual, J. E., Garc\'ia-Asenjo, L., Palomar-Vázquez, J., and Garrigues-Talens, P. (2005). New methods and tools to analyze beach-dune system evolution using a Real-Time Kinematic Global Positioning System and Geographic Information Systems. *Journal of Coastal Research*, pages 34–39.
- Patel, N. N., Angiuli, E., Gamba, P., Gaughan, A., Lisini, G., Stevens, F. R., Tatem, A. J., and Trianni, G. (2015). Multitemporal settlement and population mapping from Landsat using Google Earth Engine. *Int. J. Applied Earth Observation and Geoinformation*, 35:199–208.
- Payette, S. and Filion, L. (1985). White spruce expansion at the tree line and recent climatic change. *Canadian Journal of Forest Research*, 15(1):241–251.
- Punkari, M. (1982). Glacial geomorphology and dynamics in the eastern parts of the baltic shield interpreted using landsat imagery. *Photogrammetric journal of Finland*, 9(1):77–93.
- Qong, M. (1996). Sand Dune Attributes Estimated from SAR Images. *Science*, 4257(00).
- Radebaugh, J., Lorenz, R., Farr, T., Paillou, P., Savage, C., and Spencer, C. (2010). Linear dunes on Titan and earth: Initial remote sensing comparisons. *Geomorphology*, 121(1-2):122–132.
- Radebaugh, J., Lorenz, R., Lunine, J., Wall, S., Boubin, G., Reffet, E., Kirk, R., Lopes, R., Stofan, E., Soderblom, L., Allison, M., Janssen, M., Paillou, P., Callahan, P., and Spencer, C. (2008). Dunes on Titan observed by Cassini Radar. *Icarus*, 194(2):690–703.
- Rosin, P. (1998). Thresholding for change detection. In *Sixth International Conference on Computer Vision (IEEE Cat. No. 98CH36271)*, pages 274–279.
- Said, R. (2012). *The geological evolution of the River Nile*. Springer Science & Business Media.
- Santalla, I. R., Garcia, M. J. S., Montes, I. M., Ortiz, D. G., Crespo, T. M., and Raventos, J. S. (2009). Internal structure of the aeolian sand dunes of El Fangar spit, Ebro Delta (Tarragona, Spain). *Geomorphology*, 104(3-4):238–252.
- Schneider, A. (2012). Monitoring land cover change in urban and peri-urban areas using dense time stacks of Landsat satellite data and a data mining approach. *Remote Sensing of Environment*, 124:689–704.
- Schneider, A. and Woodcock, C. E. (2008). Compact, dispersed, fragmented, extensive? A comparison of urban growth in twenty-five global cities using remotely sensed data, pattern metrics and census information. *Urban Studies*, 45(3):659–692.
- Shetawy, A. A. A. and El Khateeb, S. M. (2009). The pyramids plateau: A dream searching for survival. *Tourism Management*, 30(6):819–827.

- Silleos, N. G., Alexandridis, T. K., Gitas, I. Z., and Perakis, K. (2006). Vegetation indices: advances made in biomass estimation and vegetation monitoring in the last 30 years. *Geocarto International*, 21(4):21–28.
- Simone, G., Farina, a., Morabito, F., Serpico, S., and Bruzzone, L. (2002). Image fusion techniques for remote sensing applications. *Information Fusion*, 3(1):3–15.
- Song, Y., Chen, C., Xu, W., Zheng, H., Bao, A., Lei, J., Luo, G., Chen, X., Zhang, R., and Tan, Z. (2020). Mapping the temporal and spatial changes in crescent dunes using an interferometric synthetic aperture radar temporal decorrelation model. *Aeolian Research*, 46:100616.
- Stewart, D. J. (1996). Cities in the desert: the Egyptian new-town program. *Annals of the Association of American Geographers*, 86(3):459–480.
- Stewart, D. J., Yin, Z.-y., Bullard, S. M., and Maclachlan, J. T. (2004). Assessing the spatial structure of urban and population growth in the greater Cairo area, Egypt: a GIS and imagery analysis approach. *Urban Studies*, 41(1):95–117.
- Strozzi, T. and Wegmuller, U. (1998). Delimitation of Urban Areas with SAR Interferometry. In *Geoscience and Remote Sensing Symposium Proceedings, 1998. IGARSS '98. 1998 IEEE International*, pages 1632–1634.
- Sutton, K. and Fahmi, W. (2001). Cairo's urban growth and strategic master plans in the light of Egypt's 1996 population census results. *Science*, 18(3):135–149.
- Taubenböck, H., Esch, T., Felbier, A., Wiesner, M., Roth, A., and Dech, S. (2012). Monitoring urbanization in mega cities from space. *Remote Sensing of Environment*, 117:162–176.
- Taubenböck, H., Wegmann, M., Roth, A., Mehl, H., and Dech, S. (2008). Analysis of urban sprawl at mega city Cairo , Egypt using multisensoral remote sensing data , landscape metrics and gradient analysis. *Area*.
- The Guardian (2010). "population of african cities to triple: Get the data," nov. 23, 2010.
- The World Bank Group (2017). "International tourism, number of arrivals", World Development Indicators. <https://databank.worldbank.org/reports.aspx?source=2&series=ST.INT.ARVL&country=EGY#>. accessed: 2017-09-11.
- Trianni, G., Angiuli, E., Lisini, G., and Gamba, P. (2014). Human settlements from landsat data using google earth engine. In *2014 IEEE Geoscience and Remote Sensing Symposium*, pages 1473–1476. IEEE.
- Tsoar, H. (2001). Types of aeolian sand dunes and their formation. In *Geomorphological fluid mechanics*, pages 403–429. Springer.
- Tupin, F. (2010). Fusion of optical and SAR images. *Radar Remote Sensing of Urban Areas*, pages 133–159.

- UNESCO, W. H. C. (2008). Operational Guidelines for the Implementation of the World Heritage Convention.
- U.S. Department of the Interior (2013). SLC-off Products: Background.
- USGS (2021). What are the band designations for the Landsat satellites? "<https://www.usgs.gov/faqs/what-are-band-designations-landsat-satellites>". accessed: 03-10-2022.
- USGS, U. S. (2018). Geological Survey (2019l): USGS EROS Archive–Digital Elevation–Shuttle Radar Topography Mission (SRTM) 1 Arc-Second Global.
- Vapnik, V. N. (1998). *Statistical Learning Theory*. John Wiley & Sons.
- Veci, L., Lu, J., Prats-Iraola, P., Scheiber, R., Collard, F., Fomferra, N., and Engdahl, M. (2014). The Sentinel-1 Toolbox. In *Proceedings of the IEEE International Geoscience and Remote Sensing Symposium (IGARSS)*., pages 1–3.
- Vermeesch, P. and Drake, N. (2008). Remotely sensed dune celerity and sand flux measurements of the world's fastest barchans (Bodele, Chad). *Geophysical Research Letters*, 35(24).
- Vermeiren, K., Van Rompaey, A., Loopmans, M., Serwajja, E., and Mukwaya, P. (2012). Urban growth of Kampala, Uganda: Pattern analysis and scenario development. *Landscape and Urban Planning*, 106(December 2015):199–206.
- Verstraeten, G., Mohamed, I., Notebaert, B., and Willems, H. (2017). The dynamic nature of the transition from the Nile floodplain to the desert in central Egypt since the Mid-Holocene. *Mainz Historical Cultural Sciences| Volume 36*, page 239.
- Verstraeten, G., Mohamed, I., Willems, H., De Laet, V., and Delgado Blasco, J. M. (2014). Analysis of Aeolian-Fluvial-Human Interactions in the Nile Valley (Central Egypt) by Combining Field-Based Geomorphology with Remote Sensing. In *34th EARSeL Symposium. 5th European Remote Sensing–New Opportunities for Science and Practice. Abstract and Programme Book. Warsaw, 16-20 June 2014*, volume 34, page 55. University of Warsaw.
- Vinogradov, B. (1977). Remote sensing in ecological botany. *Remote sensing of environment*, 6(2):83–94.
- Ward, D., Phinn, S. R., and Murray, A. T. (2000). Monitoring growth in rapidly urbanizing areas using remotely sensed data. *The Professional Geographer*, 52(3):371–386.
- WeatherOnline (2019). Wind speed forecasts. weatheronline.co.uk. accessed: 2019-05-01.
- Wegmüller, U., Strozzi, T., Farr, T., and Werner, C. L. (2000). Arid Land Surface Characterization with Repeat-Pass. *IEEE Transactions on Geoscience and Remote Sensing*, 38(2):776–781.

- Wikipedia (2018). Mallawi. <https://en.wikipedia.org/wiki/Mallawi>. accessed: 2018-06-29.
- Willems, H. and Dahms, J.-M. (2017). *The Nile: Natural and Cultural Landscape in Egypt : Proceedings of the International Symposium held at the Johannes Gutenberg-Universität Mainz, 22 & 23 February 2013*. transcript Verlag, Bielefeld, Germany.
- Willems, H. and Muammad, W. (2010). A note on the origin of the toponym al-Barshā. *The Journal of Egyptian Archaeology*, 96(1):232–236.
- Wippermann, F. and Gross, G. (1986). The wind-induced shaping and migration of an isolated dune: a numerical experiment. *Boundary-Layer Meteorology*, 36(4):319–334.
- Xie, H., Pierce, L. E., and Ulaby, F. T. (2002). Statistical properties of logarithmically transformed speckle. *IEEE Transactions on Geoscience and Remote Sensing*, 40(3):721–727.
- Zebker, H. A., Member, S., and Villasenor, J. (1992). Decorrelation in Interferometric Radar Echoes. *IEEE Transactions on Geoscience and Remote Sensing*, 30(5):950–959.
- Zhou, Y., Yang, G., Wang, S., Wang, L., Wang, F., and Liu, X. (2014). A new index for mapping built-up and bare land areas from Landsat-8 OLI data. *Remote sensing letters*, 5(10):862–871.

Acknowledgements

The whole life is full of life-changer decisions. To embrace the opportunity of pursuing this PhD is on the top of those decisions I have ever taken. Moving to The Netherlands and Belgium has literally changed my life, increasing the dimensions of my life, the personal life as much as the professional one. For this, I need to thank Prof. dr. ir. Ramon F. Hanssen, Prof. dr. Gert Verstraeten and dr. Véronique De Laet for choosing me to work with them. Moreover, I can only have gratitude to my both promotors for supporting me all this time, even being further away, after many years.

I want to thank my wife, my two sons, and my daughter, for all the understanding and time given so I could dedicate it to complete this research which was taken from my time with them.

Additionally, I want to have special words to all my friends and colleagues from Delft who shared with me many working days, coffee breaks, productive discussions, beers, and dinners, which made life away from home full of special moments, happiness, and joy. Among all these people I cannot forget Miguel Caro Cuenca, David Bekaert, Prabu Dheenthayalan, Pooja Mahapatra, Joana Esteves Martins, Anneleen Oyen, Sami Samiei Esfahany, Mahmut Arikan, Saygin Abdikan, and also to the best office mate Ling Chang, always listening and willing to help with a smile always ready. I cannot forget all the discussions with dr. Lorenzo Iannini and Ali Mousivand about classification indicators and atmospheric correction methods, which helped me a lot. Also in Delft, I had the chance to meet Prof Antonio M. Ruiz-Armenteros, which had helped me a lot during all these years, not only professionally.

Moreover, I want also to thank all the colleagues I made also in Leuven, such as Koen D'Haen, Ihab Mohamed, Karolien Vermeiren and all the professors there in the Geography and Tourism Unit, which made from all single break a family break. I will never forget the fabulous and incredible team building week prepared nearly upon my arrival. I cannot forget my two fascinating and incredible field-work campaigns in Egypt, which Prof. Harco Willems, Prof. dr. Rudi Goossens, dr. Véronique De Laet and Marijn Hendrickx made unique, together with all the people I have met at the KU Leuven base in Dayr al-Barsha.

Outside work, I do not want to forget to thank all the friends I have found in such northern latitudes, such as Eloi Sanfelix, Jorge Amor Río, Sara Salvador, Daniel León, Janos Keresztes, Rafael Boix, for making feeling at home every single day. My welcoming and living in Delft and Leuven could have never been better without them.

This research is within the framework of the APLADYN project funded by the STEREO II-program of the Belgian Science Policy-project SR/00/132. The authors acknowledge the use of ERS SAR and Envisat ASAR imagery provided by ESA under the CAT-1 C1P8230. This study contains modified Copernicus Sentinel data [2014, 2019]. Dr. Marco Chini work was funded by the National Research Fund of Luxembourg (FNR) through the MOSQUITO project, grant number C15/SR/10380137.

About the author

José Manuel Delgado Blasco was born on 27 September 1981 in Valencia, Spain. He completed his studies in Telecommunication Engineering at the Polytechnic University of Valencia (UPV) in May 2010. This included two years as an Erasmus student in Rome, studying Earth Observation and Remote Sensing during a traineeship at ESA-ESRIN. In September 2010, he started a Ph.D. study at Delft University of Technology in a collaborative project, APLADYN, with the University of Leuven.

In September 2014 he moved to Frascati, Italy, where he started to work as Earth Observation Research Support Engineer as an ESA contractor, which allowed him to increase his network with European researchers from several Earth Observation domains. Since 2019 he works as Earth Observation expert engineer, developing a wide range of end-to-end applications, promoting open science, and collaborating with Prof. A.M. Ruiz-Armenteros as a Volunteer Researcher within the "Microgreodesia Jaén" Research Group of the University of Jaén.

List of related publications

Peer-reviewed journal articles

1. **J.M. Delgado Blasco**, M. Chini, G. Verstraeten, R.F. Hanssen, *Sand Dune Dynamics Exploiting a Fully Automatic Method Using Satellite SAR Data*, Remote Sensing, **12**(23), (2020).
2. **J.M. Delgado Blasco**, F. Cian, R.F. Hanssen, G. Verstraeten, *Mapping and Quantifying the Human-Environment Interactions in Middle Egypt Using Machine Learning and Satellite Data Fusion Techniques*, Remote Sensing, **12**(3), 584, (2020).
3. **J.M. Delgado Blasco**, G. Verstraeten, R.F. Hanssen, *Detecting modern desert to urban transitions from space in the surroundings of the Giza World Heritage site and Greater Cairo.*, Journal of Cultural Heritage, **23**,p 71-78,(2017).

Conference proceedings

1. A.M. Ruiz-Armenteros, **J.M. Delgado Blasco**, F. Lamas, R. Bravo-Pareja, M. Lazecky, M. Bakon, J. Sousa, M. Caro-Cuenca, G. Verstraeten, R.F. Hanssen, *Multi-Temporal Insar Monitoring of the Aswan High Dam (Egypt)*, IGARSS 2018 - 2018 IEEE International Geoscience and Remote Sensing Symposium (2018).
2. **J.M. Delgado Blasco**, G. Verstraeten, R.F. Hanssen, A.M. Ruiz-Armenteros, *Exploring the Data Fusion of European SAR and Landsat Satellites for Monitoring the Urban Changes in Greater Cairo (Egypt) from 2010 to 2015*, ISBN 978-92-9221-305-3, Living Planet Symposium 2016, Prague, 9-13 May 2016, **SP-740** (2016).
3. **J.M. Delgado Blasco**, G. Verstraeten, R.F. Hanssen, *Monitoring the urban expansion of Cairo from 2004 to 2010 through SAR data using a non-parametric supervised classifier*, ISBN 978-83-63245-57-3, Living Planet Symposium 2013, Edinburgh, 2013, **SP-740** (2014).

Other conference abstracts and presentations

1. **J.M. Delgado Blasco**, A.M. Ruiz-Armenteros, M. Caro-Cuenca, M. Lazecky, M. Bakon, J. Sousa, G. Verstraeten, R.F. Hanssen, *Aswan High Dam structural stability analysed by Persistent Scatterer Interferometry from 2004 until 2010*, FRINGE Workshop 2017, Helsinki, June 2017, (2017).
2. **J.M. Delgado Blasco**, R.F. Hanssen, G. Verstraeten, R. Lasaponara, *Monitoring the ground stability the World Heritage Cultural Site of Giza Pyramids and surroundings using persistent scatterers interferometry from 1992 to 2010*, 5th EARSel workshop on remote sensing for cultural heritage, Frascati Rome Italy, 12-13 November 2015,(2015).
3. I.L. Mohamed, **J.M. Delgado Blasco**, R.F. Hanssen, G. Verstraeten, *Quantifying migration rates of barchan dunes using radar and optical remote sensing imagery*, 34th EARSel Symposium, Warsaw, 16-20 June 2014,(2014)).

4. G. Verstraeten, I.L. Mohamed, H. Willems, V. De Laet, **J.M. Delgado Blasco**. *Analysis of Aeolian-Fluvial-Human Interactions in the Nile Valley (Central Egypt) by Combining Field-Based Geomorphology with Remote Sensing*, 34th EARSeL Symposium, Warsaw, 16-20 June 2014,(2014).
5. **J.M. Delgado Blasco**, I.L. Mohamed, R.F. Hanssen, G. Verstraeten, *The application of radar and optical remote sensing to analyze dune dynamics at the dune-field scale*, 8th IAG International Conference on Geomorphology, Paris, France, 31 August 2013,(2013).
6. **J.M. Delgado Blasco**, M. Hendrickx, V. De Laet, G. Verstraeten, R.F. Hanssen, *PS-InSAR and Change Detection techniques for analyzing the 3D evolution of Cairo and its surroundings from 2004 to 2010*, 3rd Workshop on Remote Sensing for Archaeology and Cultural Heritage Management, Ghent, 19-22 Sept 2012,(2012).

Other publications

Non-exhaustive list of other peer-reviewed journal and conference presentations

1. M. Fomelis, **J.M. Delgado Blasco**, F. Brito, F. Pacini, E. Papageorgiou, P. Pishehvar and P. Bally, *SNAPPING Services on the Geohazards Exploitation Platform for Copernicus Sentinel-1 Surface Motion Mapping*, Remote Sensing, Vol. 14, (2022).
2. A.M. Ruiz-Armenteros, **J.M. Delgado Blasco**, M. Bakon, M. Lazecky, and others, *Monitoring critical infrastructure exposed to anthropogenic and natural hazards using satellite radar interferometry*, 3rd Congress in Geomatics Engineering, (2021).
3. A. Braun, T. Höser and **J.M. Delgado Blasco**, *Elevation change of Bhasan Char measured by persistent scatterer interferometry using Sentinel-1 data in a humanitarian context*, European Journal of Remote Sensing, Vol.54, (2021).
4. S.M.J. Mirzadeh, S. Jin, E. Parizi, E. Chaussard, R. Bürgmann, **J.M. Delgado Blasco** and others, *Characterization of Irreversible Land Subsidence in the Yazd-Ardakan Plain, Iran From 2003 to 2020 InSAR Time Series*, Journal of Geophysical Research: Solid Earth, Vol. 126, (2021).
5. A.M. Ruiz-Armenteros, and A. Ruiz-Constán, M. Lazecky, M. Bakoň, and **J.M. Delgado Blasco**, and others, *Monitoring critical infrastructure and anthropogenic hazards in Malaga province (southern Spain) using SAR remote sensing*, EGU General Assembly Conference Abstracts, (2021).
6. **J.M. Delgado Blasco**, M. Fitrzyk, J. Patruno, A.M. Ruiz-Armenteros and M. Marconcini, *Effects on the double bounce detection in urban areas based on SAR polarimetric characteristics*, Remote Sensing, Vol. 12, (2020).
7. V. Fontana, **J.M. Delgado Blasco**, A. Cavallini, N. Lorusso, A. Scremin and A. Romeo, *Artificial intelligence technologies for Maritime Surveillance applications*, 21st IEEE International Conference on Mobile Data Management, MDM, (2020).
8. F. Orellana, **J.M. Delgado Blasco**, M. Fomelis, P.J.V. D'Aranno, M.A. Marsella and P. Di Mascio, *Dinsar for road infrastructure monitoring: Case study highway network of Rome metropolitan (Italy)*, Remote Sensing, Vol. 12, (2020).
9. A.M. Ruiz-Armenteros, **J.M. Delgado-Blasco**, M. Bakon, and others, *Monitoring dams structural stability from space using differential SAR interferometry*, EGU General Assembly Conference Abstracts, (2020).
10. F. Cian, **J.M. Delgado Blasco** and L. Carrera, *Sentinel-1 for monitoring land subsidence of coastal cities in Africa using PSInSAR: A methodology based on the integration of SNAP and StaMPS*, Geosciences, Vol.9, (2019).
11. J. Patruno, M. Fitrzyk, **J.M. Delgado Blasco**, *Monitoring and Detecting Archaeological Features with Multi-Frequency Polarimetric Analysis*, Remote Sensing, Vol. 12, (2019).

12. M. Fomelis, **J.M. Delgado Blasco**, Y.L. Desnos, M. Engdahl, D. Fernández, and others, *ESA SNAP – StaMPS Integrated Processing for Sentinel-1 Persistent Scatterer Interferometry*, International Geoscience and Remote Sensing Symposium 2018, IGARSS, (2018).
13. A. Habib, K. Labbassi, **J.M. Delgado Blasco**, F. Van Leijen, L. Iannini and M. Menenti, *Land deformation monitoring using PS-InSAR technique over Sahel-Doukkala (Morocco)*, International Conference on Advanced Technologies for Signal and Image Processing, ATSIP, (2017).
14. **J.M. Delgado Blasco**, C. Manganiello, P.G. Marchetti, M. Marrazzo and M. Arcorace, *Copernicus and AIS data fusion and information management for maritime tasks: preliminary results*, Conference on Big Data from Space, BiDS, (2017).
15. T. Reza, A. Zimmer, **J.M. Delgado Blasco** P. Ghuman, T.Kr. Aasawat and M. Ripeanu, *Accelerating persistent scatterer pixel selection for InSAR processing*, IEEE Transactions on Parallel and Distributed Systems, Vol. 29, (2017).
16. A. Ruiz-Constán, A.M. Ruiz-Armenteros, F. Lamas-Fernández, S. Martos-Rosillo, **J.M. Delgado Blasco**, D.P.S. Bekaert, J.J. Sousa, A.J. Gil, M. Caro Cuenca, R.F. Hanssen and others, *Multi-temporal InSAR evidence of ground subsidence induced by groundwater withdrawal: the Montellano aquifer (SW Spain)*, Journal of Environmental Earth Sciences, (2016).
17. **J.M. Delgado Blasco**, R. Cuccu, and G. Rivolta, Giancarlo, *Monitoring Ground Deformation Using Persistent Scatterers Interferometry (PSI) and Small Baselines (SBAS) Techniques Integrated in the ESA RSS Service: The Case Study of Valencia, Rome and South Sardinia*, FRINGE Workshop 2015, (2015).
18. R. Cuccu, G. Sabatino, **J.M. Delgado Blasco** and G. Rivolta, *Enabling SAR data exploitation by processing on-demand*, IEEE International Geoscience and Remote Sensing Symposium, IGARSS, (2015).
19. **J.M. Delgado Blasco**, F. Cian, G. Rivolta, C. Giupponi and A.M. Ruiz-Armenteros, *Fusion of Sentinel-1A and Sentinel-2A data for land use monitoring over Veneto region*, Mapping Urban Areas from Space, MUAS, (2015).
20. A.B. Ruescas, **J.M. Delgado Blasco**, F. Costantini and F. Sarti, *Change detection by interferometric coherence in Nasca Lines, Peru (1997–2004)*, FRINGE Workshop 2009, Vol. 30, (2009).

